

NIST Technical Note 1926

Energetics of Small and Moderate-Scale Gaseous Pool Fires

Anthony Hamins

This publication is available free of charge from:
<https://doi.org/10.6028/NIST.TN.1926>

NIST
**National Institute of
Standards and Technology**
U.S. Department of Commerce

NIST Technical Note 1926

Energetics of Small and Moderate-Scale Gaseous Pool Fires

Anthony Hamins
*Fire Research Division
Engineering Laboratory*

This publication is available free of charge from:
<https://doi.org/10.6028/NIST.TN.1926>

November 2016



U.S. Department of Commerce
Penny Pritzker, Secretary

National Institute of Standards and Technology
Willie May, Under Secretary of Commerce for Standards and Technology and Director

Certain commercial entities, equipment, or materials may be identified in this document in order to describe an experimental procedure or concept adequately. Such identification is not intended to imply recommendation or endorsement by the National Institute of Standards and Technology, nor is it intended to imply that the entities, materials, or equipment are necessarily the best available for the purpose.

**National Institute of Standards and Technology Technical Note 1926
Natl. Inst. Stand. Technol. Tech. Note 1926, 62 pages (November 2016)
CODEN: NTNOEF**

**This publication is available free of charge from:
<https://doi.org/10.6028/NIST.TN.1926>**

Table of Contents

Abstract	ii
Nomenclature	iii
1. Introduction	1
2. Experimental Method	3
2.1 Pool Burners	3
2.2 Measurement of Radiative Flux Distribution	4
2.3 Measurement of Convected Enthalpy.....	5
2.4 Measurement of Heat Feedback to the Burner	5
3. Enthalpy Balance.....	5
3.1 Calculation of Radiant Power.....	7
3.2 Calculation of Convected Enthalpy	8
3.3 Calculation of Heat Feedback to the Burner	8
4. Modeling Heat Feedback to the Fuel Surface	8
4.1 Convective Heat Transfer to the Fuel Surface.....	8
4.2 Radiative Heat Transfer to the Fuel Surface	9
5. Results and Discussion	10
5.1 Measured Enthalpy Fractions	10
5.2 Radiative Flux Distribution	13
5.3 Burner Surface Temperature	14
5.4 Uncertainty Analysis	15
6. Comparison of Heat Feedback Model Results with Measurements.....	16
7. Conclusions	20
8. Acknowledgements	20
9. References	21
Appendix 1. Summary of the Measurement Results	23
Appendix 2. Burner Surface Temperatures	26
Appendix 3. Radiative Heat Flux Distributions.....	34

Energetics of Small and Moderate-Scale Gaseous Pool Fires

ABSTRACT

A series of measurements was made to characterize the global properties of moderate-sized pool fires steadily burning in a quiescent environment with a focus on the energetics or the global energy balance in the fire. A wide range of parameters were considered, including lightly and heavily sooting hydrocarbon fuels (methane/natural gas, propane and acetylene), burners varying from 0.1 m to 1.0 m in diameter, and total heat release rates from about 0.4 kW to 200 kW. These conditions yielded flames that were 0.1 m to 2 m in mean height. Measurements were made characterizing the time-averaged mass burning rate and the distributions of radiative heat flux emitted. The data allow determination of the fraction of the energy released as radiation, a key global parameter characterizing a fire. For all fuels and burner sizes considered here, the radiative fraction increased and the enthalpy loss to the burner decreased as a function of increasing fuel mass flux. A previously developed model of convective heat feedback to the burner surface is coupled with a simple radiative heat flux model to estimate the total heat feedback to the burner, which was compared to measurements. Hundreds of measurements were made in scores of experiments, which were distilled into a handful of time-averaged quantities per experiment.*

KEYWORDS: acetylene, burning rate, combustion efficiency, convection, methane, pool fires, propane, radiative flux, radiative fraction

* Certain commercial products are identified in this report in order to specify adequately the equipment used. Such identification does not imply recommendation by the National Institute of Standards and Technology, nor does it imply that this equipment is the best available for the purpose.

NOMENCLATURE

A	Cross sectional area of the exhaust duct [m^2]
C_p	Heat capacity of the exhaust gases
C_{pw}	Heat capacity of the water cooling the burner
h	Convective heat transfer coefficient [$\text{W}/(\text{m}^2\text{-K})$]
H_c	Heat of combustion of the fuel [kJ/g]
L	Mean flame height [m]; see Eq. 15
\dot{m}	Fuel mass burning rate [g/s]
\dot{q}''	Local heat flux [kW/m^2]
\dot{Q}_r	Radiative emission from the fire to the surroundings [kW]; see Eq. 9
\dot{Q}_c	Sensible enthalpy of the fire plume [kW]; see Eq. 10
Q_b	Heat feedback to the fuel surface [kW]; see Eqs. 11 and 13
\dot{Q}_{bc}	Convective heat feedback to the fuel surface [kW]; see Eq. 12
\dot{Q}_{br}	Radiative heat feedback to the fuel surface and burner [kW]; see Eq. 13
\dot{Q}^*	Normalized heat release rate; see Eq. 16
R_o	Radial position of the vertical radiometer array [m]
T	Temperature
ΔT	Temperature difference between the ambient and the duct temperature [$^{\circ}\text{C}$]
ΔT_w	Temperature difference between the burner water cooling inlet and outlet [$^{\circ}\text{C}$]
V_a	Average velocity of gases in the exhaust duct at the measurement station [m/s]
V_w	Average volumetric flow of water cooling the burner [l/s]

Greek Symbols

ρ	Gas density in the exhaust duct [g/m^3]
χ_r	Radiative emission from the fire to the surroundings (but not the fuel surface/burner) normalized by the idealized heat of combustion [dimensionless]; see Eqs. 2 and 9
χ_c	Convective enthalpy normalized by the idealized heat of combustion [dimensionless]; see Eqs. 2 and 10
χ_a	Combustion efficiency [dimensionless]; see Eq. 1
χ_b	Heat feedback to the burner normalized by the idealized heat of combustion [dimensionless]; see Eqs. 2, 5, and 11
χ_{bc}	Fraction of heat feedback to the fuel surface due to convection [dimensionless]; see Eq. 9
χ_{br}	Fraction of heat feedback to the fuel surface due to radiation [dimensionless]; see Eq. 14
χ_{rad}	Radiative fraction emitted to the surroundings and fuel surface [dimensionless]; see Eq. 8

1. INTRODUCTION

The measurement results reported here represent experiments that were conducted during the years 1992 to 1994 at NIST. The measurements were made to characterize the global properties of moderate-sized pool fires steadily burning in a quiescent environment. The focus was on the energetics, or the global energy balance, in the fire. Previously unpublished results characterizing the distributions of the local radiative heat flux emitted by various fires are presented. These results may be of use in the validation of computational fluid dynamics fire models, something that was not envisioned in the early 1990s. Some previously reported results are shown here for completeness – as this information is needed to define the fires for modeling purposes. Reference to previous work is made as appropriate.

Use of fire modeling in fire protection engineering has increased dramatically during the last decade due to the development of practical computational fluid dynamic fire models and the decreased cost of computational power. Today, fire protection engineers use models like the Consolidated Fire and Smoke Transport Model (CFAST) and the Fire Dynamics Simulator (FDS) to design safer buildings, nuclear power plants, aircraft cabins, trains, and marine vessels to name a few types of applications. [1, 2] To be reliable, the models require validation, at the heart of which lies a large collection of experimental measurements. The objective of this report is to provide data for use in fire model evaluation by the fire research community.

The boundary conditions of a fire, that is the manner by which the fuel and burner are configured, can impact a fire's structure and dynamics. In this report, the focus is on pool fires, which are a fundamental type of fire where the fuel surface is flat and horizontal, providing a simple and well-defined configuration to test models and further the understanding of fire phenomena. There are significant differences in the boundary conditions given for liquid and gaseous pool fires. For liquid pool fires, the boundary condition at the pool surface obeys the Clausius-Clapeyron relation with the surface isothermal and observed to be approximately at the boiling point. The mass flux at a liquid pool surface, on the other hand, is not necessarily constant across the pool surface - as the heat feedback can vary as a function of location in the pool. [3,4] For gaseous pool fires, while the mass flux is nominally constant across the burner surface, an isothermal surface condition, does not hold. Instead, the temperature depends on the local heat transfer of the system, involving the fire and the burner. Water cooling of the burner can moderate the surface temperature, depending on burner design. Monitoring the rate of thermal cooling allows measurement of the heat feedback to the burner.

In this study, a series of gaseous pool fires was studied for a range of parameters including the mass burning rate, the pool diameter, and fuel type. Measurements were conducted using methane, propane, natural gas, and acetylene in burners varying from 0.1 m to 1 m in diameter with total heat release rates from 0.4 kW to 200 kW. A series of measurements were made characterizing the time averaged mass burning rate and the distributions of radiative heat flux emitted from the fires. These data were used to determine the radiative fraction, a key global parameter characterizing a fire. Radiative heat flux distribution measurements were made for about 80 fire scenarios. Additional fires scenarios were considered to better understand the partition of the transport of energy from the fire.

Experiments were conducted varying the fuel mass flux for fires burning in a quiescent environment in three circular burners (0.10 m, 0.35 m, and 1.00 m diameters) for idealized heat release rates varying about two orders of magnitude from 1 kW to 100 kW. Measurements were made of the time-averaged distributions of radiative heat flux emitted to the surroundings. These results were used to determine the radiative fraction, a parameter characterizing the fraction of energy lost to the surroundings. A number of other measurements were made, including heat loss to the burner, and for some tests, the sensible enthalpy fraction transported by the fire plume via convection. Results from six of the experiments have been previously used to test the efficacy of FDS to predict the radiative flux distribution from moderate-sized methane fires. [1,2] Those data are presented here along with another 24 data sets for methane/natural gas fires, 16 acetylene fires, and 34 propane fires. Table 1 shows the gaseous fuels tested, the number of experiments conducted for each fuel type and burner diameter, and the fuels' heat of combustion.

Table 1. Summary of Range of $\dot{m} H_c$ Values for Radiative Distribution Experiments

Fuel	Number of Data Sets			H_c (kJ/g)	Range of $\dot{m} H_c$ (kW)		
	<u>Burner Diameter</u>				<u>Burner Diameter</u>		
	0.10 m	0.35 m	1.00 m		0.10 m	0.35 m	1.00 m
Methane	5	6	0	50.0	0.4 to 2	10 to 200	-
Natural Gas	0	8	11	49.1 to 49.4	-	10 to 90	50 to 170
Propane	16	8	11	46.4	0.4 to 40	10 to 110	50 to 140
Acetylene	5	11	0	48.2	0.5 to 2	10 to 140	-

Table 2. Parameter Scorecard: Key Parameters Experimentally Measured (E), Calculated (C), Modeled (M) or Not Measured (N) for the Fuels and Burner Diameters Tested*

Fuel	Diameter (m)	\dot{m}	\dot{Q}_r	\dot{Q}_c	\dot{Q}_a	\dot{Q}_b	\dot{Q}_{br}	\dot{Q}_{bc}
Acetylene	0.10	E	E	C	N	E	M	M
	0.35	E	E	E	C	E	M	M
Propane	0.10	E	E	C	N	C	M	M
	0.35	E	E	C	N	E	M	M
	1.00	E	E	C	N	C	M	M
Methane/ Natural Gas	0.10	E	E	C	N	E	M	M
	0.35	E	E	C	N	E	M	M
	1.00	E	E	C	N	C	M	M

A number of parameters in this study were determined either through experimental measurement (see Section 2), calculation from simple conservation rules (see Section 3), or modeled (see Section 4). Table 2 lists the key parameters* and summarizes how they are determined for each of the fuel types and burner sizes considered. In a few experiments, measurements were made of the total heat transfer to the burner and the sensible enthalpy transfer to the surroundings by convection. Information on the latter allowed estimation of the combustion efficiency. A model for heat transfer to the burner facilitated comparison

* For definitions of the parameters, see the Nomenclature Section and Sections 2 - 4 of this report.

with measurements of heat feedback to the burner. Table 2 complements Table 1 and provides an overview of the methods used to obtain the results discussed in the next two sections of this report.

This report is broken into several parts. In Section 2, the experimental method and apparatus are described. In Section 3, the enthalpy balance in a pool fire is discussed. The various energy terms are defined and the methods used to determine the radiant power and convected enthalpy of the fire are described. In Section 4, a model describing the radiative and convective heat feedback to the fuel surface is discussed. In Section 5, the results are discussed, including the measured enthalpy fractions, the radiative heat flux distributions, the burner surface temperatures, and the results of an uncertainty analysis. Section 6 compares the heat feedback model results to the measurements. Estimates of measurement uncertainty are presented. Section 7 summarizes the results. References are provided in Section 8. A series of appendices are presented containing the measurement, calculation and model results, including the global energy components (Appendix 1), the measured burner surface temperatures (Appendix 2), and plots of the local distribution of radiative flux in the vertical and radial directions (Appendix 3).

2. EXPERIMENTAL METHOD

Steady-state burning conditions were established before measurements were initiated. A warm-up period of 3 min to 5 min was required for steady conditions. The experimental apparatus and method are described in more detail in Refs. [5, 6, 7, 8, 9, 10, 11, 12], respectively. The rate of gaseous fuel delivery was controlled using calibrated rotometers. The mass flow of the gaseous fuel was determined from multiple measurements using a dry test meter fitted with a pressure gauge, and a stopwatch to measure the volume per unit time of fuel delivered to the burner and a thermocouple measurement of the ambient temperature. The expanded measurement uncertainty (with a coverage factor of two* [13]) for the fuel mass flow was 4 %. [3]

2.1 Pool Burners

All three burners used in this study were circular. Each burner was somewhat different in design and construction as described below.

The smallest burner was composed of brass. It had a 0.1016 m outer diameter with a wall thickness of approximately 0.0016 m. It was 0.10 m deep and filled with a 0.03 m layer of sand to the rim; below the sand was a 0.07 m layer of glass beads. A 3 mm (outer diameter) copper water-cooling line was embedded as a series of coils in the form of a loosely wound spiral located 1 cm below the surface of the sand and around the outside of the burner. Sand is a good insulator; thus the surface of the sand was at elevated temperatures as measured by three thermocouples at the burner surface ($r = 0$ cm, 2.5 cm, and 4.5 cm from the burner center). The measured temperature varied radially across the surface with temperatures reaching steady values of a few hundred degrees after burner warm-up. The area-weighted steady-state average temperature varied from 200 °C to 450 °C.

* unless otherwise noted, a coverage factor of two is used in uncertainty analysis throughout this report, which represents two times the standard deviation and a 95% confidence interval.

The middle-sized burner was made of porous sintered-bronze and was water cooled with the surface having a physical dimension of 0.380 m diameter, yet the effective diameter of the burning area was observed to be consistently smaller as noted by a flame-free outer (1.5 cm) annular section on the burner surface. The effective diameter was measured as 0.353 m. The burner was about 0.10 m deep. The surface temperature of the burner was taken as approximately equal to the water cooling temperature at the burner outlet.

The largest burner was composed of stainless steel. It had a 1.002 m inner diameter, was 0.075 m deep, and had a wall thickness of approximately 0.0016 m. The burner was filled with a layer of coarse gravel and then a 0.03 m layer of sand to the rim. The bottom of the burner was not water-cooled. Sand is a good insulator, so the surface temperature of the sand was at elevated temperatures, as measured by thermocouples at the burner surface (0 m, 0.25 m, and 0.45 m from the burner center).

2.2 Measurement of Radiative Flux Distribution

The time-averaged local radiative heat flux distribution, $\dot{q}''(r, z)$, along a cylindrical control surface surrounding the fire was measured using a set of calibrated water-cooled radiometers. The local heat flux was measured using wide angle (150° view angle) total heat flux gauges coated with a high emissivity paint with a flat spectral response in the infrared. About 10 water-cooled (2.5 cm diameter) total heat flux transducers were positioned along perpendicular axes aligned with the burner such that the radiative energy distribution was mapped onto a cylindrical control surface surrounding the fire with the base of the cylinder defined by the plane of the fuel surface. Figure 1 shows a schematic diagram of the experimental set-up. The first row of radiometers was positioned on a vertical axis located some distance away from the fire (R_0 in Figure 1). These radiometers were oriented horizontally facing the fire. The second row of radiometers was oriented upwards and positioned along the radius on the plane aligned with the burner surface. The radiative flux typically drops off very quickly in the radial direction, whereas in the vertical direction, the flux peaks at a vertical location equal to approximately 50 % of the characteristic flame height and then drops to small values above the visible flame tip as illustrated in Figure 1 for a typical case. The gauges were calibrated using a secondary standard in a well-characterized radiometer facility. [14,15] The gauges had a time response of approximately 2 s and the measured signal was time-averaged for about one min. The total expanded uncertainty in the radiative flux measurement was 16 %, which took into account gauge calibration and signal (and background) variance.

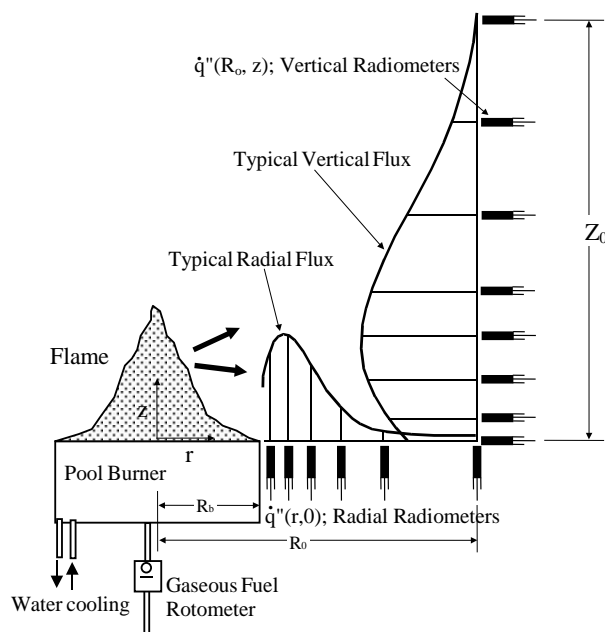


Figure 1. A schematic diagram of the set-up used in the measurement of the radiative fraction.

2.3 Measurement of Convected Enthalpy

For the 0.35 m acetylene fires, the convected enthalpy (\dot{Q}_c) in the plume was determined by measuring the flow and temperature near the exhaust duct inlet. The base of the burner was about 0.7 m above the floor and the exhaust hood entrance was about 3 m above the floor. A thermocouple array was placed about 2 m downstream of the exhaust duct entrance to determine the exhaust temperature. The total mass flow was determined about 20 m downstream using a bidirectional probe and thermocouple in the exhaust stream. Measurements were made after the velocity and temperature were steady, which usually occurred several minutes after setting the fuel flow rate. The temperature and velocity measurements were acquired at a sampling rate of 0.2 Hz and averaged for approximately 2 min.

2.4 Measurement of Heat Feedback to the Burner

For the two smaller water-cooled burners (0.10 m and 0.35 m), the steady-state average temperatures of the inlet and outlet of the cooling water were measured using 3 mm diameter stainless steel sheathed type K thermocouples. The cooling water volumetric flow (\dot{V}_w) was measured using a 1 liter graduated cylinder and a stopwatch.

3. ENTHALPY BALANCE

Consideration of the enthalpy balance helps identify the parameters that were considered in this study and that control the energetics and character of a fire. The radiative fraction, for example, has important implications in terms of fire spread, ignition of nearby items, and thereby fire safety. The magnitude of radiative transfer to targets external to the flame controls the rate of fire spread, which affects the hazard posed by a fire. Radiative transfer from a flame to the fuel surface is a key heat feedback mechanism that

influences the fuel evaporation rate in condensed-phase pool fires and consequently the fire size and its hazard.

The actual heat release rate (\dot{Q}_a) of a fire equals the sum of the enthalpy convected by the buoyant plume to the surroundings (\dot{Q}_c), the enthalpy feedback to the pool surface (\dot{Q}_b), and the energy radiated to the surroundings by high temperature particulates and gases (\dot{Q}_r):

$$\dot{Q}_a = \chi_a \dot{Q} = \dot{Q}_r + \dot{Q}_c + \dot{Q}_b \quad (1)$$

where the actual heat release rate is equal to the idealized of total heat release rate (\dot{Q}) modified by the combustion efficiency (χ_a). The idealized heat release rate is defined as:

$$\dot{Q} = \dot{m} H_c \quad (2)$$

where \dot{m} is the fuel mass flow [g/s] and H_c is the idealized heat of combustion of the fuel [kJ/g]. Dividing by \dot{Q} , Eq. 1 can be re-written as:

$$\chi_a = \chi_r + \chi_c + \chi_b \quad (3)$$

where χ_r , χ_c , and χ_b are the fractional radiative loss, convective loss, and heat feedback to the fuel surface. For hydrocarbon pool fires, the values of the fractional enthalpy losses are dependent on fuel type, burner diameter, and fire size. For liquid pool fires, the mass burning rate depends on the pool diameter. For gaseous pool fires, the mass burning rate is an independently controlled parameter. Varying the mass burning rate allows an understanding of the energetics and character of fires associated with a variety of fuel types and fire sizes.

The fractional heat feedback to the burner (χ_b) represents the total heat feedback to the burner via radiation, convection and conduction. Each of these terms can be considered independently. For moderate pool diameters, the total heat feedback to the burner (\dot{Q}_b) is related to the radiative (\dot{Q}_{br}) and convective (\dot{Q}_{bc}) heat feedback to the burner; the contribution of conduction is neglected as it is much smaller than the radiative and convective terms [3] for the burner sizes considered here.

$$\dot{Q}_b = \dot{Q}_{br} + \dot{Q}_{bc} \quad (4)$$

Normalizing this expression by the total heat release rate (\dot{Q}), the value of χ_b is equal to the sum of the radiative (χ_{br}) and convective (χ_{bc}) heat feedback to the burner:

$$\chi_b = \chi_{br} + \chi_{bc} \quad (5)$$

where the values of χ_{bc} and χ_{br} in Eq. 5 are the convective and radiative heat transfer to the burner surface normalized by the total fire heat release rate (\dot{Q}):

$$\chi_{bc} = \dot{Q}_{bc} / \dot{Q} \quad \text{and} \quad \chi_{br} = \dot{Q}_{br} / \dot{Q} \quad (6)$$

Tewarson and coworkers [19] write Eq. 3 as:

$$\chi_a = \chi_{con} + \chi_{rad} \quad (7)$$

where the combustion efficiency (χ_a) is broken into convective and radiative components. Here, the convective and radiative components are considered in terms of heat transfer to the surroundings and heat transfer to the fuel surface such that:

$$\chi_{rad} = \chi_r + \chi_{br} \text{ and } \chi_{con} = \chi_c + \chi_{bc} \quad (8)$$

Measurement of the radiative and convective heat feedback to the fuel surface (\dot{Q}_{br} and \dot{Q}_{bc} , respectively) is a challenging measurement and scant data are available in the fire literature on this topic [see Ref. 3, for example]. In some studies, the value of χ_{rad} has been estimated by assuming that the radiative flux across the fuel surface, $\dot{q}''(r \leq R_b, z = 0)$, is uniform and approximately equal to the flux measured just outside the burner, $\dot{q}''(r \approx R_b, z = 0)$. [7] This approach was used for moderate-size hydrocarbon fires, where the radiative flux is expected to be uniform across the burner surface. [7] For the fires considered here, however, a broad range of fire conditions were considered and the uniformity of the flux distribution across the pool surface was unknown. Tewarson and coworkers [19] describe measurements of \dot{Q} , \dot{Q}_c and \dot{Q}_a for conditions where \dot{Q}_{bc} is considered negligible and determine χ_{rad} from Eq. 7. For the fires considered here, the first approach may be problematic, particularly for low values of heat release rate per unit surface area, where χ_{bc} can be as large as 0.2. Here, \dot{Q}_{br} and \dot{Q}_{bc} are estimated based on Froude modeling, which allows estimation of χ_{bc} and χ_{br} . This allows calculation of χ_{rad} using Eq. 8.

3.1 Calculation of Radiant Power

The radiant power, or energy per unit time (\dot{Q}_r), emitted by the fire to the surroundings was determined by integrating the measured spatial distributions of radiant flux about a cylindrical control surface surrounding the fire:

$$\dot{Q}_r = 2\pi R_o \int_0^{Z_o} \dot{q}''(R_o, z) dz + 2\pi \int_{R_b}^{R_o} r \dot{q}''(r, 0) dr \quad (9)$$

where Z_o , R_b , and R_o are defined as the location of the uppermost vertical heat flux gauge, the burner radius, and the radial position of the vertical radiometer array as seen Fig. 1. This approach assumes that the fire is axisymmetric. The value of Z_o was experimentally selected to be large enough such that $\dot{q}''(R_o, z)$ was very small. The experimental location of the radiometers defined Z_o and R_o , and thereby the dimensions of the control surface used in Eq. 9. The integrals in Eq. 9 do not include radiative heat

feedback (\dot{Q}_{br}) to the fuel surface ($= 2\pi \int_0^{R_b} r \dot{q}''(r, 0) dr$), which is treated below.

3.2 Calculation of Convected Enthalpy

The sensible enthalpy of the plume was determined from the heat carried by the combustion products through the exhaust duct assuming relatively small losses to the hood and duct walls in steady-state:

$$\dot{Q}_c = \rho V_a A C_p \Delta T \quad (10)$$

where ρ is the gas density, V_a is the velocity of the exhaust, A is the duct cross-sectional area, C_p is the heat capacity of the exhaust, and ΔT is the difference between the ambient temperature and the averaged measured temperature at the thermocouple array. The heat capacity and density of the exhaust flow was computed as a function of temperature using the ideal gas law. The gas was assumed to be pure air, which is a fair approximation as the exhaust gases are composed mainly of air (with only highly dilute amounts of combustion products such as CO, CO₂ and H₂O at values of less than about a few percent by volume). With mass conserved in the duct, mass flow measurements were made far downstream from the duct entrance using thermocouples and bidirectional probes.

Determination of the convected enthalpy (\dot{Q}_c) in the plume allowed estimation of the combustion efficiency (χ_a) using Eq. 3. For the well-ventilated methane, natural gas, and propane fires, χ_a was taken as approximately equal to 1. [19]

3.3 Calculation of Heat Feedback to the Burner

For the two smaller water-cooled burners (0.10 m and 0.35 m), the measured steady-state average temperature difference (ΔT_w) between the water inlet and outlet, and the volumetric rate of water flow (\dot{V}_w) were used to determine the total heat feedback to the burner (\dot{Q}_b):

$$\dot{Q}_b = \dot{V}_w C_{pw} \Delta T_w \quad (11)$$

where C_{pw} is the heat capacity of the burner cooling water

4. MODELING HEAT FEEDBACK TO THE FUEL SURFACE

Following the approach used by Orloff and de Ris [16, 17], Froude modeling is applied to assess radiative emission from pool fires, including the heat feedback from a fire to the fuel surface. The flame is assumed to be homogeneous and of uniform temperature, approximated as 1200 K. A cylindrical flame shape is assumed with the base equal to the burner diameter ($2R_b$) and the cylindrical length is taken as the mean flame height (L).

4.1 Convective Heat Transfer to the Fuel Surface

Applying stagnant film theory, the convective heat transfer to the fuel surface (\dot{Q}_{bc}) can be modeled [17] as:

$$\dot{Q}_{bc} = A_s (h/ C_p) [H_c (\chi_a - \chi_{rad}) r / \chi_a - C_p (T_s - T_\infty)] y / (e^y - 1) \quad (12)$$

where $y = \dot{m}'' C_p / h$ is a blowing factor, \dot{m}'' is the mass flux (i.e., the burning rate per unit surface area of the burning pool), r is the stoichiometric fuel/air mass ratio, T_s is the burner surface temperature, T_∞ is the ambient temperature, C_p is the heat capacity of air taken at a representative temperature equal to the average of the flame temperature and the burner surface temperature, and h is the heat transfer coefficient. The value of h was taken as $8.5 \text{ W}/(\text{m}^2\text{-K})$, or $h/C_p = 7.75 \text{ W}/(\text{m}^2\text{-K})$ for pools without “lips” [17] - where the rim of the burner did not extend above the burner surface as was the case in the experiments reported here. Equation 12 suggests that convective heat transfer plays a significant role, particularly for small burning rates.

4.2 Radiative Heat Transfer to the Fuel Surface

The value of \dot{Q}_{br} can be related to \dot{Q}_r through Froude modeling [17]. Assuming relatively small fuel surface re-radiation and reflectivity, heat conduction to the fuel surface, and fuel vapor blockage. Orloff and de Ris relate the fire radiative emission to an average effective flame temperature, the Stefan-Boltzmann constant, a mean beam length representative of radiative transfer, an effective absorption-emission coefficient, and the bounding flame surface area. [16, 17] Equations 10 and 18 in Ref. [17] describe \dot{Q}_{br} and \dot{Q}_r , for flames characterized by intermediate opacity. Taking the ratio of these equations, the value of \dot{Q}_{br} can be shown to be directly proportional to the total radiative emission of the fire, modified by a geometric factor equal to the ratio of the flame base area to that of the bounding surface, such that:

$$\dot{Q}_{br} = \dot{Q}_r / (1 + 2 \frac{L}{R_b}) \quad (13)$$

Dividing by \dot{Q} , Eq. 13 can be expressed in terms of the fractional radiative heat feedback to the burner:

$$\chi_{br} = \chi_r / (1 + 2 \frac{L}{R_b}) \quad (14)$$

For the fires considered in this study, the ratio (L/R_b) takes on a range of values from about 1 to 8, yielding values of the ratio (χ_{br}/χ_r) ranging from 0.06 to 0.33.

Heskestad [18] provides a correlation relating the mean flame height (the 50 % intermittency value) to the heat release rate (\dot{Q}) and the fire diameter ($D = 2R_b$):

$$\frac{L}{D} = -1.02 + 3.7 \dot{Q}^{*2/5} \quad (15)$$

where

$$\dot{Q}^* = \frac{\dot{Q}}{\rho_\infty c_p T_\infty \sqrt{g d} D^2} \quad (16)$$

Determination of χ_{br} allows calculation of χ_{rad} using Eq. 8.

5. RESULTS AND DISCUSSION

A summary of the results for the gaseous acetylene, propane, and methane/natural gas experiments are shown in Tables A1.1 – A1.3 in Appendix 1, respectively, which list the fire diameter (D), the mass burning rate (\dot{m}), the idealized heat release rate ($\dot{m} H_c$), the time-averaged radiative fraction (χ_r), the convected enthalpy fraction (χ_c), and the enthalpy fraction lost to the burner (χ_b). The term R_o is also listed, which defines the radial position of the vertical radiometer array shown in Figure 1. Table A1.2 (the acetylene results) also includes the combustion efficiency (χ_a).

Figure 2 shows images of the 0.35 m acetylene fire and the 0.10 m propane fire. Although both fires are luminous, the acetylene fire produces copious amounts of soot, as observed by the black smoke emitted downstream from the flame tip.

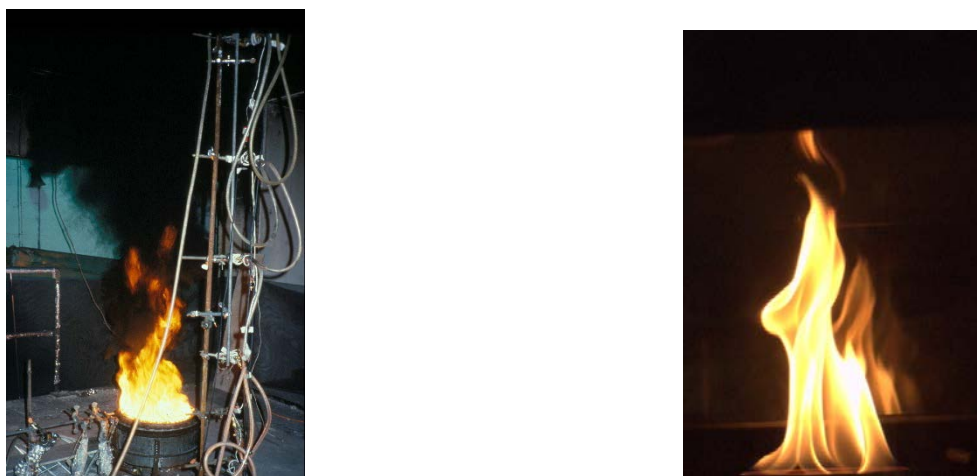


Figure 2. Photos of acetylene burning in the 0.35 m burner (left) and propane burning in a 0.10 m burner (right). Unlike propane, the acetylene fires emitted copious amount of soot.

5.1 Measured Enthalpy Fractions

Figures 3 and 4 show the variation of χ_c , χ_b and χ_r with fuel mass flux for the methane/natural gas and propane fires, respectively. [8] The data are presented in Tables A1.1 and A1.2 in Appendix 1. Plotting the results in terms of mass flux allows comparison of results from different burners. The results for χ_c were calculated assuming that the value of χ_a was equal to unity. This is not an unreasonable assumption as the methane, natural gas, and propane fires are expected to emit relatively small amounts of soot for well-ventilated fires. [19]

Figure 5 shows results from Table A1.3 in Appendix 1 for the 0.35 m diameter acetylene fires, plotting χ_a , χ_c , χ_b and χ_r as a function of the acetylene mass flux. [6] The fires plotted in Figure 3 have

idealized heat release rates that vary from about 10 kW to 130 kW.* For the fires considered here, the value of χ_a was estimated to be as low as about 0.65 (± 0.14) with much of the unburned carbon emitted as smoke (see Figure 2).

For all fuels and burner sizes considered here, the radiative fraction increased and the enthalpy loss to the burner decreased as a function of increasing fuel mass flux. The changing radiative flux has been previously observed for small and moderate-scale gaseous pool fires [6], and is quite different than that observed for liquid pool fires, which are fairly constant over a range of small and moderate-scale pool diameters [7].

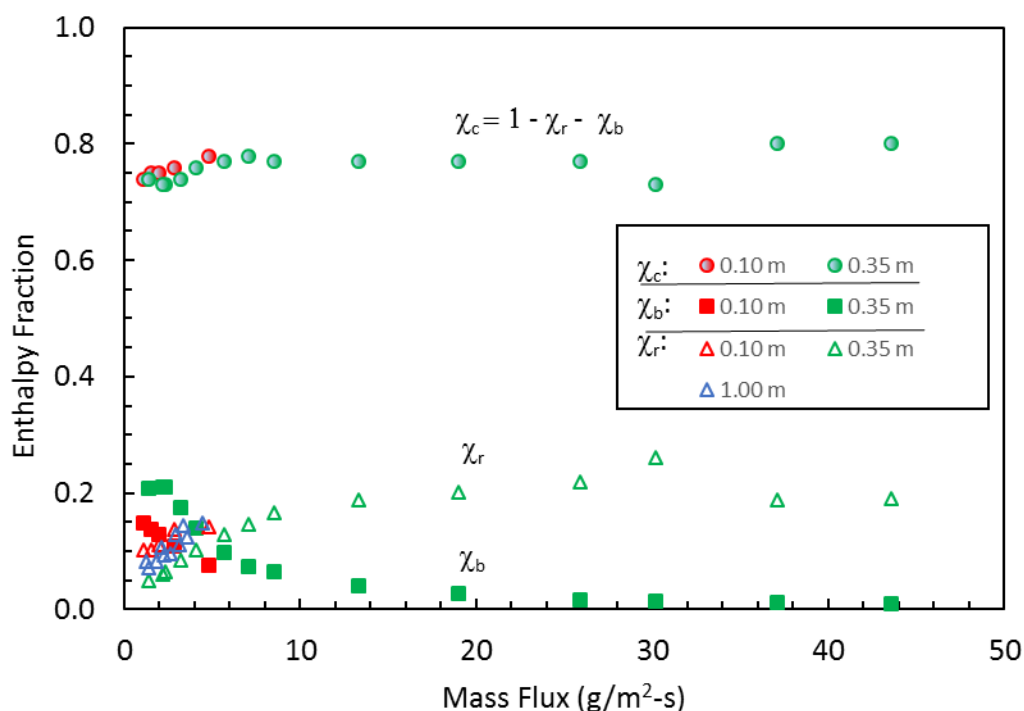


Figure 3. Measured values of χ_r and χ_b , and calculated values of χ_c , as a function of the methane/natural gas mass flux in the 0.10 m, 0.35 m, and 1.00 m burners.

* an acetylene fire with an idealized heat release rate of about 20 kW had a mass flux of about 4.4 $\text{g/m}^2\text{-s}$ in the 0.35 m burner.

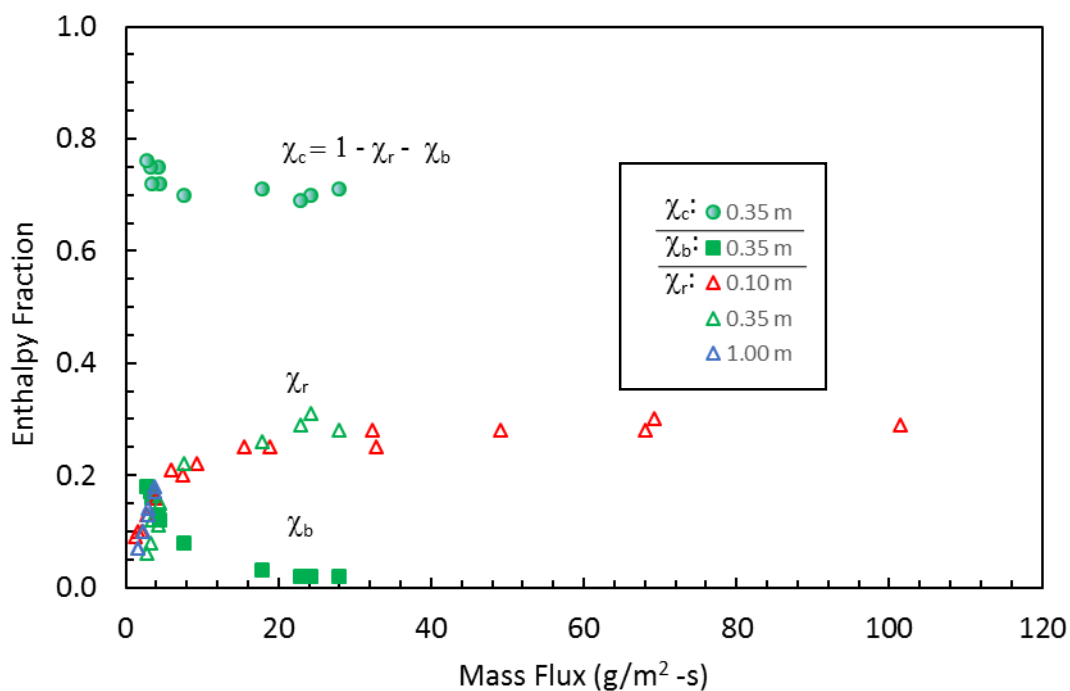


Figure 4. Measured values of χ_r and χ_b and calculated values of χ_c as a function of the propane mass flux.

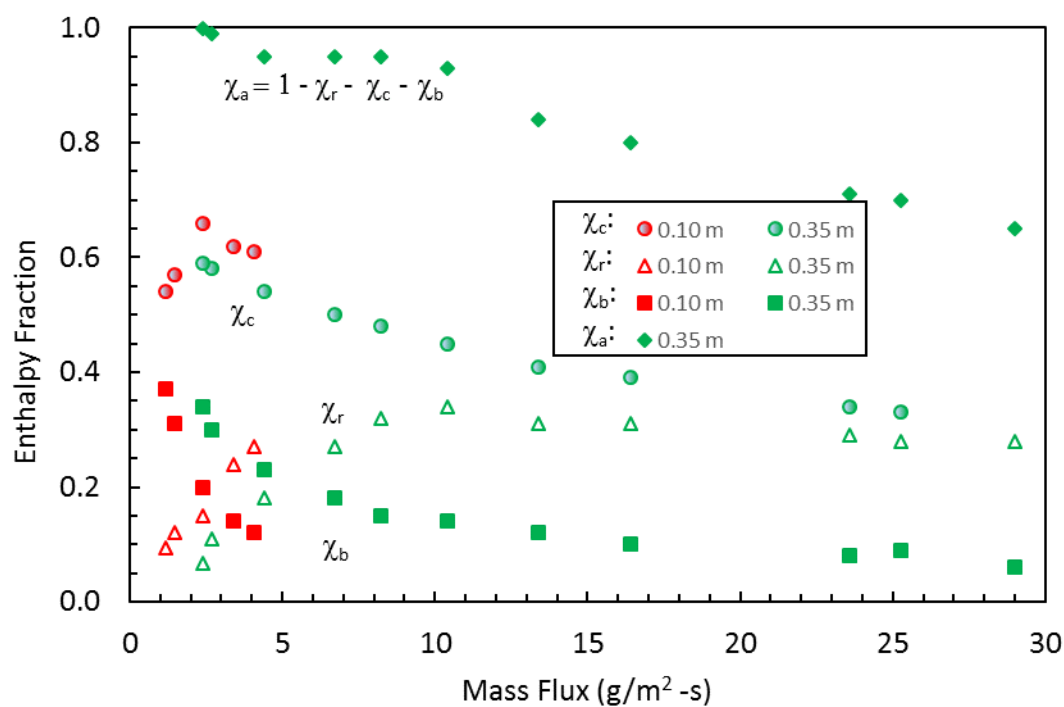


Figure 5. Measured values of χ_r , χ_b , and χ_c (0.35 m burner) and calculated values of χ_a and χ_c (0.10 m burner) as a function of the acetylene mass flux.

5.2 Radiative Flux Distribution

For each of the 80 fires listed in Appendix 1, a complementary file provides the measured distribution of radiative heat flux in the downward ($\dot{q}''(r, z=0)$) and radial ($\dot{q}''(r=R_b, z)$) directions, as indicated in Fig.

1. Typical radiative heat flux measurements are presented in Figure 6, which shows the radiative heat flux distribution for Test A10, an acetylene fire burning in the 0.35 m burner. The left-hand side of the figure shows the flux downwards as a function of radial distance from the burner center. The dashed vertical line on the left in the figure represents the location of the burner edge (at 0.175 m). The right-hand side of the figure shows the flux as a function of vertical location downstream the plane defined by the burner surface for locations 0.69 m from the burner axis. The flux data were used to determine χ_r .

For Test A10, χ_r was calculated as 0.32 ± 0.04 as noted in Figure 5.

The measured radiative heat flux distributions are presented in Appendix A3. The figures show the flux in the downwards direction as a function of radial distance from the burner center (filled symbols), and the flux in the radial direction with respect to locations above the burner surface along the burner axis (unfilled symbols). The lines in the figures are best fits to the data. Sometimes the radial flux is larger than the axial (vertically downwards) flux, sometimes not, depending on the fire size and shape. In all cases, however, the integrated flux in the radial direction is larger than that in the axial direction and had a larger contribution to χ_r . For these experiments, the value of R_0 varies from 0.8 to 5 times the burner diameter. Hostikka [5] used FDS to simulate the radiative flux distribution from a number of the methane fires reported in this data set (namely, Tests M1, M5, M15, M17, M20, and M30 in Table A1.1).

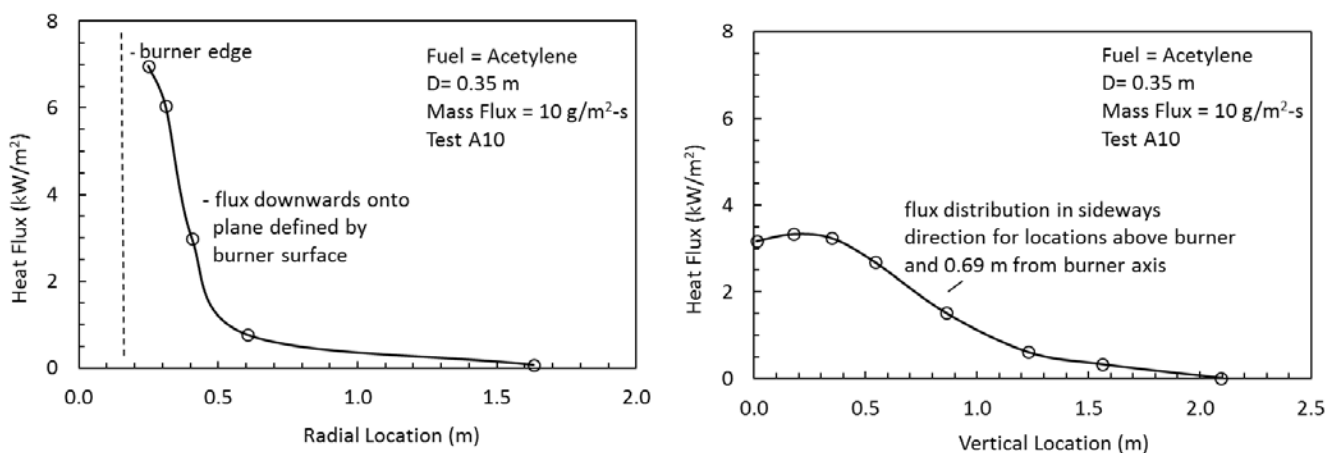


Figure 6. The distribution of radiative heat flux (\dot{q}'') in a 0.35 m acetylene fire (Test A10) showing the flux downwards as a function of radial distance from the burner center (left) and the radial flux as a function of vertical location above the plane defined by the burner surface for locations 0.69 m from the burner axis (right). The lines are best polynomial fits to the data. The expanded uncertainty was 16 %.

5.3 Burner Surface Temperature

The steady-state average temperature difference (ΔT_w) between the burner water cooling inlet and outlet in the 0.10 m and the 0.35 m burners was typically $50\text{ }^{\circ}\text{C} \pm 3\text{ }^{\circ}\text{C}$. The surface temperature of the water-cooled 0.35 m sintered metal burner was taken as nearly uniform. The temperature on the burner surface for fires in the 0.10 m and 1.0 m sand burners, however, was non-uniform. This is seen in Figure 7 for the natural gas fires established in the 1.0 m burner, where the measured surface temperature is plotted as a function of the fuel mass flow (proportional to the heat release rate) for three surface locations ($r = 0.00\text{ m}$, 0.25 m , and 0.45 m ; see Figure 1). The expanded uncertainty for the three thermocouples positioned at each of the r locations was dominated by measurement variance (see the uncertainty bars in Figure 7). The average value of the expanded uncertainties was $20\text{ }^{\circ}\text{C}$. The surface temperature increased with mass flow (and heat release rate) for locations near the middle of the burner (at $r=0.00\text{ m}$ and 0.25 m), but decreased closer to the burner edge ($r = 0.45\text{ m}$). These results suggests that fire size and fuel blowing rate, as well as flame structure play a significant role in heat transfer to the burner. These data and the other surface temperature results are presented in tabular form in Appendix 2.

Tables A2.1 in Appendix 2 shows the measured surface temperature distribution for the 0.10 m diameter fires (Tests M1-M20) as a function of the radial distance from the burner center (r in Figure 1). The temperature varied from $220\text{ }^{\circ}\text{C}$ to $370\text{ }^{\circ}\text{C}$ depending on the conditions and the radial location. The area-weighted mean temperature (T_{avg}) is also listed. Table A2.2 in Appendix 2 shows the measured cooling water temperature at the burner inlet and outlet for the 0.35 m diameter methane/natural gas experiments (Tests M21-M31). The average temperatures were between $30\text{ }^{\circ}\text{C}$ and $70\text{ }^{\circ}\text{C}$. Under steady-state conditions, the temperature difference between the inlet and outlet provided a basis for determining the heat transfer to the burner. Similar results are seen for the propane and acetylene fires, which are shown in Tables A2.3 to A2.6.

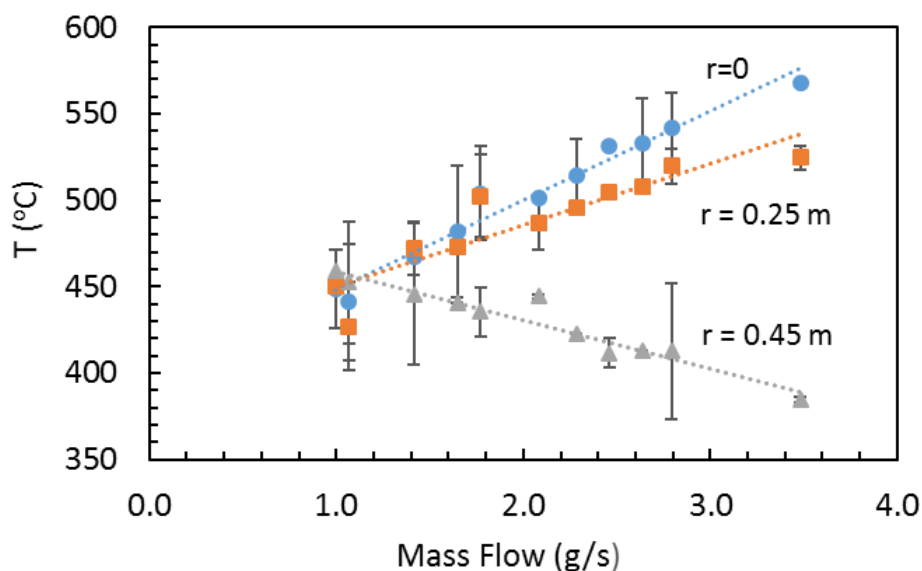


Figure 7. The measured surface temperature as a function of the fuel mass flow for three radial locations on the pool surface ($r = 0.00\text{ m}$, 0.25 m , and 0.45 m) for natural gas fires established in the 1.0 m burner. The data are also presented in Table A2.1 in Appendix 2. The lines represent best linear fits to the data.

5.4 Uncertainty Analysis

Uncertainties were estimated for all measured, calculated, and modeled parameters. For convenience, Table 3 summarizes the results. The uncertainties in the table are expressed as relative values in the form of percentages, rather than as absolute values, to facilitate comparison.

The expanded uncertainty in \dot{Q}_c was estimated as 10 % based on a propagation of uncertainty analysis and repeat measurements. [6] The expanded uncertainty in the values of χ_r was estimated as 17 % and was dominated by uncertainty in the local radiative heat flux and the mass flow rate. The expanded uncertainty in the measurement of \dot{Q}_b and χ_b was 4 % [6] and 6 %, respectively. The measurement and uncertainty analysis assumed that heat losses from the duct to the surroundings were small relative to transported enthalpy. From this information and Eq. 1, the expanded uncertainty of χ_a was estimated as 21 %. For fires in which \dot{Q}_c was not measured, χ_c was calculated using Eq. 1, assuming a value of unity for χ_a , the expanded uncertainty of χ_c was estimated as 18 %. Likewise, the expanded uncertainty in \dot{Q}_c and χ_c was 10 % and 11 %, respectively, using Eqs. 10 and 2. A propagation of uncertainty analysis [20] showed that the expanded uncertainty in the calculated value of L using Eq. 15 was proportional to the expanded uncertainty in \dot{m} multiplied by a factor related to the flame geometry: $0.4(1 + 1.02 D/L)$, which on average was 4 %.

Table 3. Uncertainty Scorecard: Expanded Uncertainty of Measured, Calculated, and Modeled Parameters.

Parameter	Relevant Equation/Figure	Expanded Uncertainty (%)		
		Measured	Calculated	Modeled
\dot{m}	Fig. 1	4	-	-
L	Eq. 15	-	4	-
\dot{q}''	Fig. 1	16	-	-
\dot{Q}_r	Eq. 9	-	16	-
\dot{Q}_c	Eq. 10	10	-	-
\dot{Q}_b	Eqs. 11 / Eq. 13	4	-	17
\dot{Q}_{bc}	Eq. 12	-	-	8
\dot{Q}_{br}	Eq. 13	-	-	15
χ_r	Eqs. 2, 9	17	-	-
χ_c	Eqs. 2, 10 / Eqs. 1, 2, 3*	11	18	-
χ_a	Eq. 1	-	21	-
χ_b	Eqs. 2, 11 / Eq. 5	6	-	18
χ_{bc}	Eq. 9	-	-	9
χ_{br}	Eq. 14	-	-	15
χ_{rad}	Eq. 8	-	-	23

* assuming a value of unity for χ_a

6. COMPARISON OF HEAT FEEDBACK MODEL RESULTS WITH MEASUREMENTS

Figures 8 – 10 compare the measured and calculated values of χ_b as a function of heat release rate normalized by the pool surface area, which is directly related to the mass flux as seen in Figs. 3 – 5. The measurement of χ_b is fairly simple (see Eq. 11), involving measurement of the water cooling mass flow and its temperature difference through the burner, in addition to the measurement of the fuel flow. Calculated values were determined from Eqs. 12 – 16. Measured values of χ_b are shown in Figures 3 - 5 and tabulated in Tables A1.1- A1.3 in Appendix 1. The values of χ_b were relatively large (> 0.2) for small mass flux ($100 \text{ g/m}^2\text{-s}$ to $200 \text{ g/m}^2\text{-s}$) and rapidly decreased as the mass flux increased.

The expanded uncertainty of the measurement of χ_b was 6 % on average (see Table 3), which is smaller than the symbols in the figures, whereas the model uncertainty was 18 % based on uncertainty in the model input parameters. About one-third of the measurements agree within the expanded combined uncertainty with the model results, whereas the rest of the measurements are outside the expanded uncertainty though typically not by much. The worst agreement was for the acetylene fires in the 0.35 m burner (see Figure 10). The reason for this is unclear, but may be attributed to the copious amounts of soot generated only in that fire (for the conditions tested in this study), a portion of which was observed to settle on the burner surface.

Although the model is not completely in agreement with all of the measurements within experimental uncertainty, the general trend of χ_b decreasing with mass flux appears to be correct (see Figures 8 - 10). The results confirm the importance of “blowing” on convective heat transfer to the horizontal burner surface for small values of the heat release rate per unit surface area. This phenomenon may have significance for burning solids in a horizontal configuration such as thermoplastics, wood, or furniture, particularly in the early stages of a fire when the burning rate is relatively small.

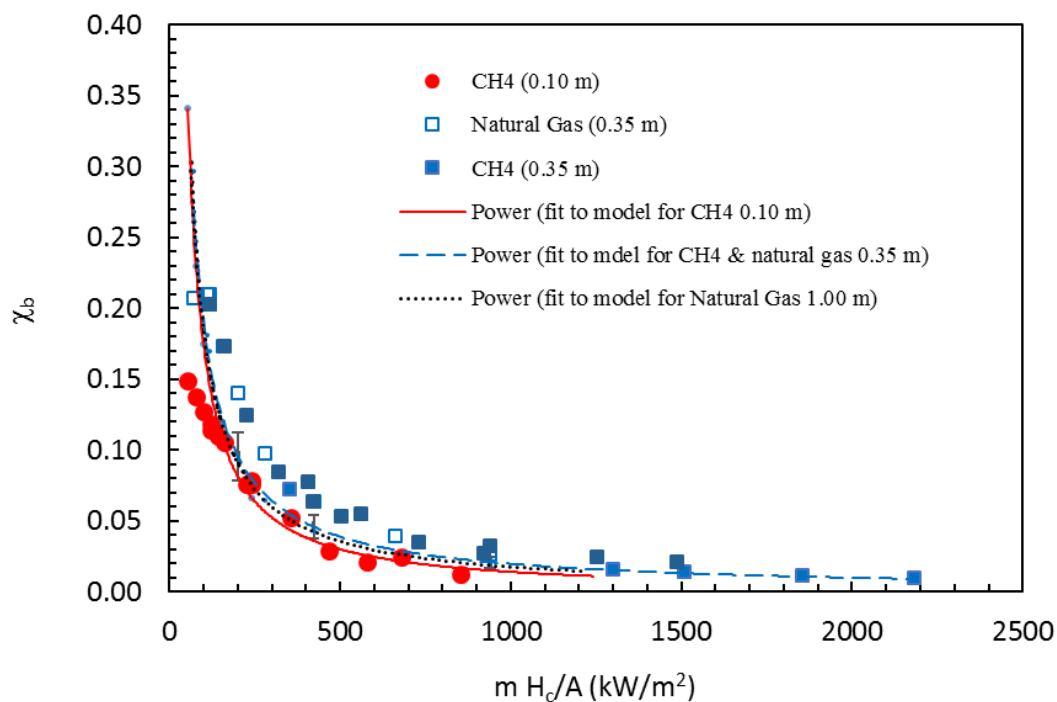


Figure 8. The measured (symbols) and model (lines) for the total heat feedback (χ_b) to the burner for methane and natural gas fires as a function of the product of the heat release rate normalized by the pool surface area. A few representative expanded uncertainty bars for the model results are shown; the uncertainty bars for the measurements are less than the size of the symbols.

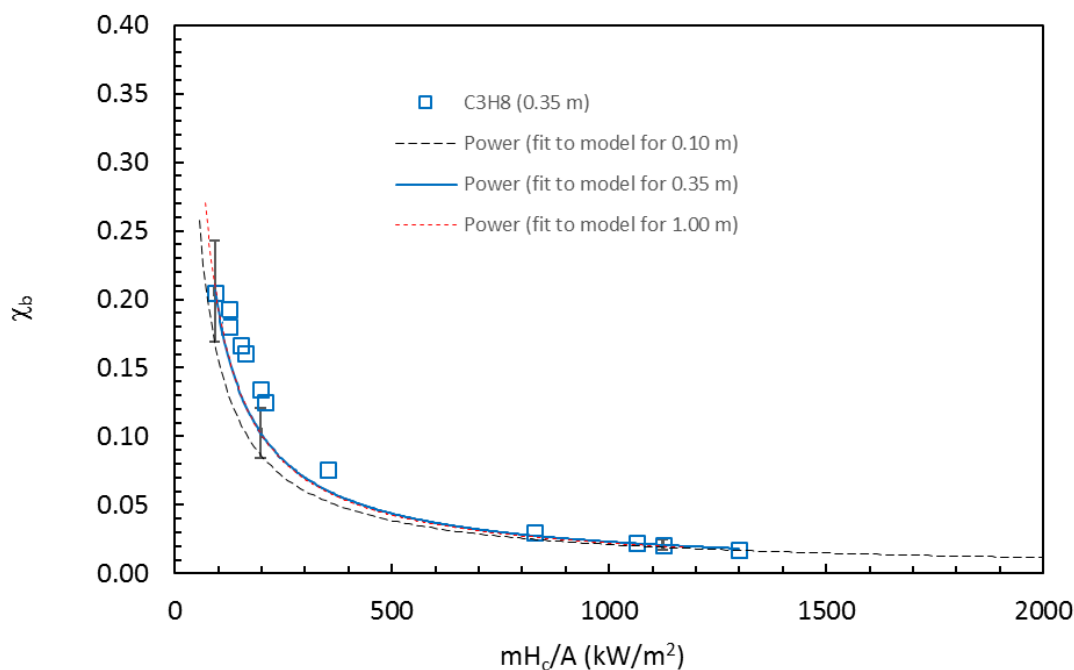


Figure 9. The measured (symbols) and model results (lines) for the total heat feedback (χ_b) to the burner for propane fires as a function of the product of the heat release rate normalized by the pool surface area. A few representative expanded uncertainty bars for the model results are shown; the uncertainty bars for the measurements are less than the size of the symbols.

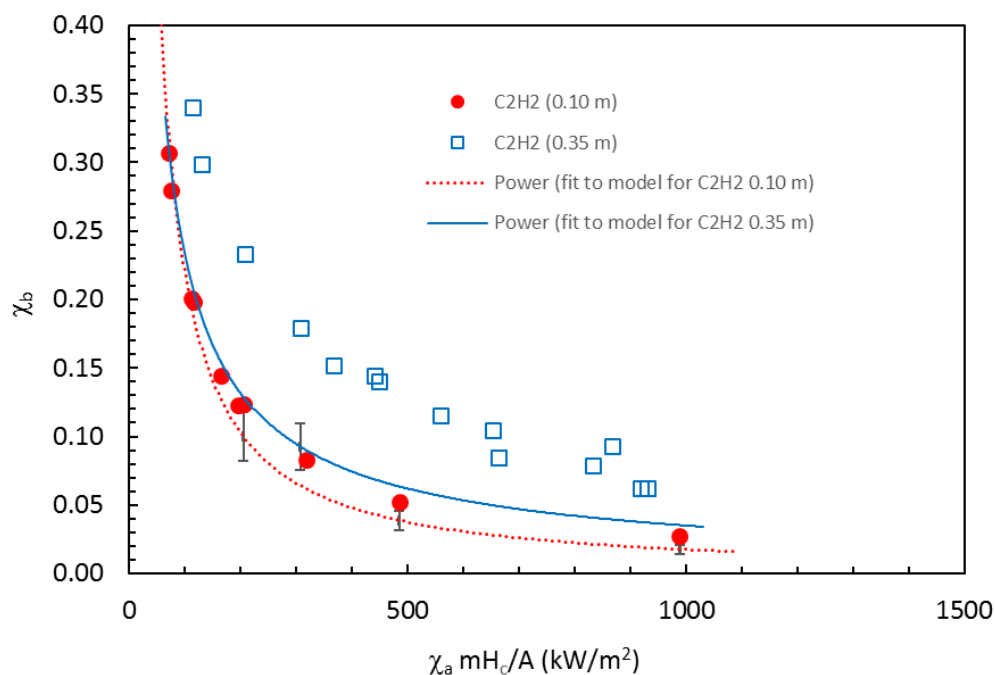


Figure 10. The measured (symbols) and model results (lines) for the total heat feedback (χ_b) to the 0.10 m and 0.35 m burners for acetylene fires as a function of the product of the heat release rate normalized by the pool surface area. A few representative expanded uncertainty bars for the model results are shown; the uncertainty bars for the measurements are less than the size of the symbols.

Using the model for χ_b (Eqs. 12 – 16), the relative importance of χ_{br} was compared to χ_{bc} . Figure 11 shows the calculated fractional radiative feedback to the fuel surface normalized by the total heat feedback ($\chi_{br}/(\chi_{br} + \chi_{bc})$) for the methane, natural gas, propane, and acetylene pool fires in the various burners tested here. For small blowing rates or heat release rates per unit surface area, as expected, convective heat feedback dominated radiative heat feedback, whereas for larger fires, radiation dominated.

Figure 12 shows the relationship between χ_r and χ_{rad} for all the modeling results for the three fuels. Also shown are values of χ_{br} . The Tables in Appendix 1 list the actual values of these parameters. As seen in the figure, the values of χ_r are within about 5 % of χ_{rad} .

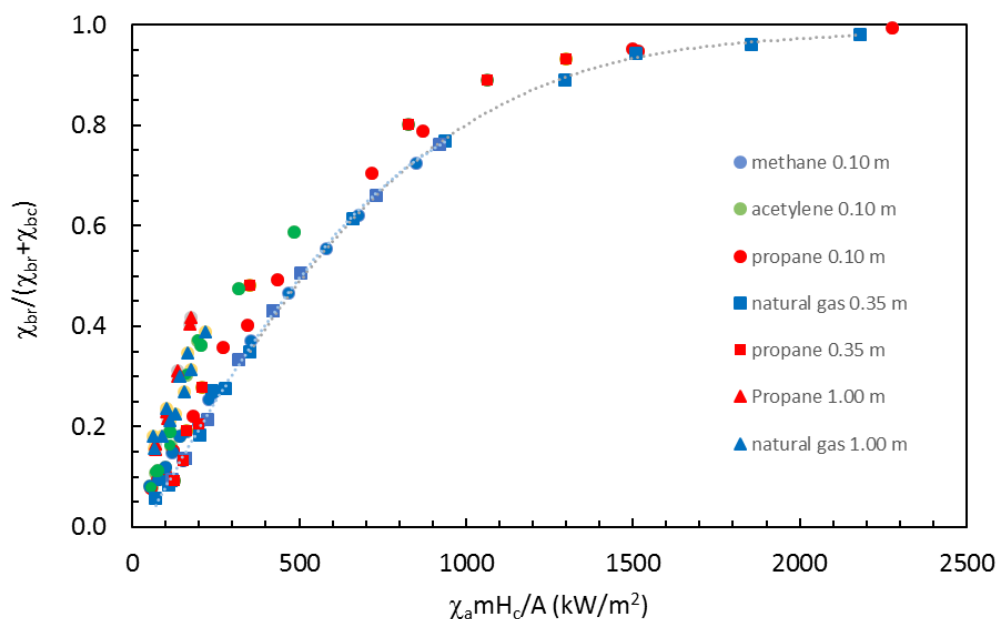


Figure 11. Model results (Eqs. 12 -16) for the fractional radiative feedback to the fuel surface ($\chi_{br}/(\chi_{br} + \chi_{bc})$) for the methane, natural gas, propane, and acetylene pool fires as a function of the actual heat release per unit burner surface area.

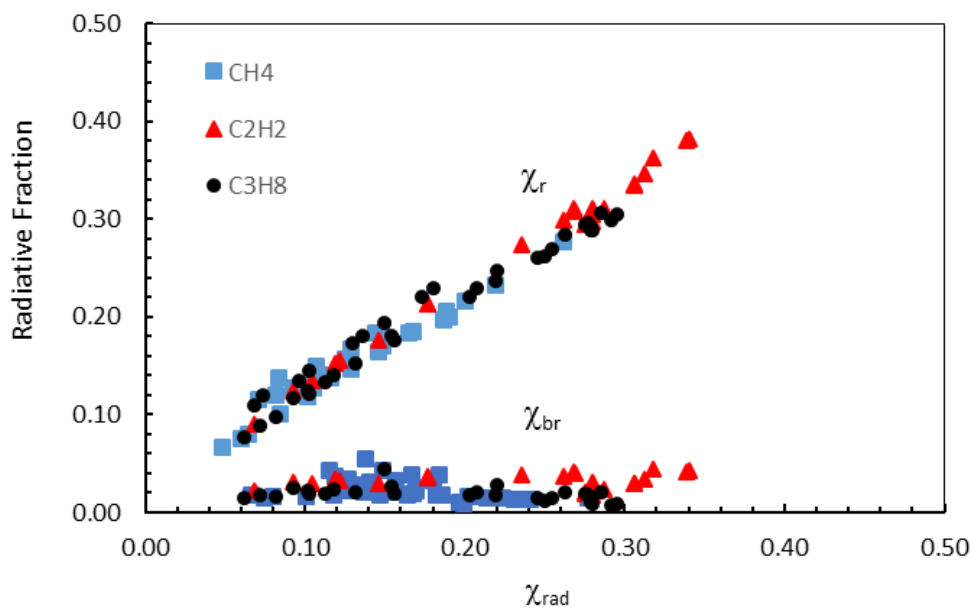


Figure 12. Model results showing the relationship of χ_r and χ_{br} in terms of χ_{rad} for the three fuels.

7. CONCLUSIONS

In summary, a series of measurements were conducted to characterize the energetics of a number of gaseous pool fires. The measurements included the distribution of radiative heat flux emitted to the surroundings as a function of fuel mass flux for different burners sizes and fuel types. This information was used to calculate the fraction of energy emitted as radiation. Heat transfer to the burner and sensible enthalpy transfer to the surroundings by convection were also measured. For all fuels and burner sizes considered here, the radiative fraction increased and the enthalpy loss to the burner decreased as a function of increasing fuel mass flux. A previously developed model was applied to estimate the convective heat feedback to the burner. The measured total fractional heat feedback to the burner was compared to its calculated value. To fully define these fires for model validation, future work is needed to directly measure χ_{br} , χ_a , χ_c , and the yields of smoke and carbon monoxide.

8. ACKNOWLEDGEMENTS

The author is grateful to the many people whose hard work, helpful discussions, and positive disposition made this report possible, including Paul Borthwick, Robert Buch, Laurean DeLauter, Jay Gore, Takashi Kashiwagi, Michael Klassen, Katsu Konishi, Dave Mattingly, Kevin McGrattan, Gary Rodarmel, Jiann Yang, and Richard Zile. Funding from NIST's Standard Reference Data Enhancement Project is gratefully acknowledged.

9. REFERENCES

1. Peacock, R.D., Reneke, P.A., Forney, G.P., CFAST – Consolidated Model of Fire Growth and Smoke Transport (Version 6), NIST Special Publication 1041r1, March 2013.
<http://dx.doi.org/10.6028/NIST.SP.1041r1>
2. McGrattan, K., McDermott, R., Hostikka, S., Floyd, J., Weinschenk, C., Overholt, K., Fire Dynamics Simulator, NIST Special Publication 1019, Sixth Edition, April 2016.
<http://dx.doi.org/10.6028/NIST.SP.1019>
3. Hamins, A., Fischer, S., Kashiwagi, T., Klassen, M., and Gore, J., Heat Feedback to the Fuel Surface in Pool Fires, *Combust. Sci. Tech.*, **97**, 37-62 (1993).
4. Akita, K. and Yumoto, T., Heat Transfer in Small Pools of Liquid Methanol, *Proceedings of the Tenth Sym. (Int.) on Combustion*, The Combustion Institute, 943 (1965).
5. Hostikka, S., McGrattan, K., and Hamins, A., Numerical Modeling of Small and Moderate-Scale Pool Flames using Large Eddy Simulation and Finite Volume Method for Radiation, *Proceedings Seventh Int. Sym. on Fire Safety Science*, 383-394 (2003).
6. Hamins, A., Konishi, K., Borthwick, P., and Kashiwagi, T., Global Properties of Gaseous Pool Fires, *Proceedings The Twenty-Sixth Sym. (Int.) on Combustion*, The Combustion Institute, 1429-1436 (1996).
7. Hamins, A., Klassen, M., Gore, J., and Kashiwagi, T., Estimate of Flame Radiance via a Single Location Measurement in Liquid Pool Fires. *Combustion and Flame*, 86:223-228, 1991.
8. Klassen, M., Gore, J., Hamins, A., and Kashiwagi, T., Radiative Heat Feedback in a Toluene Pool Fire, *Proceedings Twenty-Fourth Sym. (Int.) on Combustion*, The Combustion Institute, 1713-1719 (1992).
9. Gore, J., Klassen, M., Hamins, A., and Kashiwagi, T., Fuel Property Effects on Burning Rates and Radiative Transfer from Liquid Pool Flames, *Proceedings of the Third International Symposium on Fire Safety Science*, 395-404 (1991).
10. M. Klassen and J.P. Gore, Structure and Radiation Properties of Pool Fires, *NIST Report GCR-94-651*, National Institute of Standards and Technology, Gaithersburg, MD, June 1994.
11. Buch, R., Hamins, A., Konishi, K., and Kashiwagi, T., Mass Vaporization Rates and Radiative Emission of Pool Burning of Silicone Fluids, *Combust. Flame*, **108**, 118-126 (1997).
12. Hamins, A., Kashiwagi, T., and Buch, R., Characteristics of Pool Fire Burning, in *Fire Resistance of Industrial Fluids, ASTM STP 1284* (Eds: G. Totten and J. Reichel), American Society for Testing and Materials (ASTM) Publication Number 04-012840-12, W. Conshocken, PA, pp. 15-41 (1995).
13. Taylor, B.N. and Kuyatt, C.E., Guidelines for Evaluating and Expressing the Uncertainty of NIST Measurement Results, NIST TN 1297, National Institute of Standards and Technology, Gaithersburg, MD, Sept. 1994.
14. Pitts, W.M., Murthy, A.V., de Ris, J.L., Filtz, J-R, Nygard, K., Smith, D., Wetterlund, I., Round Robin Study of Total Heat Flux Gauges, *NIST Special Publication 1031*, National Institute of Standards and Technology, Gaithersburg, MD, October 2004.

-
15. Pitts, W.M., Lawson, J.R., and Shields, J.R., Report of Test FR 4014, NIST/BFRL Calibration System for Heat-Flux Gages, National Institute of Standards and Technology, Gaithersburg, MD, August 6, 2001.
 16. Orloff, L. and de Ris, J., Froude Modeling of Pool Fires, *Proceedings of the Nineteenth Symp. (Int.) on Combustion*, The Combustion Institute, 885-895 (1982).
 17. Orloff, L. and de Ris, J., Froude Modeling of Pool Fires, *Technical Report FMRC OHON3.BU, RC81-BT-9*, Factory Mutual Research Corp., Norwood, MA, October 1983.
 18. Heskestad, G., Fire Plumes, Flame Height, and Air Entrainment, Chapter 13 of the *SFPE Handbook of Fire Protection Engineering* (Fifth Ed.; M. Hurley Ed.), Springer, New York, 396 – 428, 2016. DOI 10.1007/978-1-4939-2565-0_13
 19. Khan, M.M. and Tewarson, A., Combustion Characteristics of Materials and Generation of Fire Products, Chapter 36 in the *SFPE Handbook of Fire Protection Engineering* (Fifth Ed.; M. Hurley Ed.), Springer, New York, 1143 – 1232, 2016. DOI 10.1007/978-1-4939-2565-0_36
 20. Hamins, A., McGrattan, K., and Peacock, R., Experimental Uncertainty, Volume 2 in Verification and Validation of Selected Fire Models for Nuclear Power Plant Applications, *NRC Report NUREG 1824*, U.S. Nuclear Regulatory Commission, Rockville, MD, January 2006.

APPENDIX 1. SUMMARY OF THE MEASUREMENT RESULTS

Table A1.1 Summary of gaseous methane/natural gas fire experiments including the fire diameter (D), fuel heat of combustion (H_c), mass flux (\dot{m}), value of R_o (the radial distance from the burner center to the vertical radiometer array), idealized heat release rate ($\dot{m}H_c$), radiative fraction (χ_r), convective enthalpy fraction (χ_c), enthalpy fraction lost to the burner (χ_b), and the filenames containing the data. The measurement uncertainties are listed in Table 3.

<i>Test #</i>	<i>D</i> (m)	<i>H_c</i> (kJ/g)	\dot{m} (g/s)	<i>R_o</i> (m)	$\dot{m}H_c$ (kW)	χ_r	χ_c^{**}	χ_b	χ_{rad}^{***}	Data File	Original Test Name
M1	0.10	50.03	0.00845	0.13	0.42	0.10	0.75	0.15	0.13	M1.csv	6/14 #1
M2	0.10	50.03	0.0122	0.13	0.61	0.10	0.76	0.14	0.13	M2.csv	6/14 #2
M3	0.10	50.03	0.0155	0.13	0.78	0.11	0.76	0.13	0.13	M3.csv	6/14 #3
M4	0.10	50.03	0.0222	0.13	1.11	0.14	0.75	0.11	0.16	M4.csv	6/14 #4
M5	0.10	50.03	0.0378	0.13	1.89	0.14	0.78	0.076	0.16	M5.csv	6/14 #5
M6	0.35	49.40*	0.226	0.40	11.15	0.065	0.73	0.21	0.08	M6.csv	3/17 #10
M7	0.35	49.40*	0.310	0.40	15.30	0.084	0.74	0.17	0.10	M7.csv	3/17 #12
M8	0.35	49.40*	0.212	0.40	10.49	0.060	0.73	0.21	0.075	M8.csv	3/18 #13
M9	0.35	49.40*	0.135	0.40	6.67	0.049	0.74	0.21	0.066	M9.csv	3/18 #14
M10	0.35	49.40*	0.391	0.64	19.31	0.101	0.76	0.14	0.12	M10.csv	3/18 #15
M11	0.35	49.40*	0.546	0.63	26.97	0.129	0.77	0.098	0.15	M11.csv	3/18 #16
M12	0.35	49.40*	0.822	0.81	40.62	0.165	0.77	0.064	0.18	M12.csv	3/18 #17
M13	0.35	49.40*	1.285	0.92	63.49	0.188	0.77	0.040	0.21	M13.csv	3/18 #19
M14	0.35	49.40*	1.828	0.92	90.31	0.201	0.77	0.027	0.22	M14.csv	3/18 #20
M15	0.35	50.03	3.567	0.92	178.43	0.187	0.80	0.012	0.20	M15.csv	3/18 #21
M16	0.35	50.03	4.194	0.92	209.82	0.190	0.80	0.010	0.20	M16.csv	3/21 #22
M17	0.35	50.03	0.679	0.92	33.98	0.146	0.78	0.073	0.16	M17.csv	3/21 #23
M18	0.35	50.03	2.904	0.90	145.28	0.261	0.72	0.014	0.28	M18.csv	4/8 #1
M19	0.35	50.03	2.495	0.90	124.85	0.219	0.77	0.016	0.23	M19.csv	4/8 #2
M20	1.00	49.13*	0.997	1.00	49.00	0.083	0.61	0.30*	0.14	M20.csv	5/3 #7
M21	1.00	49.13*	1.648	1.00	80.96	0.107	0.71	0.18*	0.15	M21.csv	5/3 #9
M22	1.00	49.13*	2.282	1.00	112.12	0.128	0.74	0.13*	0.17	M22.csv	5/3 #11
M23	1.00	49.13*	2.635	1.00	129.46	0.144	0.74	0.11*	0.18	M23.csv	5/3 #12
M24	1.00	49.29*	1.069	0.79	52.69	0.071	0.65	0.28*	0.12	M24.csv	5/18 #13
M25	1.00	49.29*	1.414	0.79	69.72	0.082	0.71	0.21*	0.12	M25.csv	5/18 #14
M26	1.00	49.29*	1.771	0.79	87.30	0.093	0.75	0.16*	0.13	M26.csv	5/18 #15
M27	1.00	49.29*	2.081	0.79	102.58	0.095	0.77	0.14*	0.13	M27.csv	5/18 #16
M28	1.00	49.29*	2.462	0.79	121.33	0.110	0.75	0.12*	0.14	M28.csv	5/18 #17
M29	1.00	49.29*	2.793	0.79	137.65	0.125	0.77	0.10*	0.16	M29.csv	5/18 #18
M30	1.00	49.29*	3.482	0.79	171.61	0.148	0.77	0.085*	0.18	M30.csv	5/18 #19

* calculated using Eqs. 5 and 12-16; ** calculated using Eq. 3, assuming $\chi_a = 1$; *** calculated using Eqs. 8 and 14.

Table A1.2 Summary of gaseous propane fire experiments including the fire diameter (D), mass flux (\dot{m}), the value of R_o (radial distance from the burner center to the vertical radiometer array), idealized heat release rate ($\dot{m} H_c$), radiative fraction (χ_r), convective enthalpy fraction (χ_c), enthalpy fraction lost to the burner (χ_b), χ_{rad} and the filenames containing the data. The measurement uncertainties are listed in Table 3.

Test #	D (m)	\dot{m} (g/s)	R_o (m)	$\dot{m} H_c$ (kW)	χ_r	χ_c^{**}	χ_b	χ_{rad}^{***}	Data File	Original Test Name
P1	0.10	0.0582	0.26	2.70	0.20	0.72	0.046*	0.22	P1.csv	5/27 #1
P2	0.10	0.148	0.26	6.84	0.25	0.70	0.019*	0.27	P2.csv	5/31 #2
P3	0.10	0.254	0.26	11.78	0.28	0.69	0.013*	0.29	P3.csv	5/31 #3
P4	0.10	0.386	0.37	17.89	0.28	0.68	0.010*	0.29	P4.csv	5/31 #4
P5	0.10	0.543	0.37	25.16	0.30	0.67	0.009*	0.30	P5.csv	5/31 #5
P6	0.10	0.796	0.49	36.90	0.29	0.66	0.008*	0.30	P6.csv	5/31 #6
P7	0.10	0.0095	0.13	0.44	0.09	0.76	0.32*	0.12	P7.csv	6/10 #11
P8	0.10	0.0169	0.13	0.78	0.10	0.75	0.18*	0.12	P8.csv	6/10 #12
P9	0.10	0.0130	0.13	0.60	0.10	0.75	0.23*	0.12	P9.csv	6/10 #13
P10	0.10	0.0210	0.13	0.97	0.13	0.74	0.14*	0.15	P10.csv	6/10 #14
P11	0.10	0.0311	0.13	1.44	0.16	0.73	0.090*	0.18	P11.csv	6/10 #15
P12	0.10	0.0463	0.13	2.15	0.21	0.72	0.059*	0.23	P12.csv	6/10 #16
P13	0.10	0.0735	0.19	3.41	0.22	0.71	0.036*	0.24	P13.csv	6/10 #17
P14	0.10	0.122	0.19	5.64	0.25	0.70	0.022*	0.26	P14.csv	6/10 #18
P15	0.10	0.257	0.28	11.89	0.25	0.69	0.012*	0.26	P15.csv	6/10 #19
P16	0.10	0.535	0.28	24.79	0.28	0.67	0.009*	0.29	P16.csv	6/10 #20
P17	0.35	0.732	0.92	33.94	0.22	0.70	0.076	0.25	P17.csv	3/21 #1
P18	0.35	2.694	0.92	124.8	0.28	0.71	0.017	0.30	P18.csv	3/21 #2
P19	0.35	0.431	0.57	20.00	0.15	0.72	0.13	0.18	P19.csv	3/21 #3
P20	0.35	0.336	0.57	15.59	0.12	0.72	0.16	0.14	P20.csv	3/21 #4
P21	0.35	0.409	0.39	18.98	0.11	0.75	0.14	0.13	P21.csv	3/21 #6
P22	0.35	0.316	0.39	14.64	0.08	0.75	0.17	0.098	P22.csv	3/21 #7
P23	0.35	2.334	0.68	108.1	0.28	0.70	0.021*	0.29	P23.csv	4/8 #9
P24	0.35	2.207	0.68	102.3	0.29	0.69	0.022	0.31	P24.csv	4/8 #10
P25	0.35	1.719	0.68	79.70	0.26	0.71	0.030	0.28	P25.csv	4/8 #11
P26	0.35	0.258	0.51	11.98	0.062	0.76	0.18	0.077	P26.csv	4/11 #12
P27	1.00	1.190	0.81	55.17	0.07	0.75	0.27*	0.11	P27.csv	4/20 #1
P28	1.00	1.761	0.81	81.65	0.10	0.75	0.19*	0.15	P28.csv	4/20 #2
P29	1.00	2.315	0.81	107.3	0.14	0.74	0.14*	0.18	P29.csv	4/20 #3
P30	1.00	2.943	1.00	136.4	0.17	0.73	0.12*	0.22	P30.csv	4/20 #4
P31	1.00	1.199	0.97	55.59	0.07	0.75	0.27*	0.12	P31.csv	5/23 #5
P32	1.00	1.779	0.97	82.46	0.10	0.75	0.18*	0.14	P32.csv	5/23 #6
P33	1.00	2.326	0.97	107.8	0.13	0.74	0.14*	0.17	P33.csv	5/23 #7
P34	1.00	2.963	0.97	137.3	0.18	0.73	0.12*	0.23	P34.csv	5/23 #8

* calculated using Eqs. 5 and 12-16.

** calculated using Eq. 3, assuming $\chi_a = 1$.

*** calculated using Eqs. 8 and 14.

Table A1.3 Summary of gaseous acetylene fire experiments including the fire diameter (D), mass flux (\dot{m}), value of R_o (radial distance from the burner center to the vertical radiometer array), idealized heat release rate ($\dot{m} H_c$), radiative fraction (χ_r), convective enthalpy fraction (χ_c), enthalpy fraction lost to the burner (χ_b), χ_{rad} , combustion efficiency (χ_a), and the filenames containing the data. The measurement uncertainties are listed in Table 3.

<i>Test</i>	D^* (m)	\dot{m} (g/s)	R_o (m)	$\dot{m} H_c$ (kW)	χ_r	χ_c	χ_b	χ_a	χ_{rad}^\dagger	Data File	Original Test Name
A1	0.10	0.00943	0.13	0.45	0.093	0.54*	0.37	1*	0.12	A1.csv	6/15 #1
A2	0.10	0.0116	0.13	0.56	0.12	0.57*	0.31	1*	0.15	A2.csv	6/15 #2
A3	0.10	0.0188	0.13	0.90	0.15	0.66*	0.20	1*	0.18	A3.csv	6/15 #3
A4	0.10	0.0267	0.13	1.29	0.24	0.62*	0.14	1*	0.27	A4.csv	6/15 #4
A5	0.10	0.0320	0.13	1.54	0.27	0.61*	0.12	1*	0.31	A5.csv	6/15 #5
A6	0.35	0.259	0.39	12.5	0.11	0.58**	0.30	0.99***	0.13	A6.csv	3/23 #5
A7	0.35	0.229	0.51	11.0	0.07	0.59**	0.34	1.00***	0.09	A7.csv	4/11 #6
A8	0.35	0.424	0.51	20.4	0.18	0.54**	0.23	0.95***	0.21	A8.csv	4/11 #7
A9	0.35	0.648	0.51	31.3	0.27	0.50**	0.18	0.95***	0.31	A9.csv	4/11 #8
A10	0.35	0.793	0.69	38.2	0.32	0.48**	0.15	0.95***	0.36	A10.csv	4/11 #9
A11	0.35	1.00	0.69	48.0	0.34	0.45**	0.14	0.93***	0.38	A11.csv	4/11 #10
A12	0.35	1.29	0.69	62.4	0.31	0.41**	0.12	0.84***	0.35	A12.csv	4/11 #11
A13	0.35	1.58	0.69	76.3	0.31	0.39**	0.10	0.80***	0.34	A13.csv	4/11 #12
A14	0.35	2.27	0.69	109.2	0.29	0.34**	0.078	0.71***	0.31	A14.csv	4/11 #13
A15	0.35	2.43	0.69	117.2	0.28	0.33**	0.080	0.70***	0.30	A15.csv	4/11 #14
A16	0.35	2.79	0.69	134.7	0.28	0.31**	0.062	0.65***	0.30	A16.csv	4/11 #15

* calculated using Eq. 3, assuming $\chi_a = 1$.
** measured (see Eq. 10).
*** calculated using Eq. 3
† calculated using Eqs. 8 and 14.

APPENDIX 2. BURNER SURFACE TEMPERATURES

This appendix contains tables and figures presenting the measured temperatures on the burner surface for fires in the 0.10 m and 1.0 m burners, and the water cooling inlet and outlet temperatures for fires in the 0.35 m burner. An overview of the organization of the data is presented in Table A2.1 below.

Table A2.1 Organization of the surface temperature data in this appendix (Appendix 2).

Fuel	Diameter (m)	Table Number	Figure Number
Methane/ Natural Gas	0.10	2.2	2.1
	0.35	2.3	
	1.00	2.4	
Propane	0.10	2.5	2.2
	0.35	2.6	
	1.00	2.7	
Acetylene	0.10	2.8	2.4
	0.35	2.9	

Table A2.2 The measured surface temperature and standard uncertainty for the 0.10 m diameter methane experiments as a function of r (see Figure 1), the radial distance from the burner center. T_{avg} is the area-weighted average surface temperature. The standard uncertainty is also listed.

Test	$T(r=0.00)$ (°C)	$T(r=0.025\text{ m})$ (°C)	$T(r=0.045\text{ m})$ (°C)	T_{avg} (°C)
M1	346 ± 2	354 ± 2	218 ± 2	291 ± 3
M2	317 ± 2	344 ± 2	260 ± 2	304 ± 3
M3	314 ± 2	374 ± 2	306 ± 2	340 ± 3
M4	296 ± 2	341 ± 2	343 ± 2	340 ± 3
M5	273 ± 2	344 ± 2	346 ± 2	342 ± 3

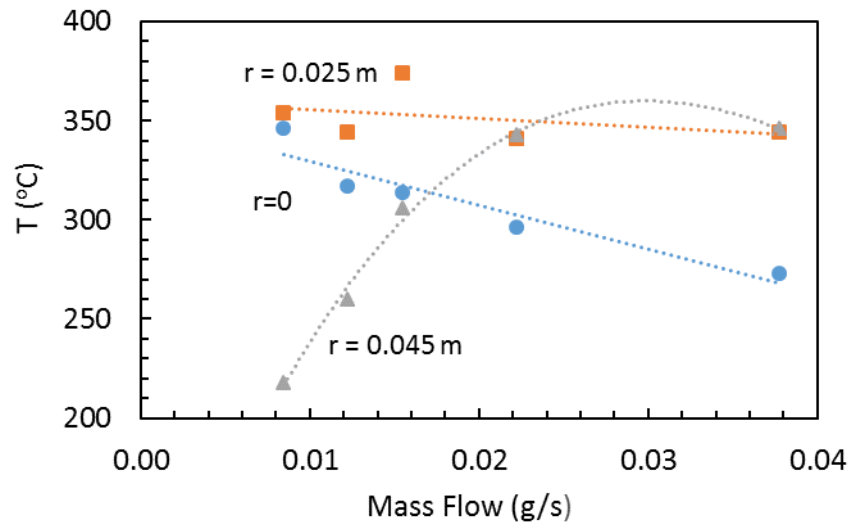


Figure A2.1 The measured surface temperature for the 0.10 m diameter methane experiments as a function of r , the radial distance from the burner center. The same data is presented in Table A2.1 along with the standard uncertainty. The dotted lines represent polynomial fits to the data.

Table A2.3 The measured temperature and standard uncertainty of the cooling water at the burner inlet and outlet for the 0.35 m diameter methane/natural gas experiments. T_{avg} is the average water temperature. The burner surface temperature is best represented by the outlet temperature. The surface temperature is assumed uniform and taken as approximately the outlet temperature.

<i>Test#</i>	<i>T</i> _{inlet} (°C)	<i>T</i> _{outlet} (°C)	<i>T</i> _{avg} (°C)
M6	18 ± 2	58 ± 2	38 ± 3
M7	17 ± 2	58 ± 2	41 ± 3
M8	18 ± 2	52 ± 2	34 ± 3
M9	18 ± 2	42 ± 2	24 ± 3
M10	18 ± 2	61 ± 2	43 ± 3
M11	18 ± 2	60 ± 2	42 ± 3
M12	17 ± 2	61 ± 2	44 ± 3
M13	15 ± 2	58 ± 2	42 ± 3
M14	15 ± 2	56 ± 2	41 ± 3
M15	15 ± 2	54 ± 2	39 ± 3
M16	18 ± 2	58 ± 2	40 ± 3
M17	18 ± 2	65 ± 2	47 ± 3
M18	12 ± 2	45 ± 2	33 ± 3
M19	12 ± 2	45 ± 2	33 ± 3

Table A2.4 Measured surface temperature for the 1.00 m diameter natural gas fire experiments as a function of r (see Figure 1), the radial distance from the burner center. T_{avg} is the calculated area-weighted average surface temperature. The standard uncertainty is also listed. This data is also presented (and discussed) in Figure 7 in the main body of this report.

T_{est}	$T(r=0)$ (°C)	$T(r=0.25\text{ m})$ (°C)	$T(r=0.45\text{ m})$ (°C)	T_{avg} (°C)
M20 *	448 ± 27	450 ± 15	459 ± 20	454 ± 37
M21 *	482 ± 27	473 ± 15	441 ± 20	459 ± 37
M22 *	514 ± 27	496 ± 15	423 ± 20	463 ± 37
M23 *	533 ± 27	508 ± 15	413 ± 20	465 ± 37
M24	452 ± 23	427 ± 26	453 ± 35	455 ± 49
M25	470 ± 34	472 ± 16	446 ± 41	457 ± 55
M26	488 ± 38	502 ± 24	435 ± 14	459 ± 47
M27	501 ± 27	487 ± 16	444 ± 2	461 ± 31
M28	531 ± 21	505 ± 4	412 ± 9	464 ± 23
M29	542 ± 26	520 ± 10	413 ± 40	466 ± 49
M30	568 ± 20	525 ± 7	385 ± 2	471 ± 22
* best fits interpolating results from M24 – M30 as a function of fuel mass flow.				

Table A2.5 The measured surface temperature and standard uncertainty for the 0.10 m diameter propane fire experiments as a function of r (see Figure 1), the radial distance from the burner center. T_{avg} is the area-weighted average surface temperature.

T_{test}	$T(r=0)$ (°C)	$T(r=0.025\text{ m})$ (°C)	$T(r=0.045\text{ m})$ (°C)	T_{avg} (°C)
P1	241 ± 2	337 ± 2	311 ± 2	321 ± 3
P2	152 ± 2	203 ± 2	304 ± 2	239 ± 3
P3	145 ± 2	143 ± 2	221 ± 2	179 ± 3
P4	129 ± 2	135 ± 2	207 ± 2	168 ± 3
P5	109 ± 2	124 ± 2	205 ± 2	161 ± 3
P6	97 ± 2	104 ± 2	188 ± 2	143 ± 3
P7	366 ± 2	406 ± 2	305 ± 2	358 ± 3
P8	289 ± 2	376 ± 2	355 ± 2	363 ± 3
P9	313 ± 2	379 ± 2	276 ± 2	329 ± 3
P10	291 ± 2	366 ± 2	338 ± 2	351 ± 3
P11	271 ± 2	343 ± 2	351 ± 2	344 ± 3
P12	234 ± 2	310 ± 2	338 ± 2	320 ± 3
P13	196 ± 2	241 ± 2	309 ± 2	271 ± 3
P14	175 ± 2	177 ± 2	271 ± 2	221 ± 3
P15	127 ± 2	139 ± 2	204 ± 2	169 ± 3
P16	81 ± 2	84 ± 2	167 ± 2	122 ± 3

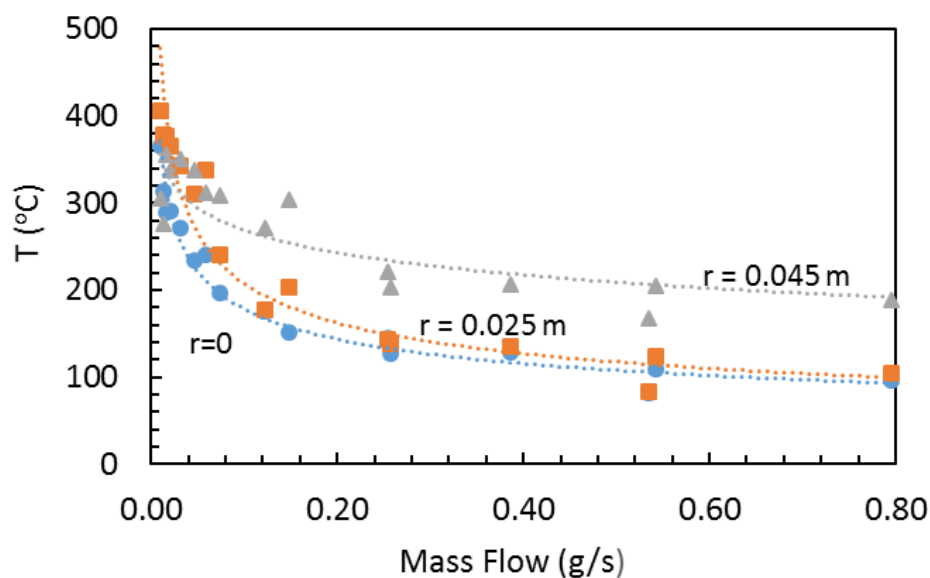


Figure A2.2 The measured surface temperature for the 0.10 m diameter propane experiments as a function of r , the radial distance from the burner center. The same data are presented in Table A2.3 along with the standard uncertainty.

Table A2.6 The measured temperature of the cooling water at the burner inlet and outlet for the 0.35 m diameter propane fire experiments. T_{avg} is the average water temperature. The surface temperature is assumed uniform and taken as approximately the outlet temperature. The standard uncertainty is also listed.

<i>Test</i>	<i>T_{inlet}</i> (°C)	<i>T_{outlet}</i> (°C)	<i>T_{avg}</i> (°C)
P17	18 ± 2	67 ± 2	49 ± 3
P18	18 ± 2	60 ± 2	42 ± 3
P19	20 ± 2	64 ± 2	44 ± 3
P20	18 ± 2	62 ± 2	44 ± 3
P21	17 ± 2	62 ± 2	45 ± 3
P22	16 ± 2	59 ± 2	43 ± 3
P23	12 ± 2	45 ± 2	33 ± 3
P24	12 ± 2	48 ± 2	36 ± 3
P25	12 ± 2	50 ± 2	38 ± 3
P26	19 ± 2	57 ± 2	38 ± 3

Table A2.7 Measured surface temperature and standard uncertainty for the 1.00 m diameter propane fire experiments as a function of r (see Figure 1), the radial distance from the burner center. T_{avg} is the area-weighted average surface temperature.

T_{test}	$T(r=0)$ (°C)	$T(r=0.25\text{ m})$ (°C)	$T(r=0.45\text{ m})$ (°C)	T_{avg} (°C)
P27	466 ± 2	469 ± 2	459 ± 2	465 ± 3
P28	503 ± 2	487 ± 2	430 ± 2	464 ± 3
P29	560 ± 2	513 ± 2	419 ± 2	476 ± 3
P30	607 ± 2	540 ± 2	397 ± 2	484 ± 3
P31	466 ± 2	469 ± 2	459 ± 2	465 ± 3
P32	503 ± 2	487 ± 2	430 ± 2	465 ± 3
P33	560 ± 2	513 ± 2	419 ± 2	476 ± 3
P34	607 ± 2	540 ± 2	397 ± 2	484 ± 3

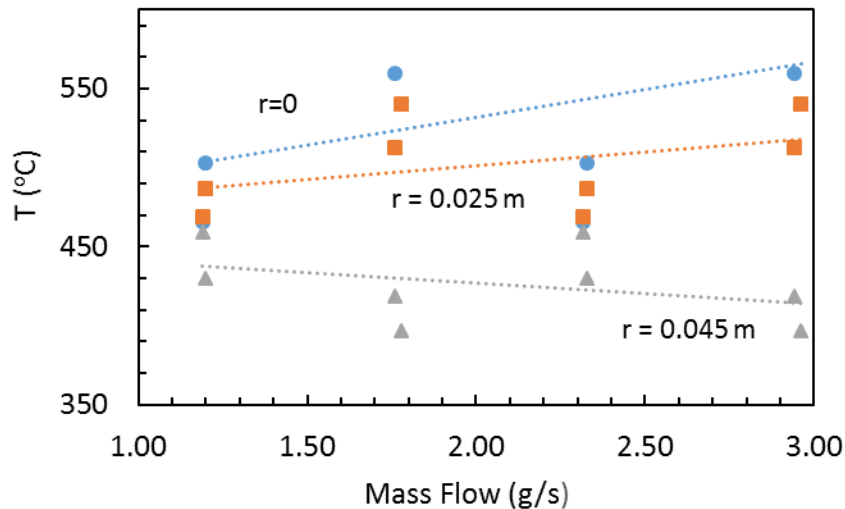


Figure A2.3 The measured surface temperature for the 1.00 m diameter propane experiments as a function of r , the radial distance from the burner center. The same data are presented in Table A2.5 along with the standard measurement uncertainty.

Table A2.8 Measured surface temperature and standard uncertainty for the 0.10 m diameter acetylene fire experiments as a function of r (see Figure 1), the radial distance from the burner center. T_{avg} is the area weighted average temperature.

T_{test}	$T(r=0)$ (°C)	$T(r=0.025\text{ m})$ (°C)	$T(r=0.045\text{ m})$ (°C)	T_{avg} (°C)
A1	375 ± 2	483 ± 2	360 ± 2	422 ± 3
A2	386 ± 2	437 ± 2	414 ± 2	424 ± 3
A3	360 ± 2	466 ± 2	457 ± 2	448 ± 3
A4	395 ± 2	459 ± 2	463 ± 2	458 ± 3
A5	407 ± 2	469 ± 2	450 ± 2	458 ± 3

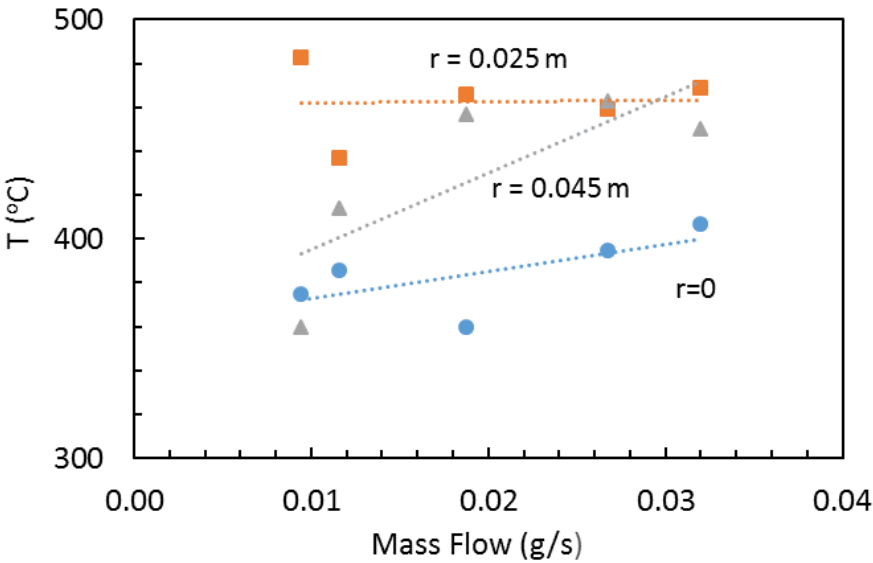


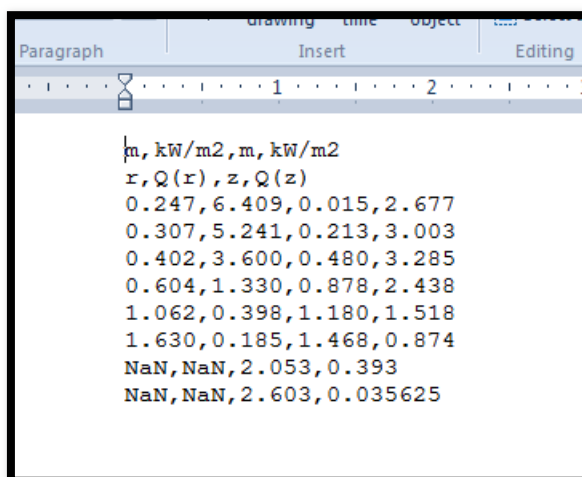
Figure A2.4 The measured surface temperature for the 0.10 m diameter acetylene experiments as a function of r , the radial distance from the burner center. The same data are presented in Table A2.6 along with the standard measurement uncertainty.

Table A2.9 The measured temperature and standard uncertainty of the cooling water at the burner inlet and outlet for the 0.35 m diameter acetylene fire experiments. T_{avg} is the average water temperature. The surface temperature is assumed uniform and taken as approximately the outlet temperature.

<i>Test</i>	<i>T_{inlet}</i> (°C)	<i>T_{outlet}</i> (°C)	<i>T_{avg}</i> (°C)
A6	19 ± 2	74 ± 2	47 ± 3
A7	19 ± 2	63 ± 2	41 ± 3
A8	19 ± 2	62 ± 2	41 ± 3
A9	18 ± 2	60 ± 2	39 ± 3
A10	16 ± 2	59 ± 2	38 ± 3
A11	15 ± 2	63 ± 2	39 ± 3
A12	13 ± 2	61 ± 2	37 ± 3
A13	13 ± 2	66 ± 2	40 ± 3
A14	13 ± 2	68 ± 2	41 ± 3
A15	13 ± 2	73 ± 2	43 ± 3
A16	13 ± 2	68 ± 2	41 ± 3

APPENDIX 3. RADIATIVE HEAT FLUX DISTRIBUTIONS

This appendix presents data that represents the radiative heat flux distributions for the 80 fires characterized in this study (see tables in Appendix 1). Each of the test results is maintained as an independent datafile, which is graphially presented here as a series of figures. Figure A3.1 below shows a screenshot from the file named “A6.csv” as viewed in Wordpad. The file contains four columns of comma delimited data, which represents the heat flux distribution from Test A6. The first and third columns are the r and z positions (see Figure 1) in meters. The second and fourth columns in the data files are the radial and vertical radiative heat fluxes in kW/m² (see Figure 1 in main text). Figures A 3.2 – A3.31 below represent the radial and vertical radiative heat fluxes as a function of location for the acetylene (Figures A 3.2 – A3.7), methane/natural gas (Figures A 3.8 – A3.17), and propane (Figures A 3.18 – A3.29) fires, respectively. The values of R_o are listed in the Tables in Appendix 1 (also see Figure 1 in the main body of this report). The values of R_o are listed in the Tables in Appendix 1 (see the discussion of Figure 1 for an explanation of the meaning of R_o). This data set is available upon request.



m, kW/m2, m, kW/m2			
r, Q(r), z, Q(z)			
0.247, 6.409, 0.015, 2.677			
0.307, 5.241, 0.213, 3.003			
0.402, 3.600, 0.480, 3.285			
0.604, 1.330, 0.878, 2.438			
1.062, 0.398, 1.180, 1.518			
1.630, 0.185, 1.468, 0.874			
NaN, NaN, 2.053, 0.393			
NaN, NaN, 2.603, 0.035625			

Figure A3.1 A screenshot of a MS WordPad file “A6.csv” that is composed of 4 columns of comma delimited numbers that represents measurement locations (in the r and z locations seen in Figure 1) and associated measured values of the radiative heat flux in the radial and vertical, $\dot{q}''(r)$ (or $Q(r)$) and $\dot{q}''(z)$ (or $Q(z)$) directions, respectively. The first two rows in the file provide the units and the parameter name, respectively. The symbol “NaN” (“not a number”) implies that there is no data available for a particular entry.

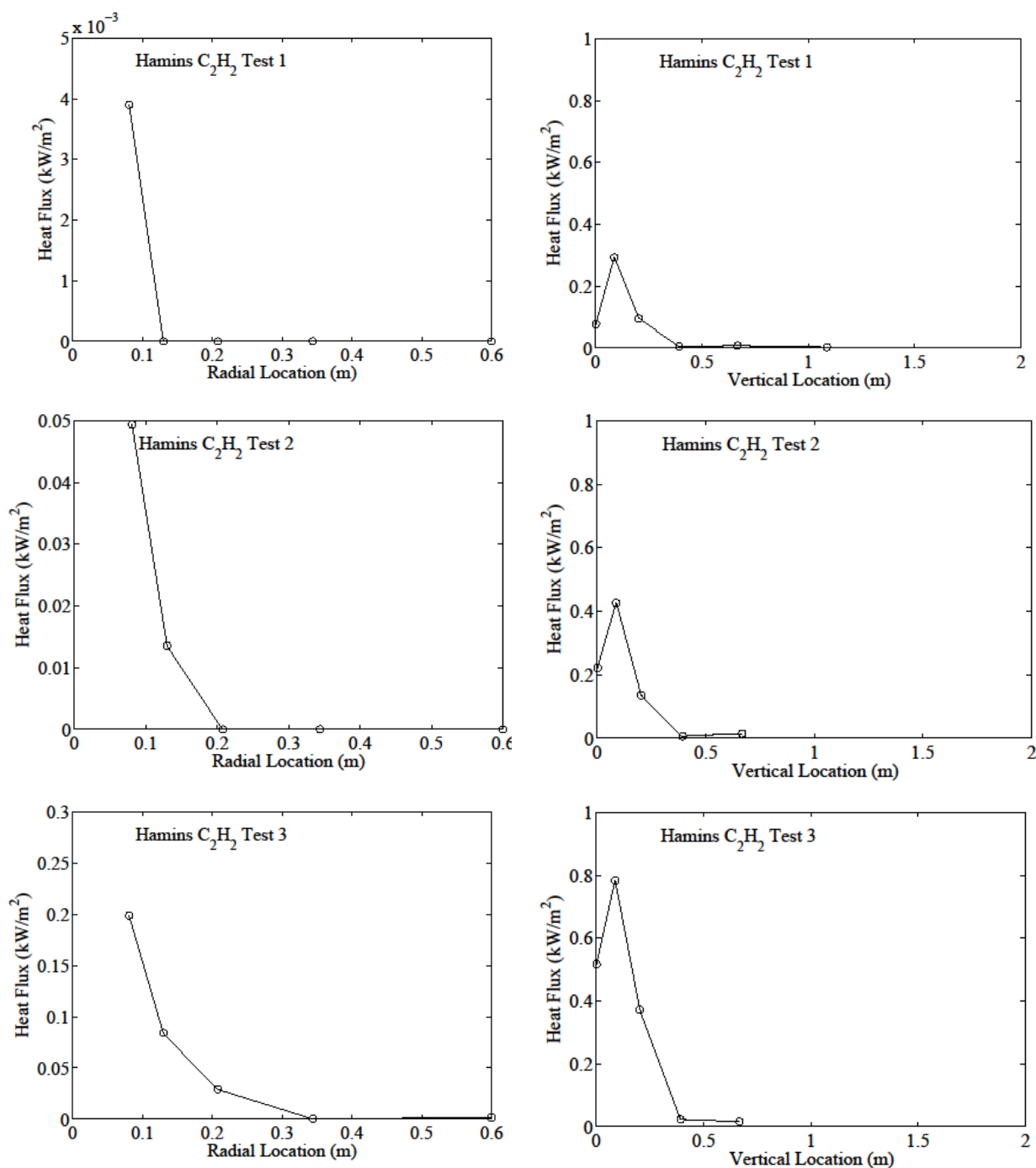


Figure A3.2 The measured local radiative heat flux distributions for 3 acetylene fire experiments (Tests A1 – A3) in the 0.1 m burner, showing the flux downwards as a function of radial distance from the burner center (left) and the radial flux as a function of vertical location above the plane defined by the burner surface for locations (R_o) away from the burner axis (right-hand figures; see values of R_o in the tables in Appendix 1). The lines connect the data points. The expanded measurement uncertainty was 16 %.

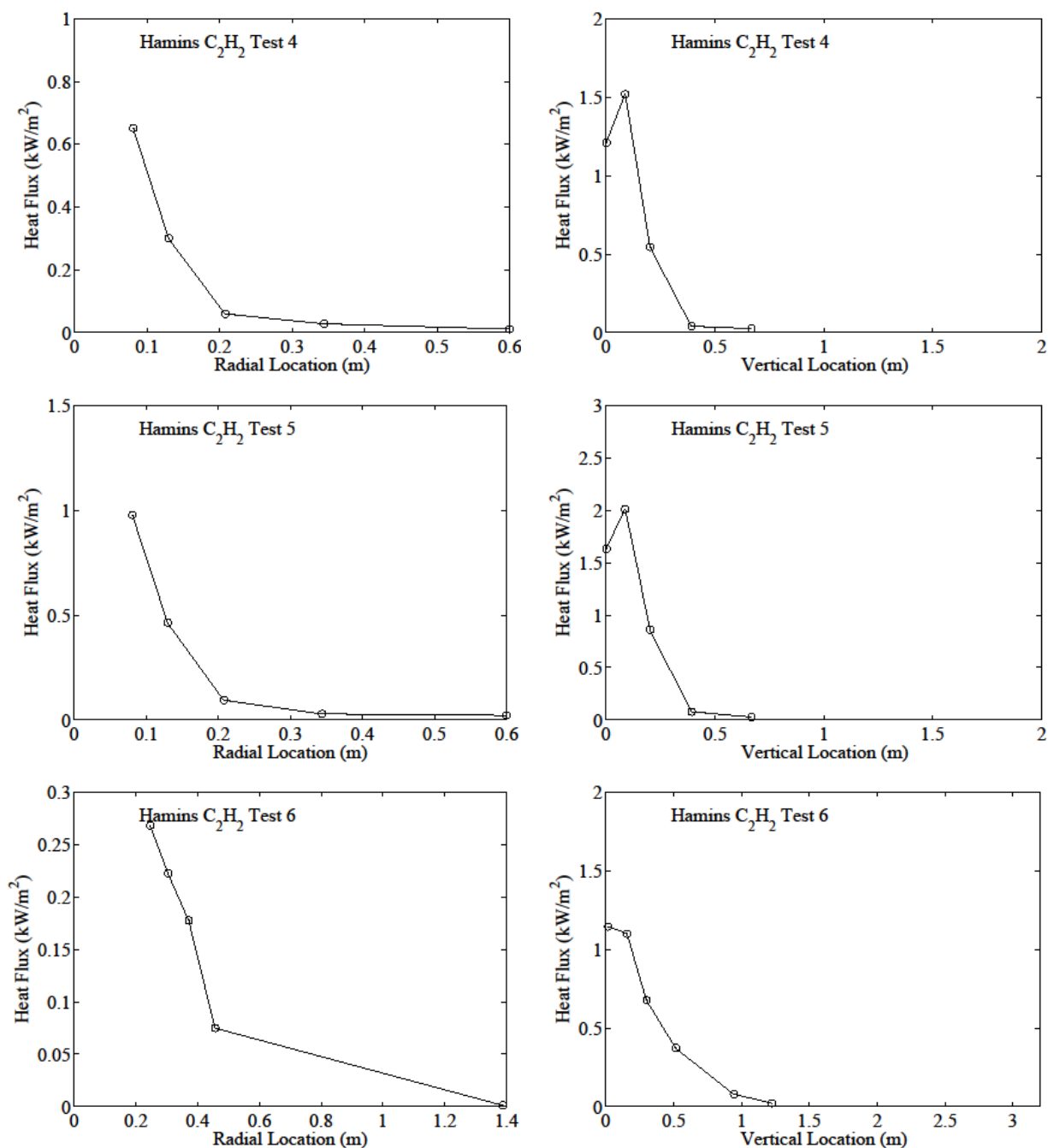


Figure A3.3 The measured local radiative heat flux distributions for 3 acetylene fire experiments (Tests A4 – A6) in the 0.1 m and 0.35 m burners, showing the flux downwards as a function of radial distance from the burner center (left) and the radial flux as a function of vertical location above the plane defined by the burner surface for locations (R_0) away from the burner axis (right-hand figures; see values of R_0 in the tables in Appendix 1). The lines connect the data points. The expanded measurement uncertainty was 16 %.

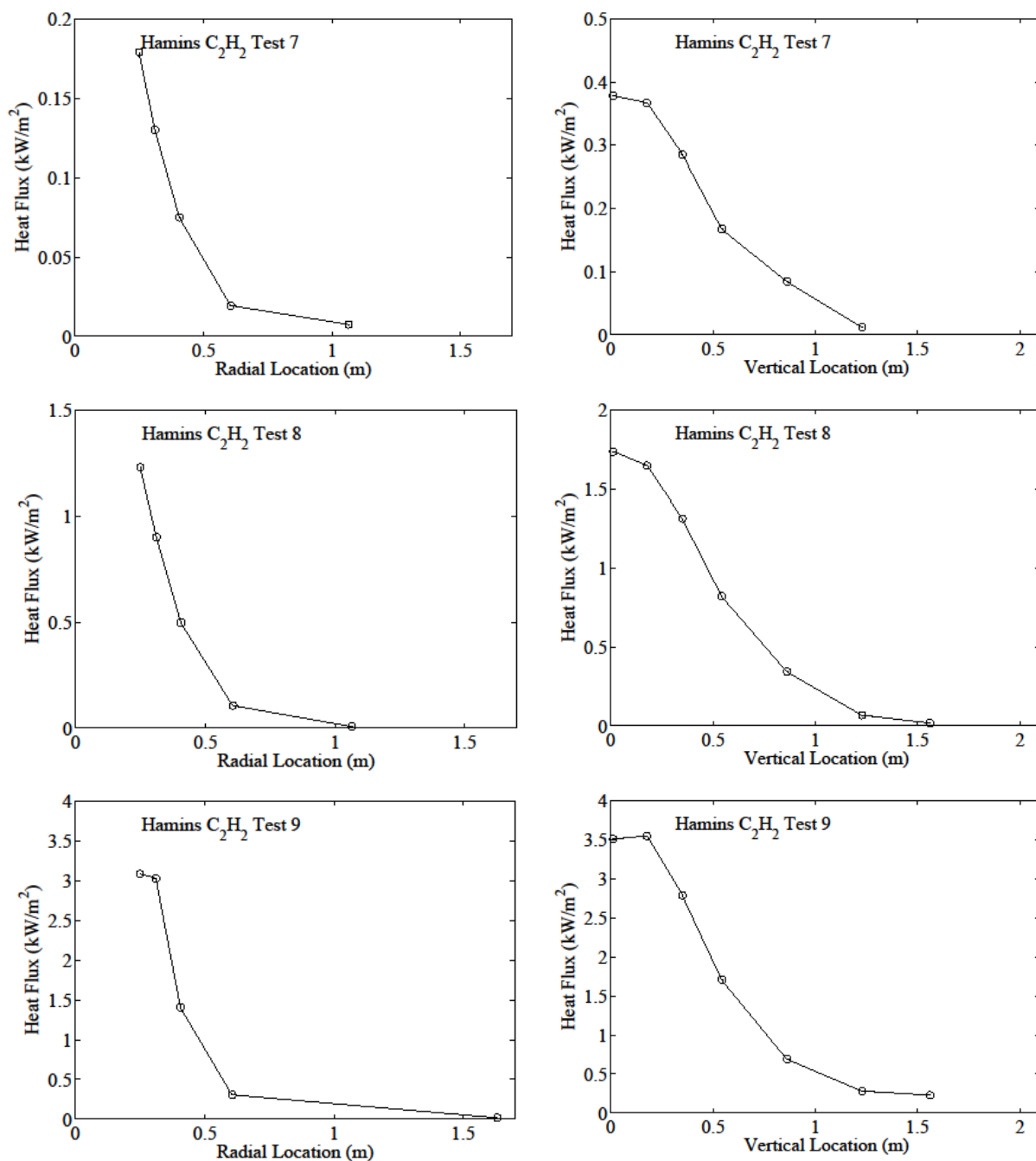


Figure A3.4 The measured local radiative heat flux distributions for 3 acetylene fire experiments (Tests A7 – A9) in the 0.35 m burner, showing the flux downwards as a function of radial distance from the burner center (left) and the radial flux as a function of vertical location above the plane defined by the burner surface for locations (R_o) away from the burner axis (right-hand figures; see values of R_o in the tables in Appendix 1). The lines connect the data points. The expanded measurement uncertainty was 16 %.

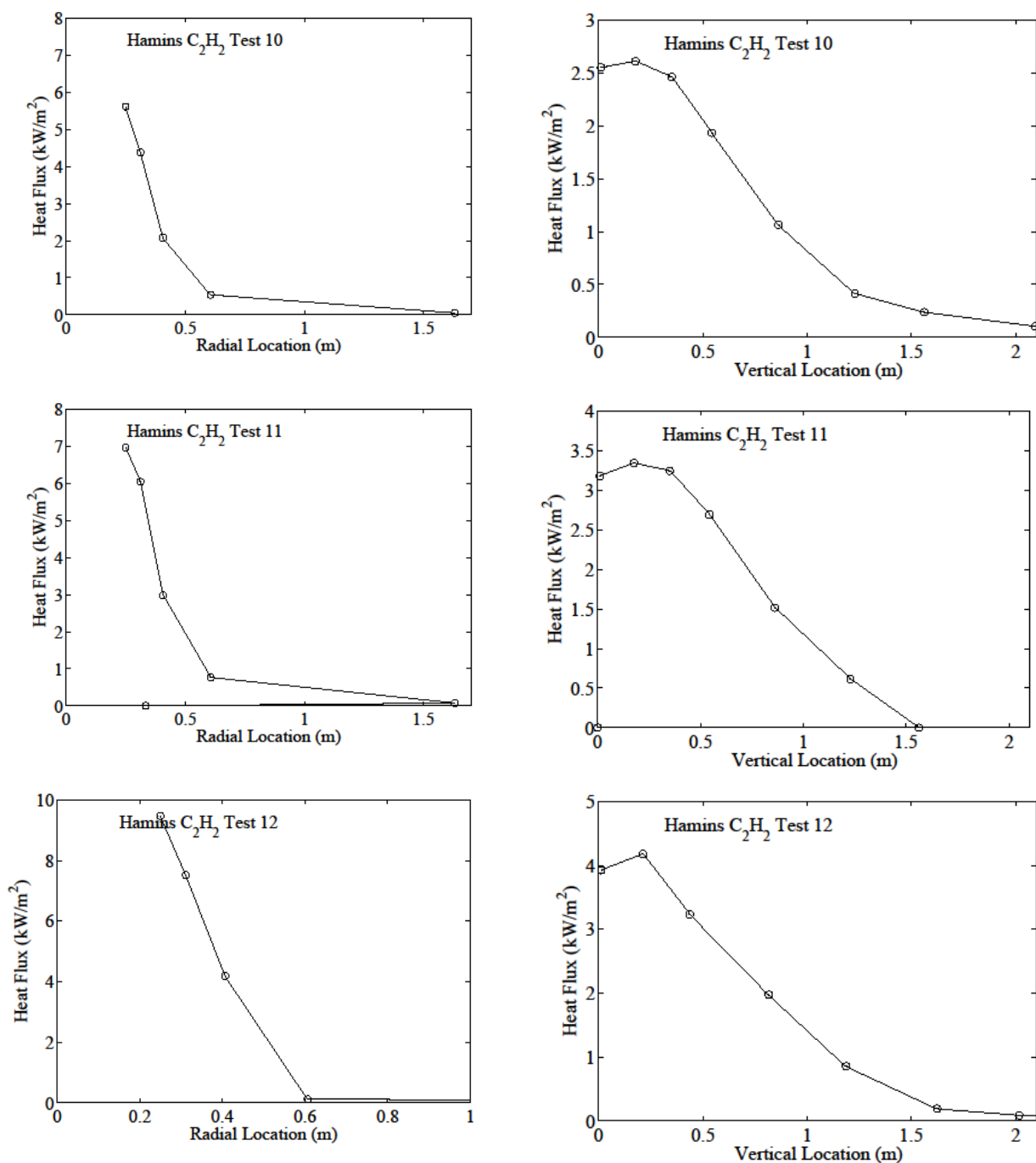


Figure A3.5 The measured local radiative heat flux distributions for 3 acetylene fire experiments (Tests A10 – A12) in the 0.35 m burner, showing the flux downwards as a function of radial distance from the burner center (left) and the radial flux as a function of vertical location above the plane defined by the burner surface for locations (R_o) away from the burner axis (right-hand figures; see values of R_o in the tables in Appendix 1). The lines connect the data points. The expanded measurement uncertainty was 16 %.

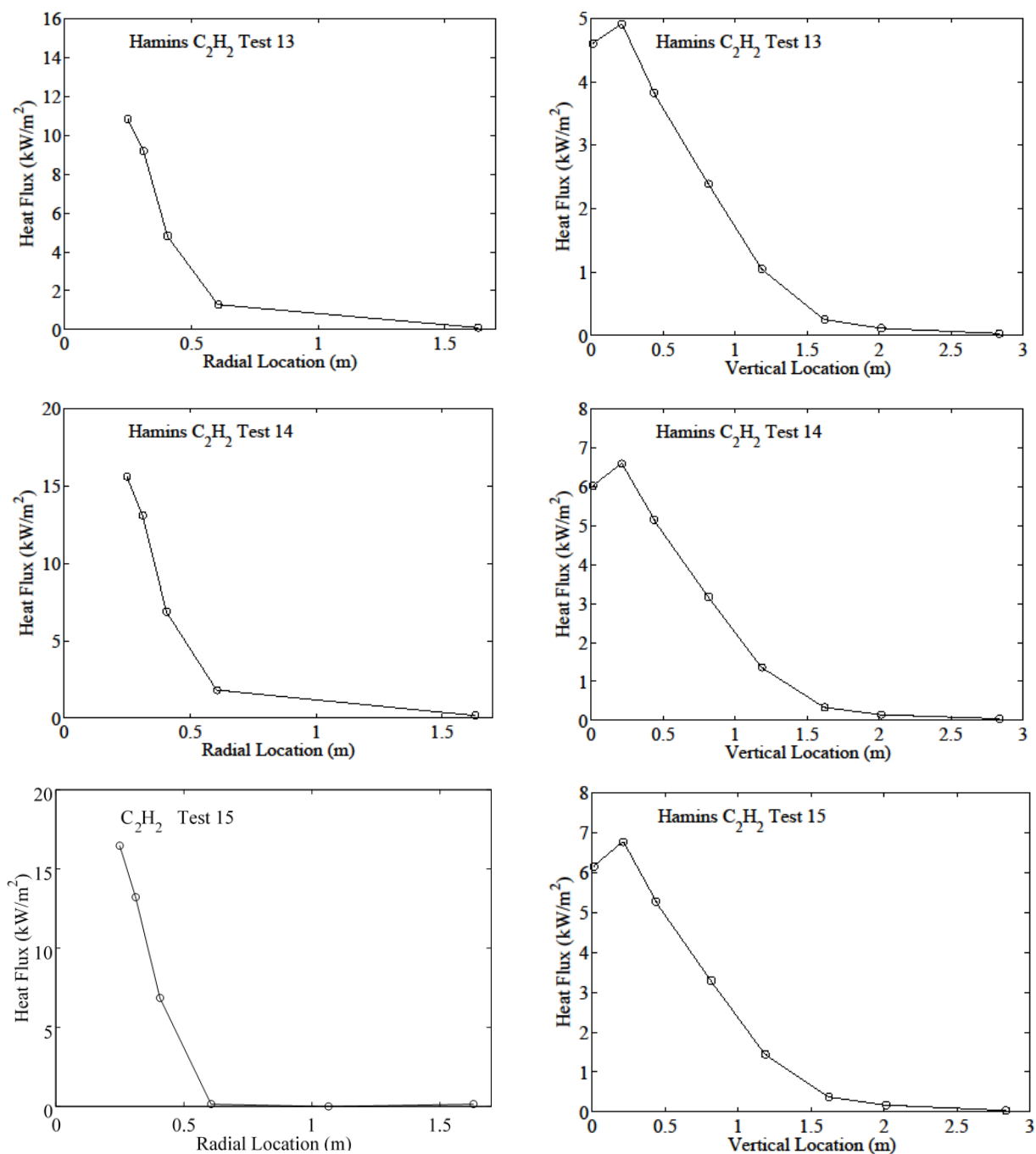


Figure A3.6 The measured local radiative heat flux distributions for 3 acetylene fire experiments (Tests A13 – A15) in the 0.35 m burner, showing the flux downwards as a function of radial distance from the burner center (left) and the radial flux as a function of vertical location above the plane defined by the burner surface for locations (R_0) away from the burner axis (right-hand figures; see values of R_0 in the tables in Appendix 1). The lines connect the data points. The expanded measurement uncertainty was 16 %.

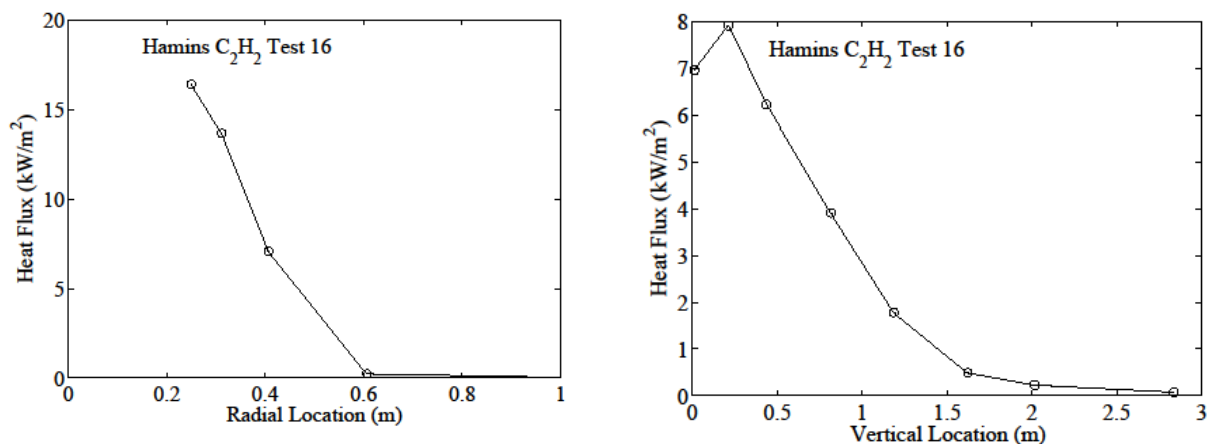


Figure A3.7 The measured local radiative heat flux distributions for an acetylene fire experiment (Test A16) in the 0.35 m burner, showing the flux downwards as a function of radial distance from the burner center (left) and the radial flux as a function of vertical location above the plane defined by the burner surface for locations (R_o) away from the burner axis (right-hand figures; see values of R_o in the tables in Appendix 1). The lines connect the data points. The expanded measurement uncertainty was 16 %.

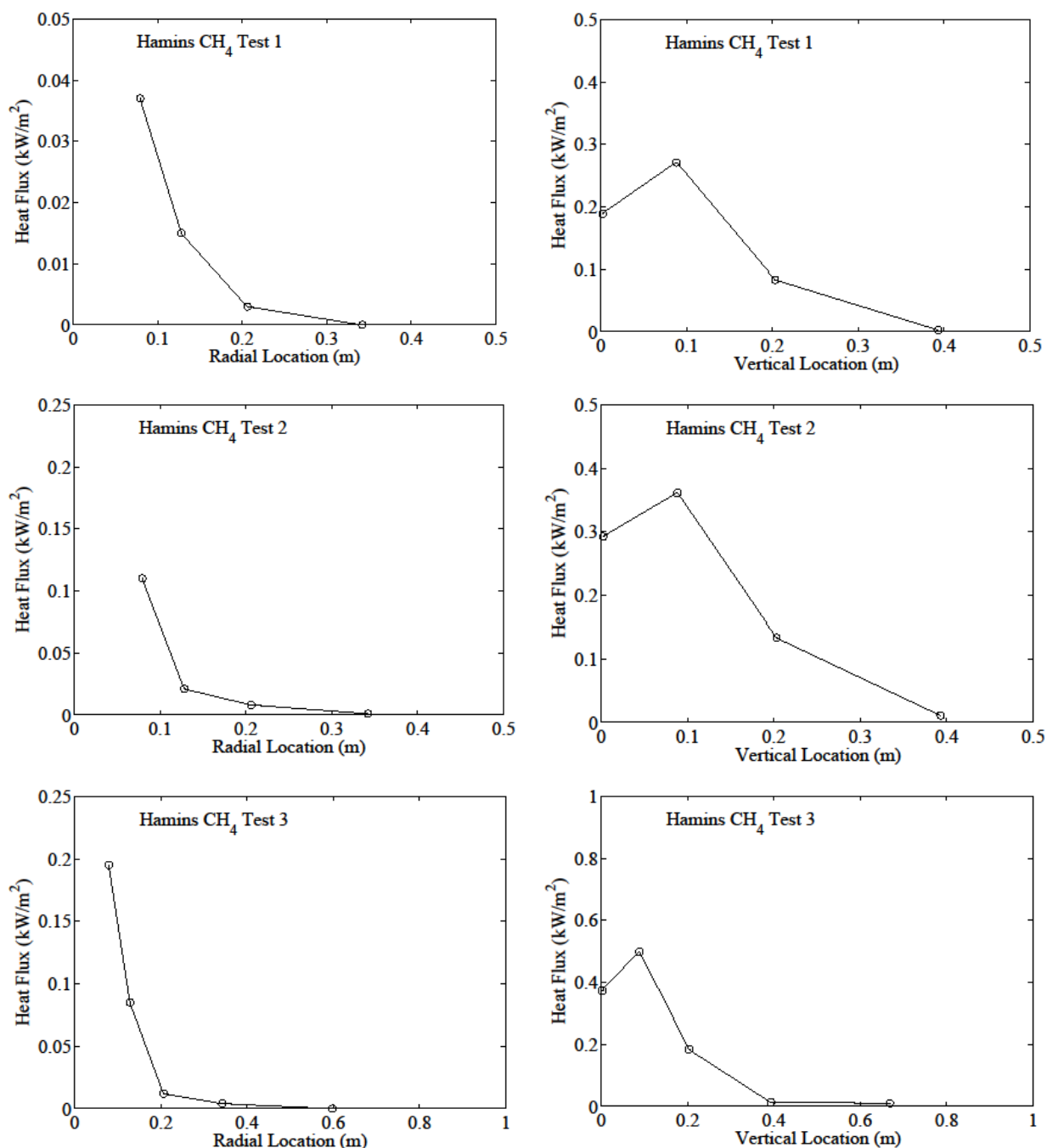


Figure A3.8 The measured local radiative heat flux distributions for 3 methane fire experiments (Tests M1 – M3) in the 0.1 m burner, showing the flux downwards as a function of radial distance from the burner center (left) and the radial flux as a function of vertical location above the plane defined by the burner surface for locations (R_o) away from the burner axis (right-hand figures; see values of R_o in the tables in Appendix 1). The lines connect the data points. The expanded measurement uncertainty was 16 %.

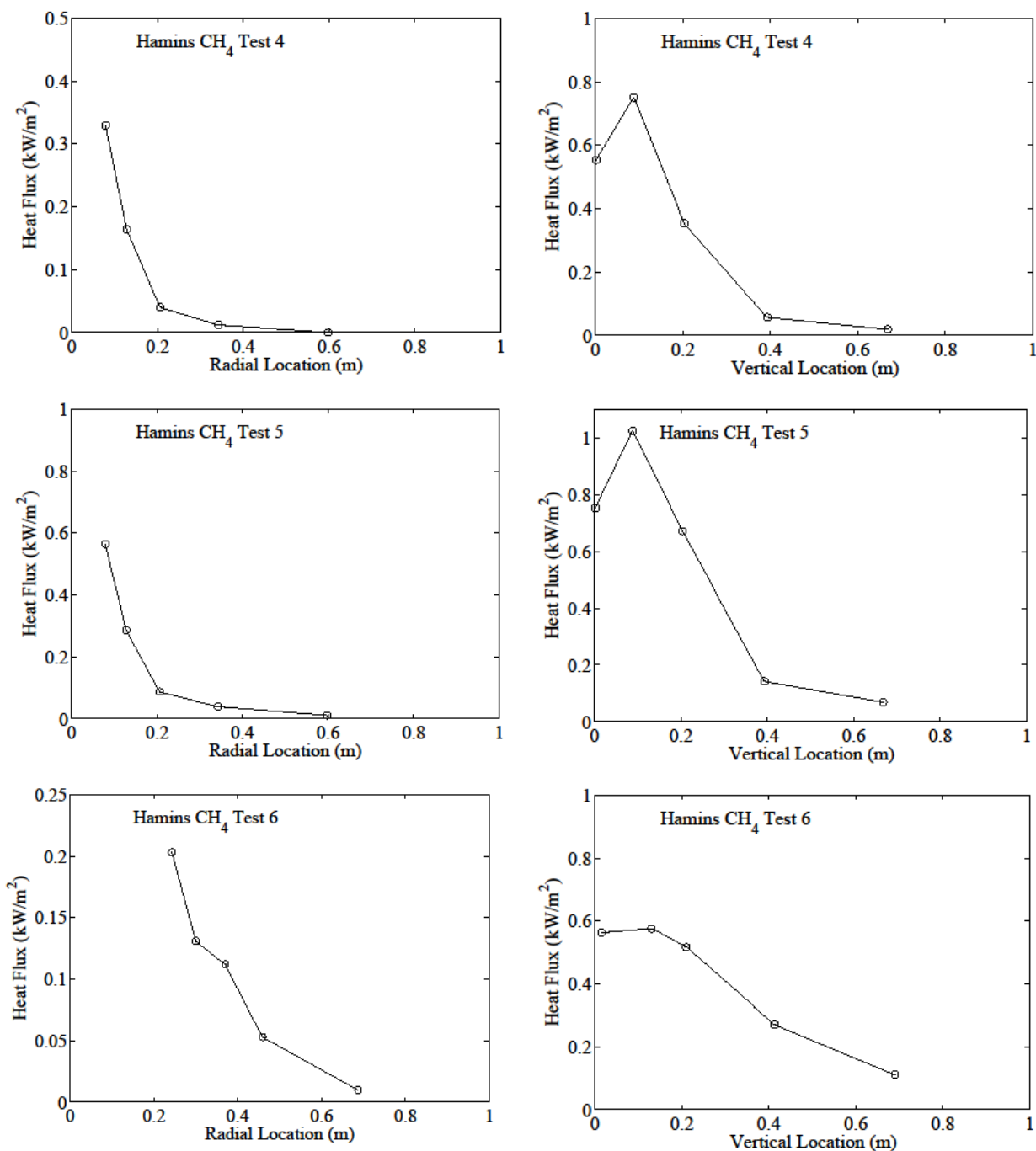


Figure A3.9 The measured local radiative heat flux distributions for 3 methane and natural gas fire experiments (Tests M4 – M6) in the 0.1 m and 0.35 m burners, showing the flux downwards as a function of radial distance from the burner center (left) and the radial flux as a function of vertical location above the plane defined by the burner surface for locations (R_0) away from the burner axis (right-hand figures; see values of R_0 in the tables in Appendix 1). The lines connect the data points. The expanded measurement uncertainty was 16 %.

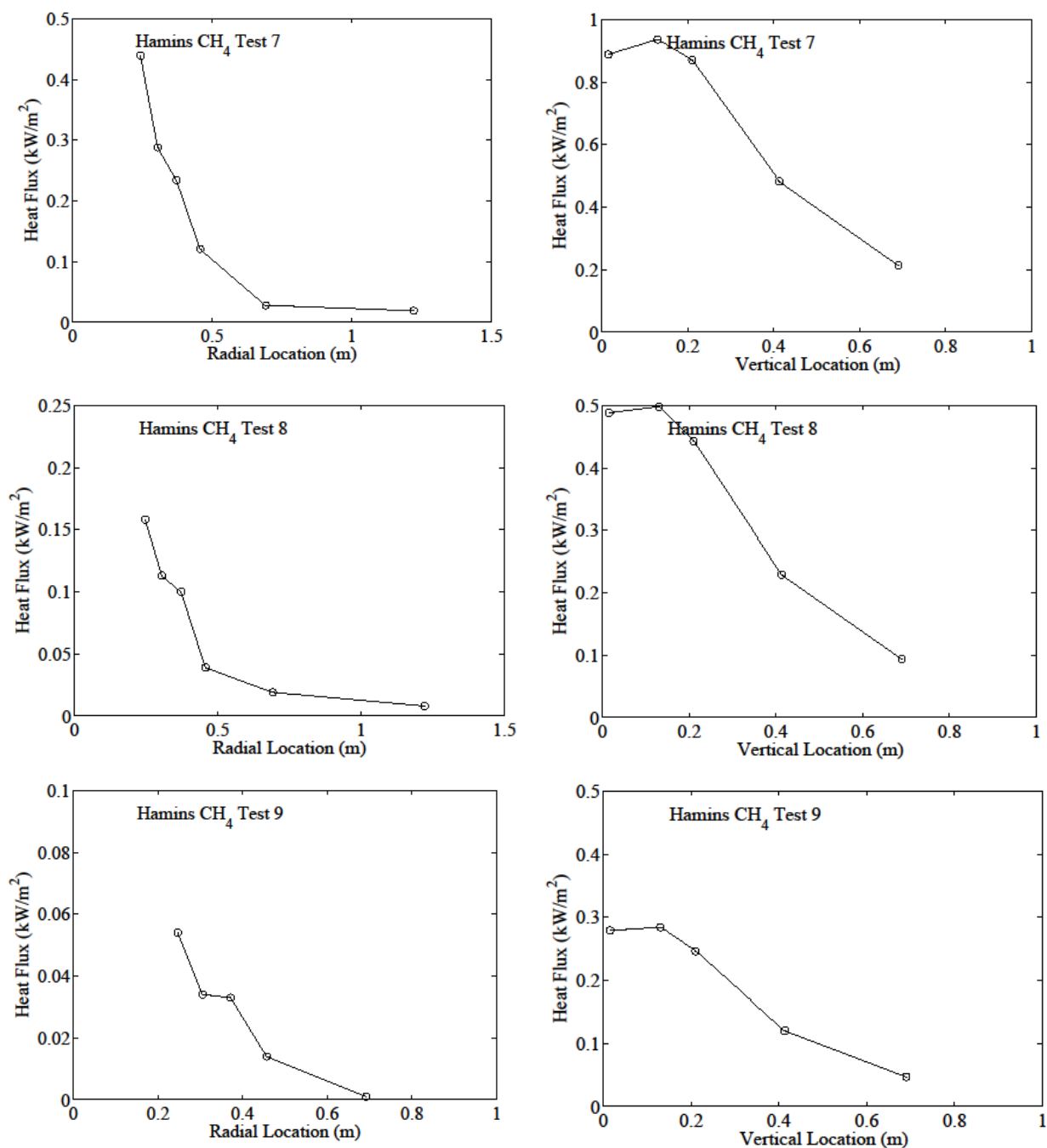


Figure A3.10 The measured local radiative heat flux distributions for 3 natural gas fire experiments (Tests M7 – M9) in the 0.35 m burner, showing the flux downwards as a function of radial distance from the burner center (left) and the radial flux as a function of vertical location above the plane defined by the burner surface for locations (R_o) away from the burner axis (right-hand figures; see values of R_o in the tables in Appendix 1). The lines connect the data points. The expanded measurement uncertainty was 16 %.

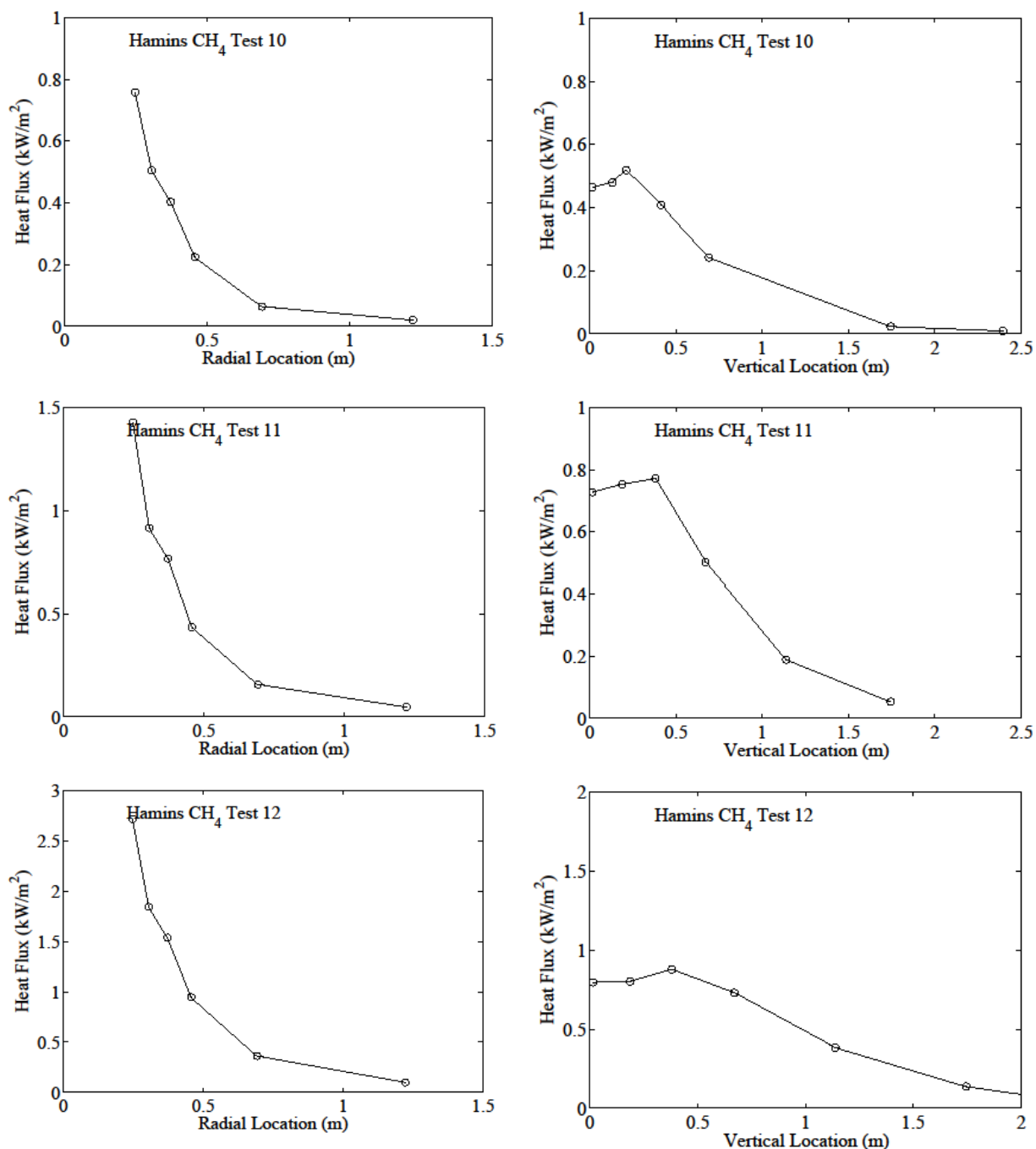


Figure A3.11 The measured local radiative heat flux distributions for 3 methane and natural gas fire experiments (Tests M10–M12) in the 0.35 m burner, showing the flux downwards as a function of radial distance from the burner center (left) and the radial flux as a function of vertical location above the plane defined by the burner surface for locations (R_o) away from the burner axis (right-hand figures; see values of R_o in the tables in Appendix 1). The lines connect the data points. The expanded measurement uncertainty was 16 %.

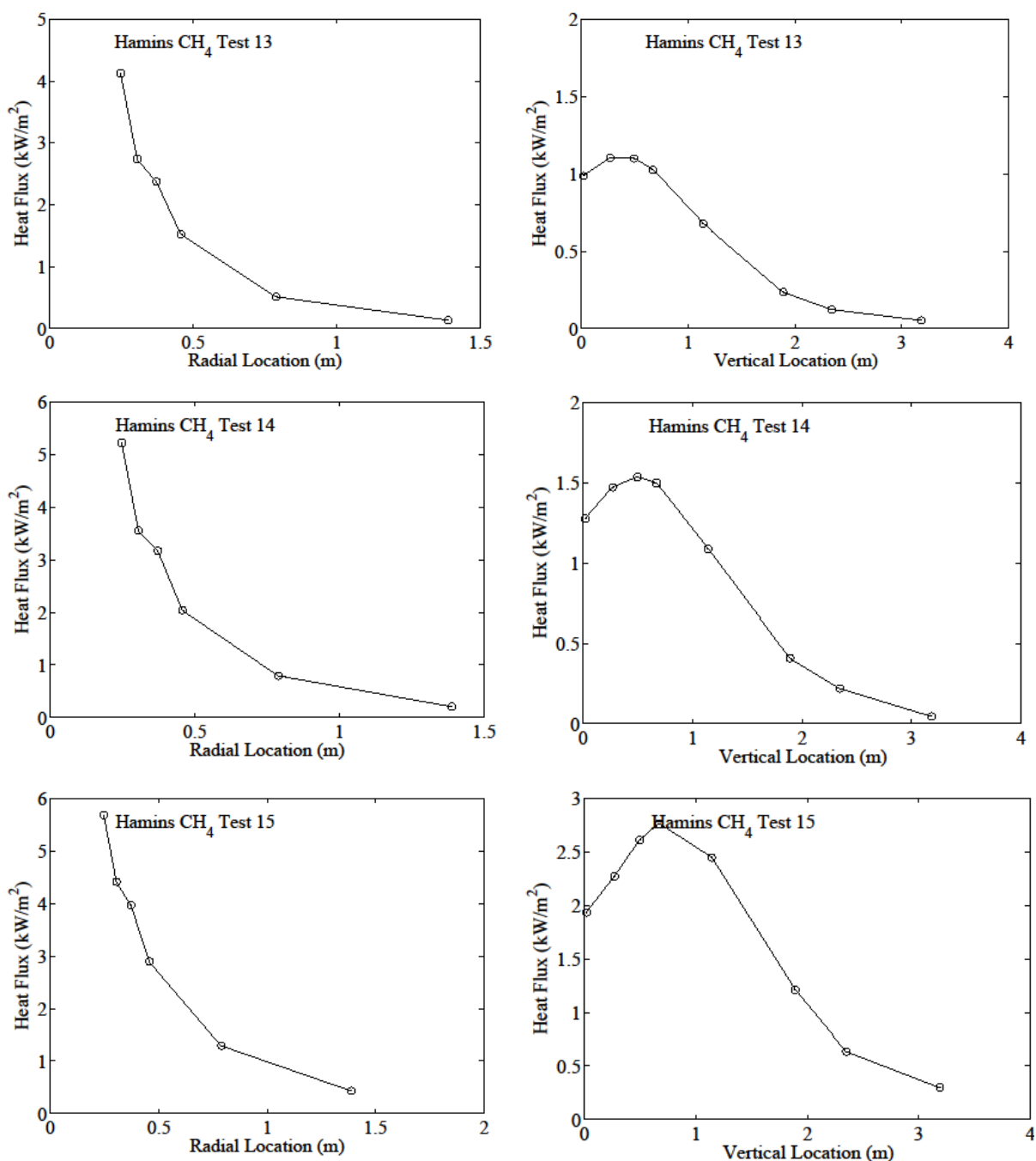


Figure A3.12 The measured local radiative heat flux distributions for 3 methane and natural gas fire experiments (Tests M13–M15) in the 0.35 m burner, showing the flux downwards as a function of radial distance from the burner center (left) and the radial flux as a function of vertical location above the plane defined by the burner surface for locations (R_o) away from the burner axis (right-hand figures; see values of R_o in the tables in Appendix 1). The lines connect the data points. The expanded measurement uncertainty was 16 %.

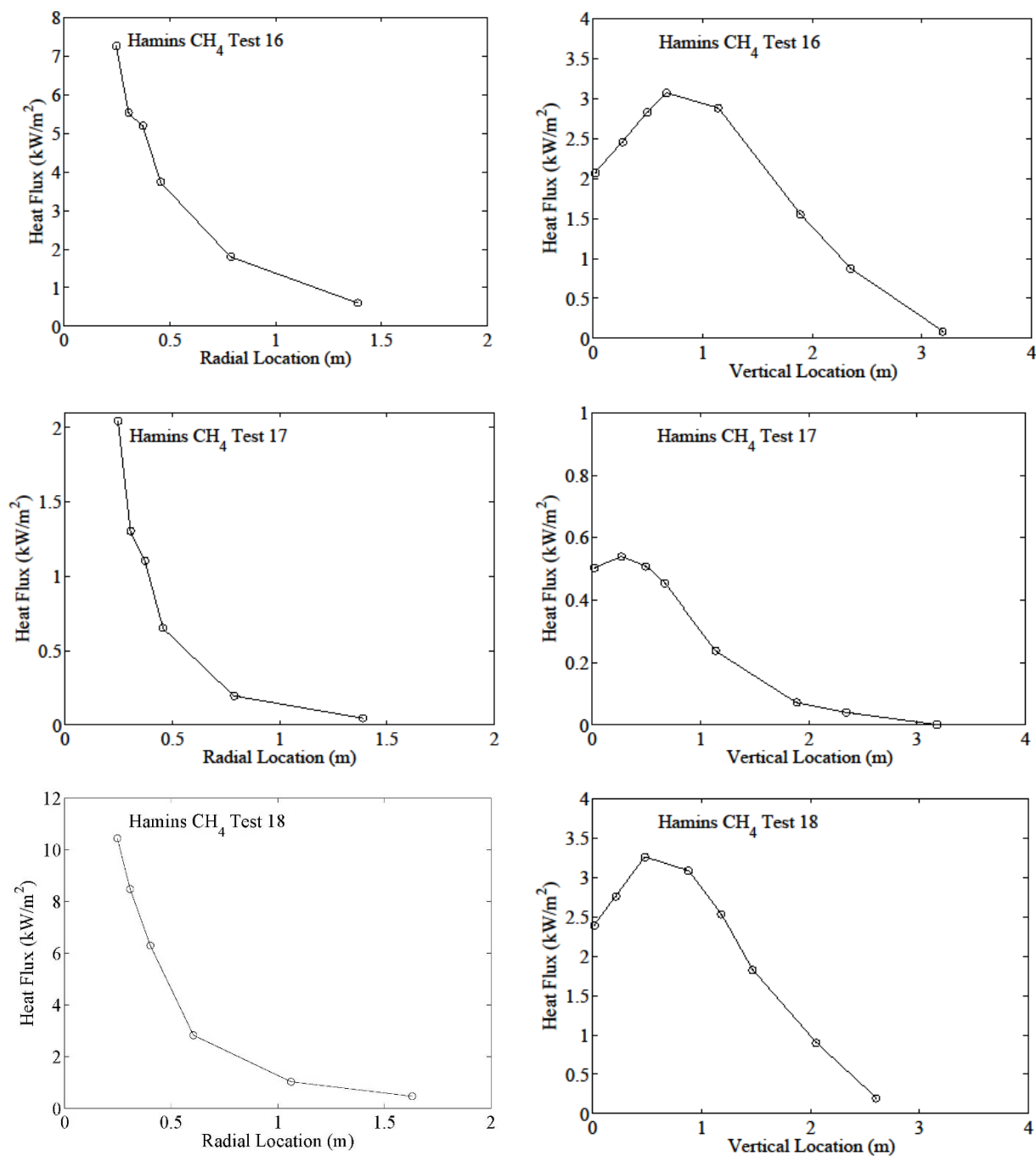


Figure A3.13 The measured local radiative heat flux distributions for 3 methane fire experiments (Tests M16–M18) in the 0.35 m burner, showing the flux downwards as a function of radial distance from the burner center (left) and the radial flux as a function of vertical location above the plane defined by the burner surface for locations (R_o) away from the burner axis (right-hand figures; see values of R_o in the tables in Appendix 1). The lines connect the data points. The expanded measurement uncertainty was 16 %.

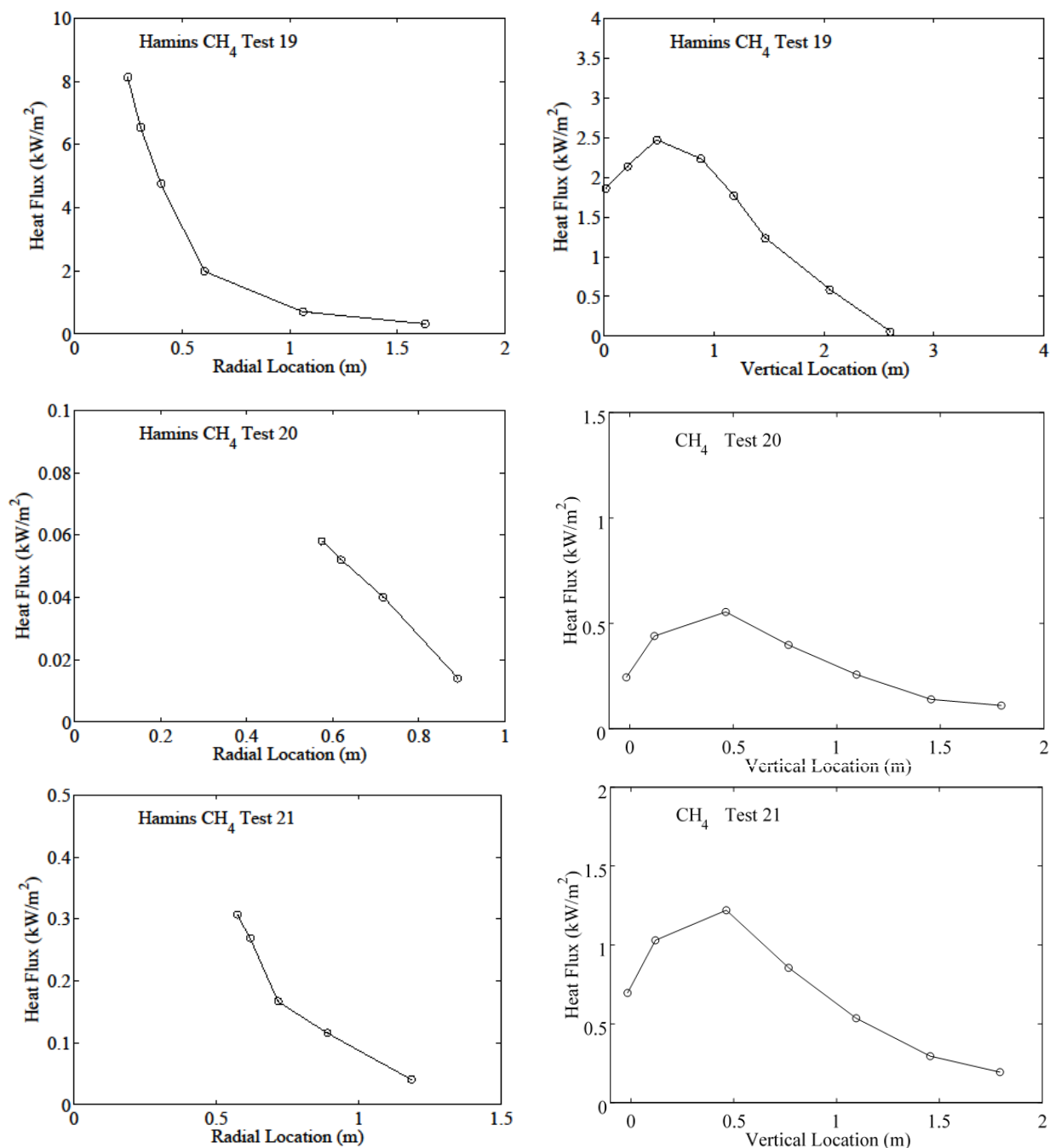


Figure A3.14 The measured local radiative heat flux distributions for methane and natural gas fire experiments (Tests M19–M21) in the 0.35 m and 1.00 m burners, showing the flux downwards as a function of radial distance from the burner center (left) and the radial flux as a function of vertical location above the plane defined by the burner surface for locations (R_0) away from the burner axis (right-hand figures; see values of R_0 in the tables in Appendix 1). The lines connect the data points. The expanded measurement uncertainty was 16 %.

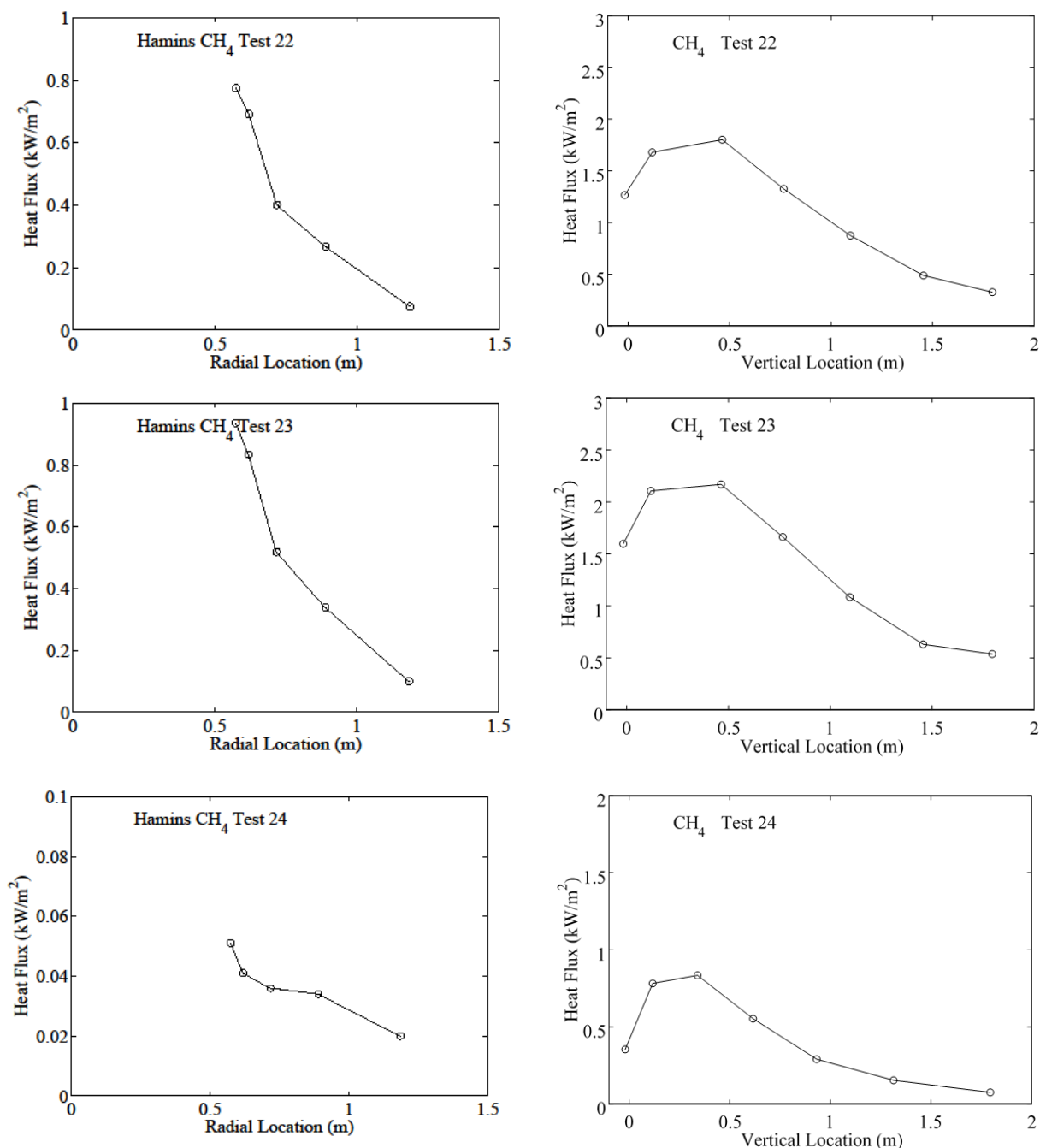


Figure A3.15 The measured local radiative heat flux distributions for 3 natural gas fire experiments (Tests M22–M24) in the 1.00 m burner, showing the flux downwards as a function of radial distance from the burner center (left) and the radial flux as a function of vertical location above the plane defined by the burner surface for locations (R_0) away from the burner axis (right-hand figures; see values of R_0 in the tables in Appendix 1). The lines connect the data points. The expanded measurement uncertainty was 16 %.

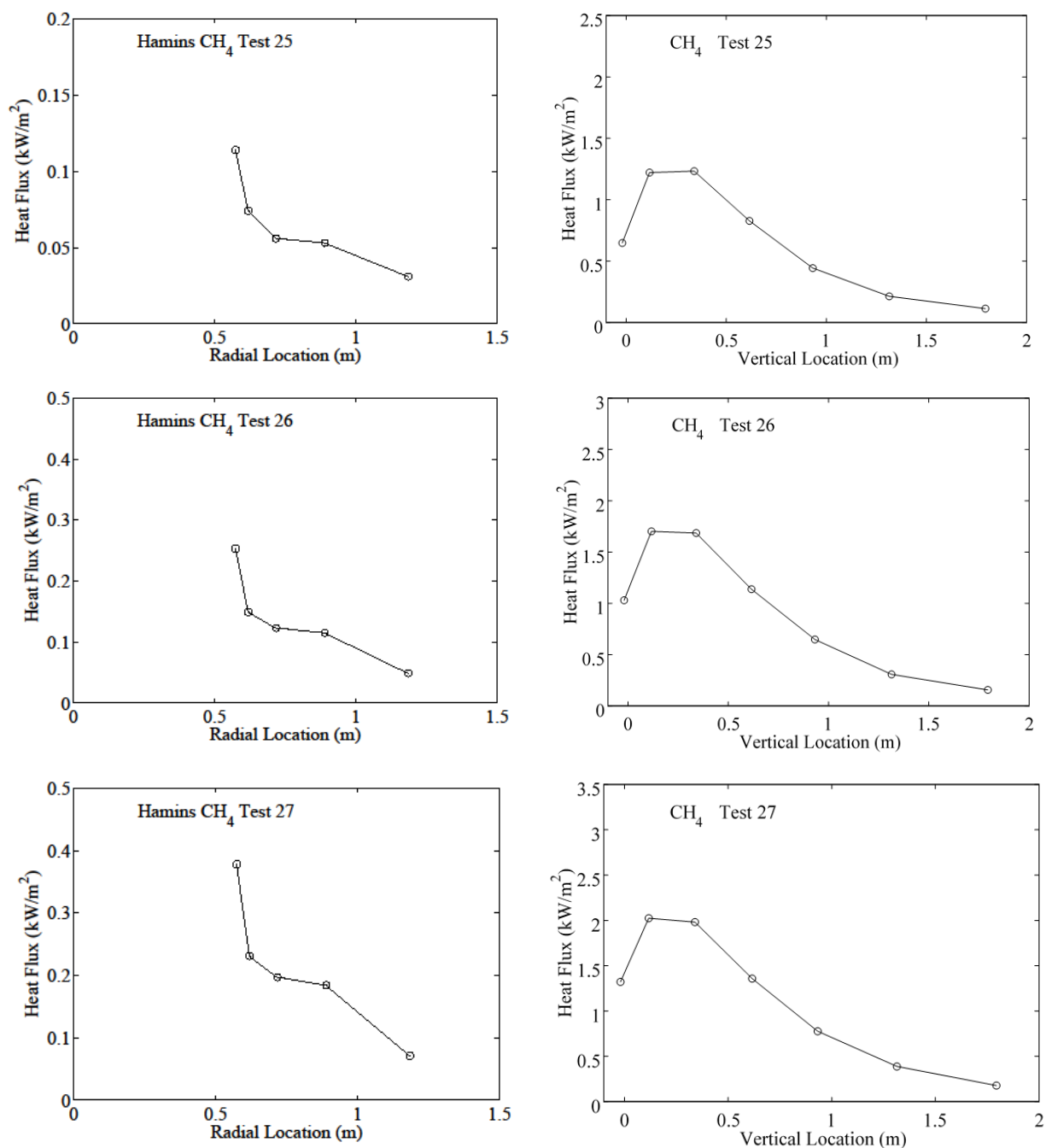


Figure A3.16 The measured local radiative heat flux distributions for 3 natural gas fire experiments (Tests M25–M27) in the 1.00 m burner, showing the flux downwards as a function of radial distance from the burner center (left) and the radial flux as a function of vertical location above the plane defined by the burner surface for locations (R_0) away from the burner axis (right-hand figures; see values of R_0 in the tables in Appendix 1). The lines connect the data points. The expanded measurement uncertainty was 16 %.

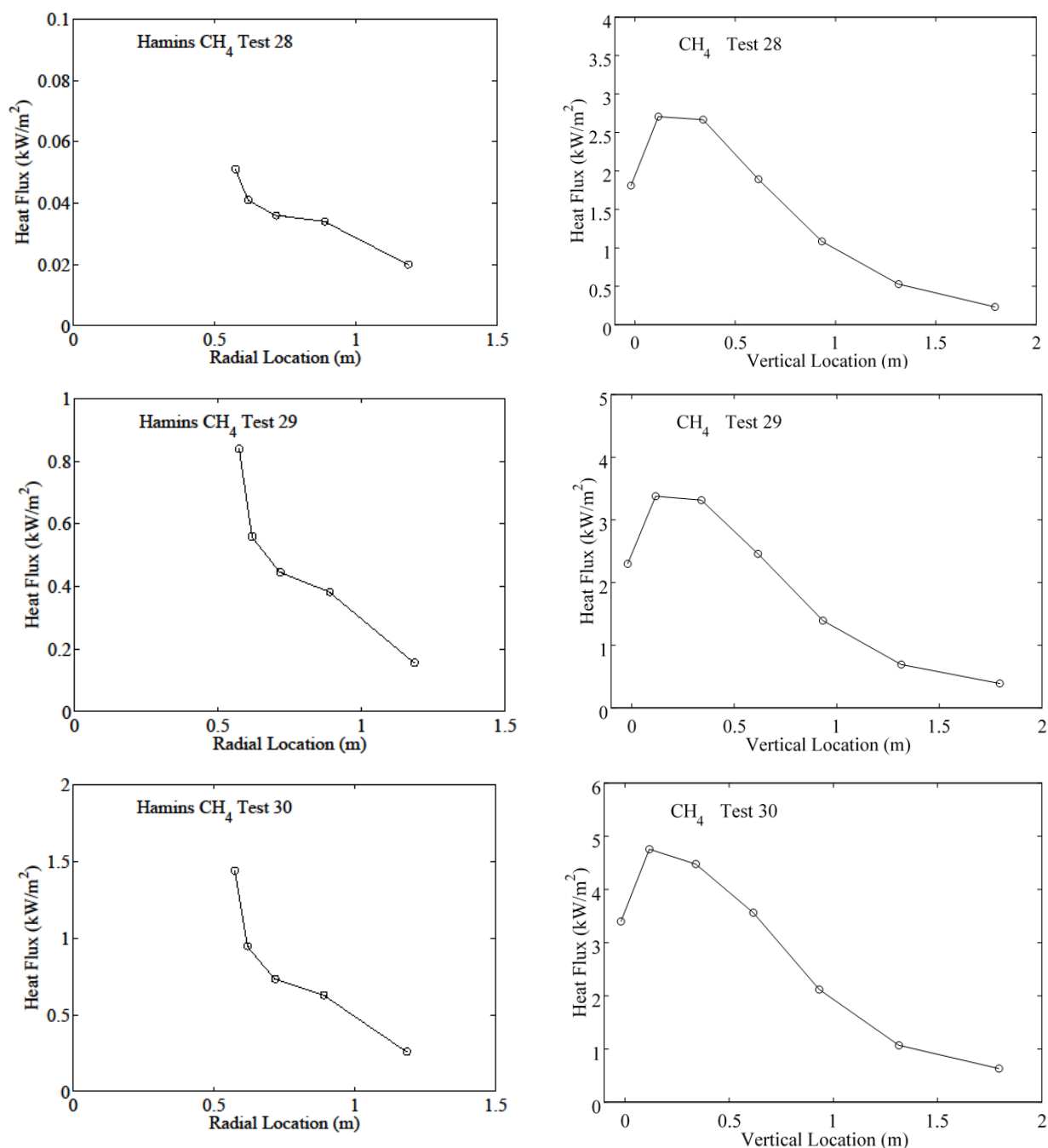


Figure A3.17 The measured local radiative heat flux distributions for 3 natural gas fire experiments (Tests M28–M30) in the 1.00 m burner, showing the flux downwards as a function of radial distance from the burner center (left) and the radial flux as a function of vertical location above the plane defined by the burner surface for locations (R_0) away from the burner axis (right-hand figures; see values of R_0 in the tables in Appendix 1). The lines connect the data points. The expanded measurement uncertainty was 16 %.

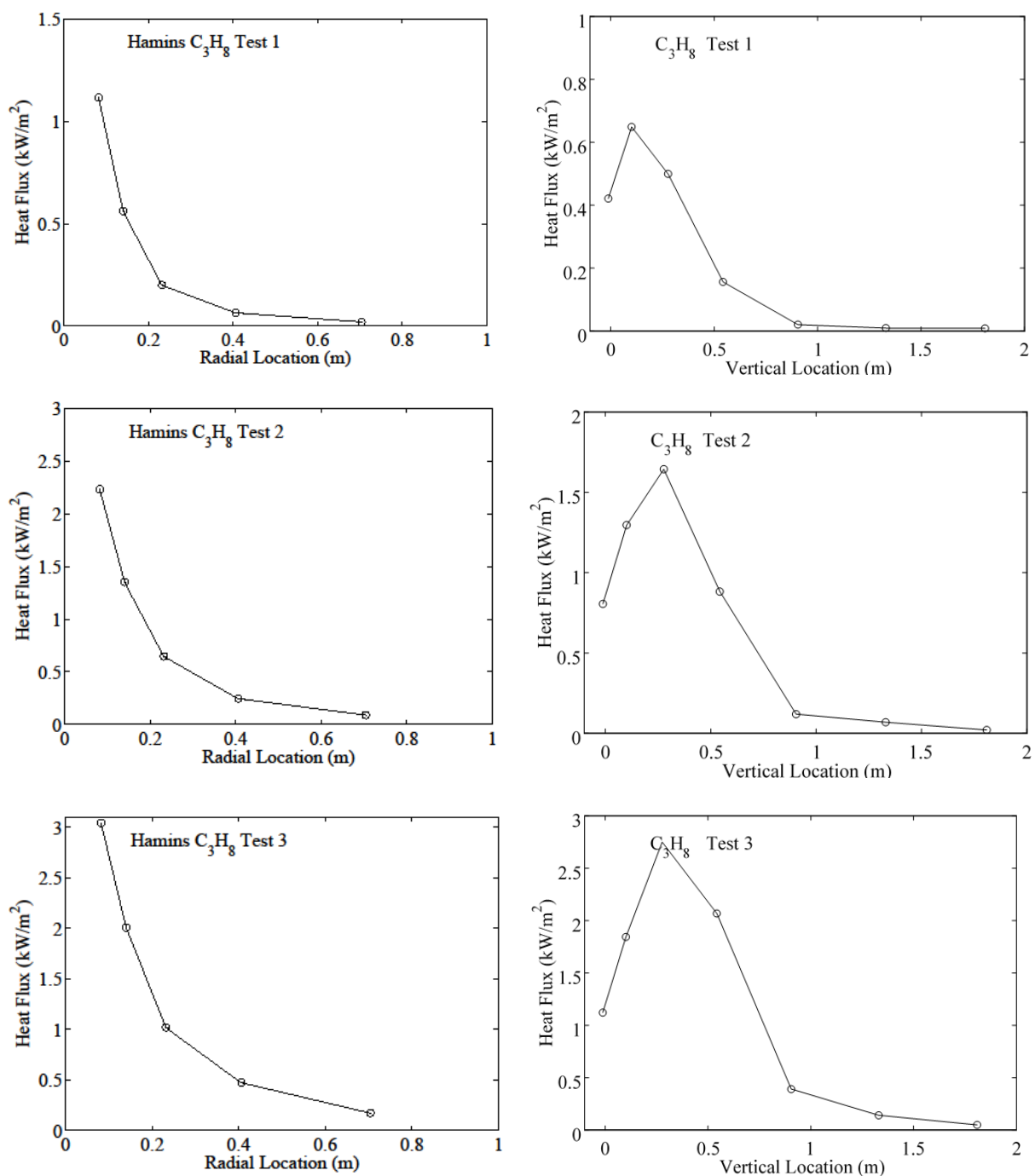


Figure A3.18 The measured local radiative heat flux distributions for 3 propane fire experiments (Tests P1–P3) in the 0.10 m burner, showing the flux downwards as a function of radial distance from the burner center (left) and the radial flux as a function of vertical location above the plane defined by the burner surface for locations (R_o) away from the burner axis (right-hand figures; see values of R_o in the tables in Appendix 1). The lines connect the data points. The expanded measurement uncertainty was 16 %.

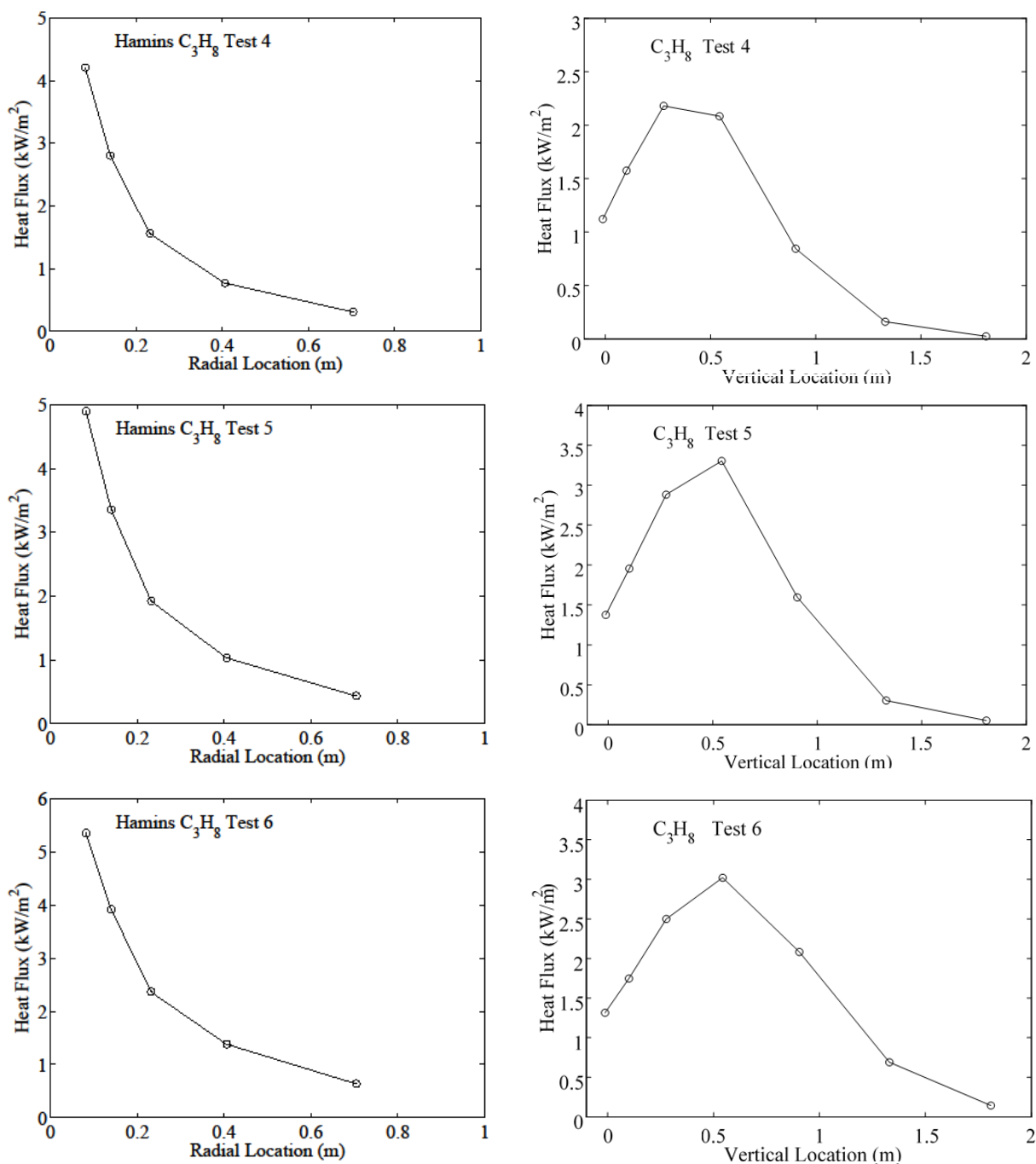


Figure A3.19 The measured local radiative heat flux distributions for 3 propane fire experiments (Tests P4–P6) in the 0.10 m burner, showing the flux downwards as a function of radial distance from the burner center (left) and the radial flux as a function of vertical location above the plane defined by the burner surface for locations (R_0) away from the burner axis (right-hand figures; see values of R_0 in the tables in Appendix 1). The lines connect the data points. The expanded measurement uncertainty was 16 %.

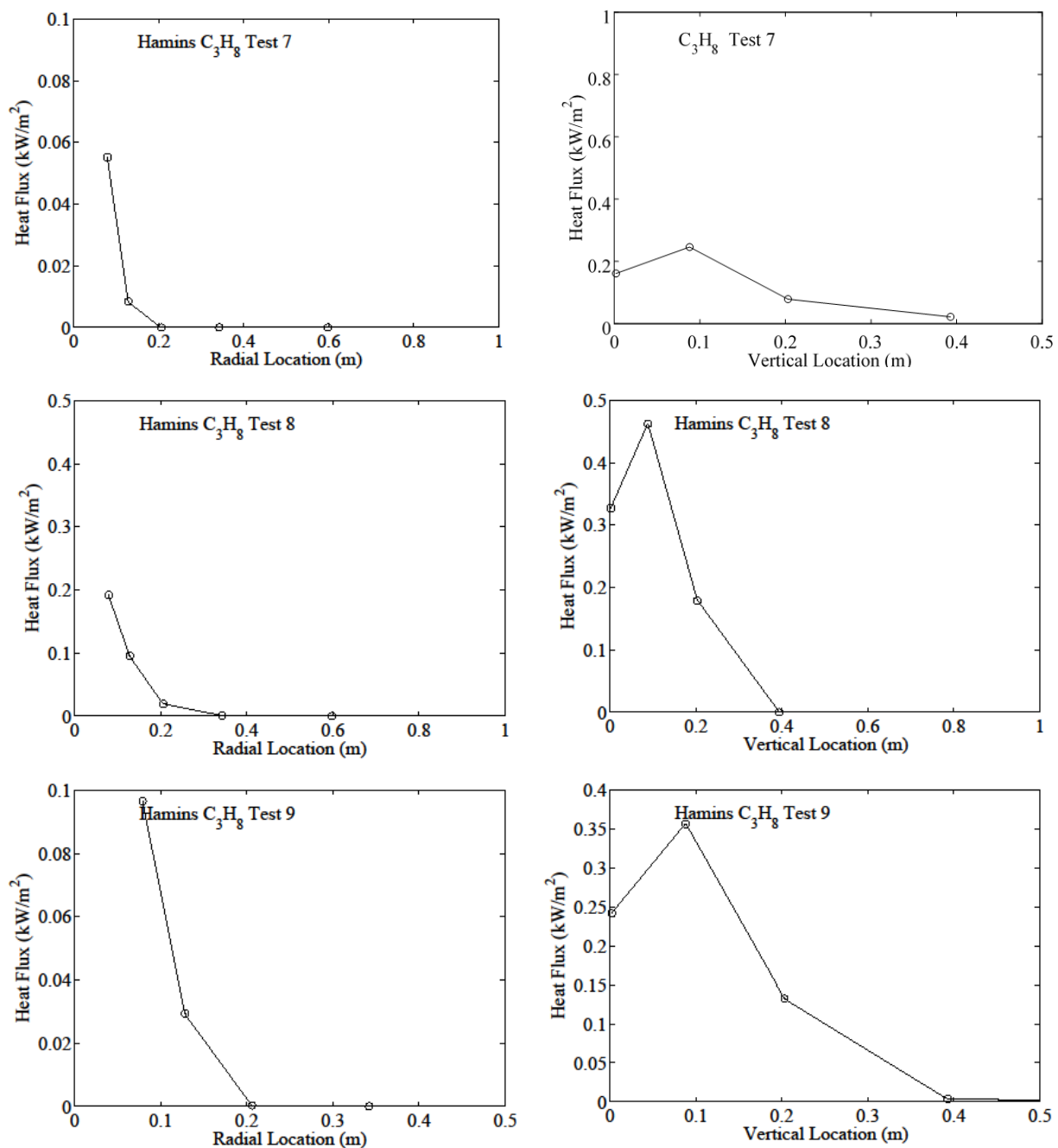


Figure A3.20 The measured local radiative heat flux distributions for 3 propane fire experiments (Tests P7–P9) in the 0.10 m burner, showing the flux downwards as a function of radial distance from the burner center (left) and the radial flux as a function of vertical location above the plane defined by the burner surface for locations (R_o) away from the burner axis (right-hand figures; see values of R_o in the tables in Appendix 1). The lines connect the data points. The expanded measurement uncertainty was 16 %.

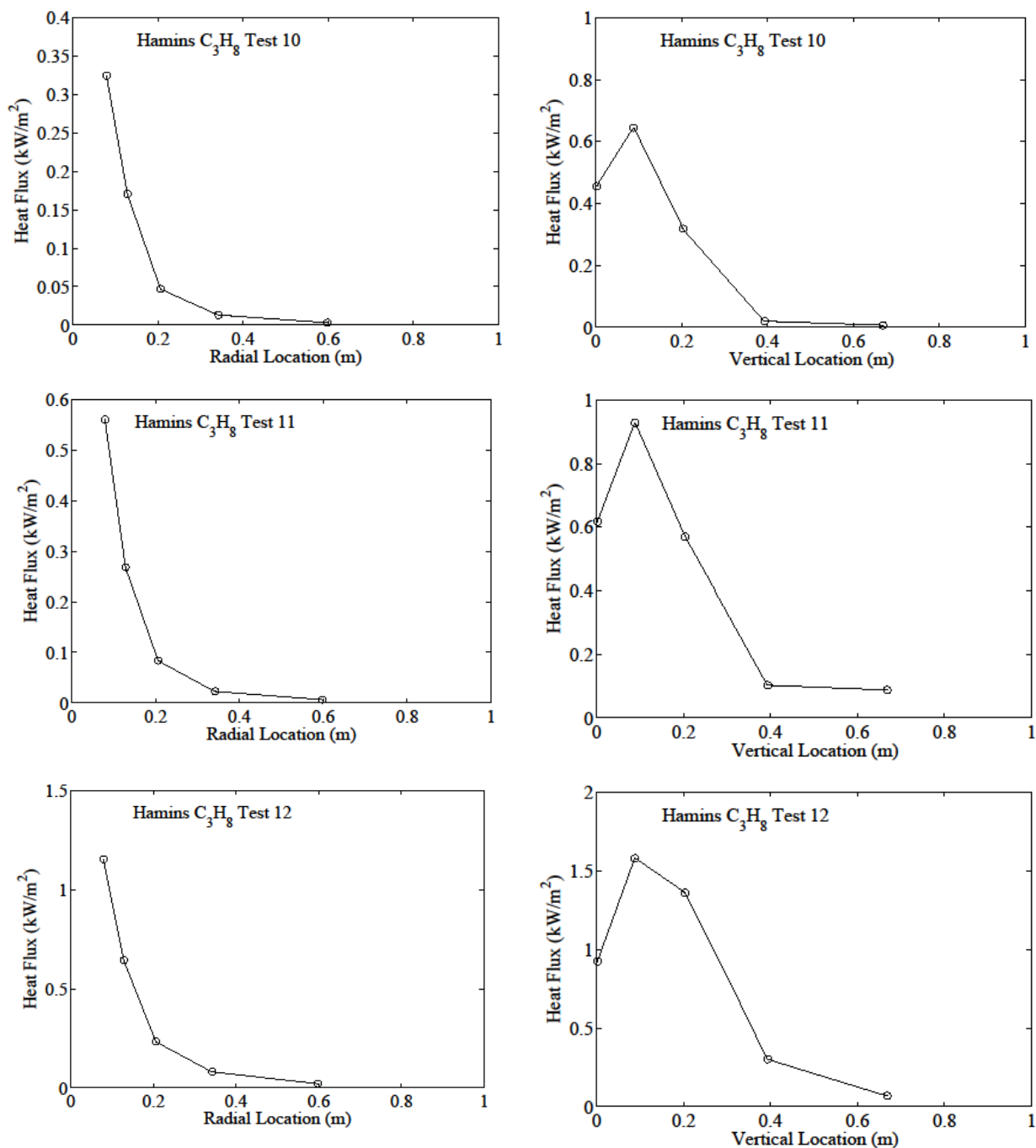


Figure A3.21 The measured local radiative heat flux distributions for 3 propane fire experiments (Tests P10–P12) in the 0.10 m burner, showing the flux downwards as a function of radial distance from the burner center (left) and the radial flux as a function of vertical location above the plane defined by the burner surface for locations (R_o) away from the burner axis (right-hand figures; see values of R_o in the tables in Appendix 1). The lines connect the data points. The expanded measurement uncertainty was 16 %.

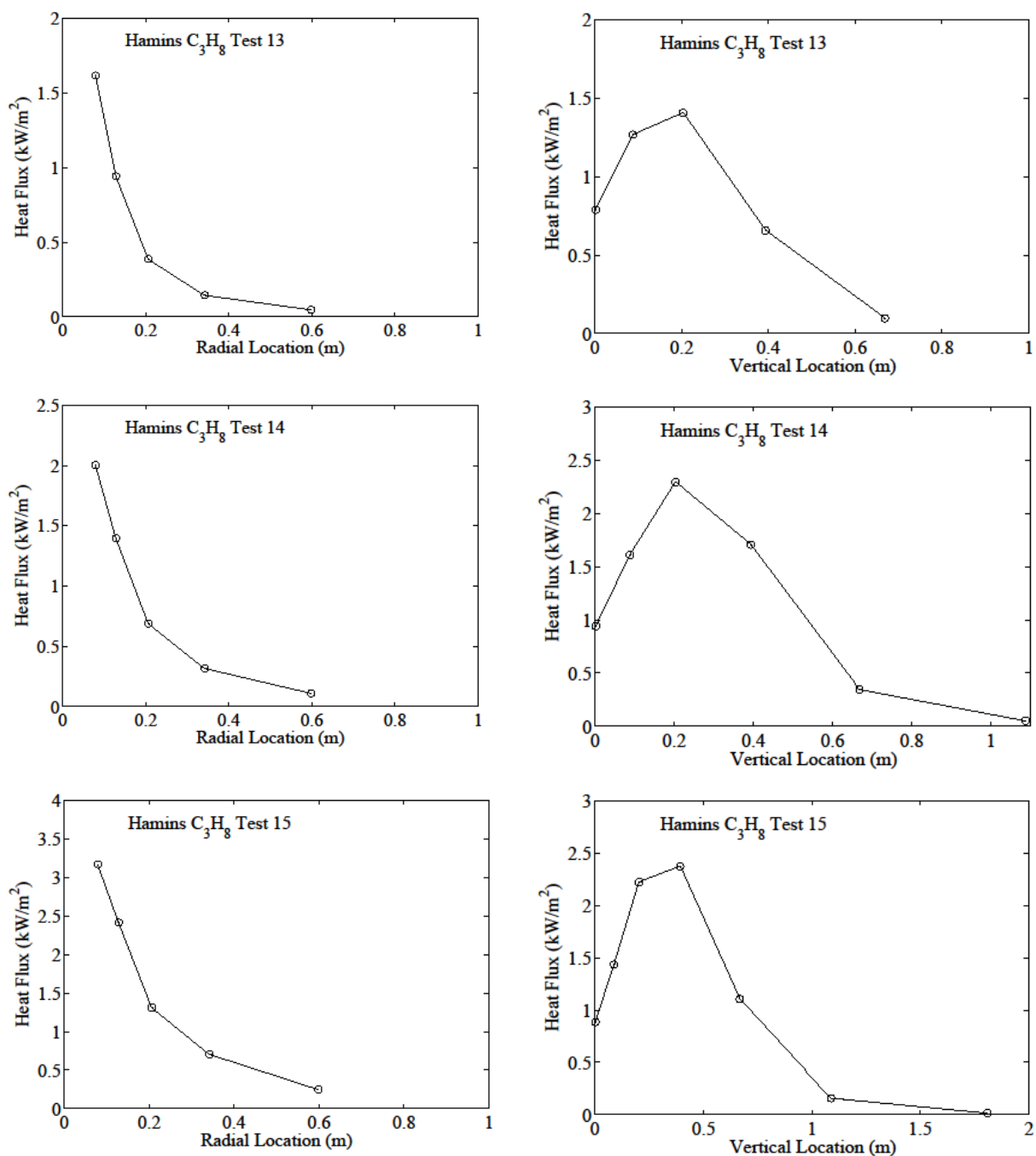


Figure A3.22 The measured local radiative heat flux distributions for 3 propane fire experiments (Tests P13–P15) in the 0.10 m burner, showing the flux downwards as a function of radial distance from the burner center (left) and the radial flux as a function of vertical location above the plane defined by the burner surface for locations (R_o) away from the burner axis (right-hand figures; see values of R_o in the tables in Appendix 1). The lines connect the data points. The expanded measurement uncertainty was 16 %.

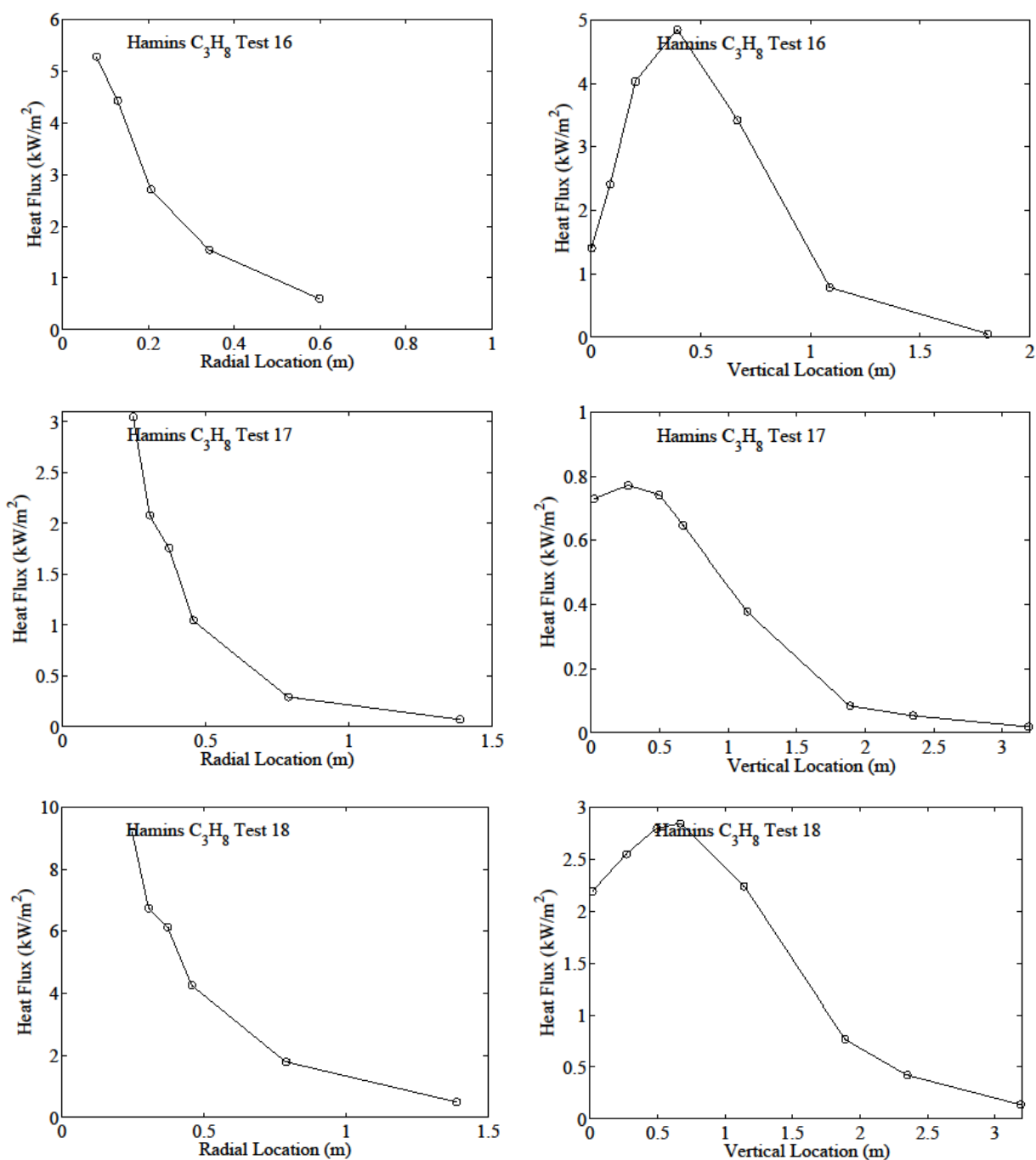


Figure A3.23 The measured local radiative heat flux distributions for 3 propane fire experiments (Tests P16–P18) in the 0.10 m and 0.35 m burners, showing the flux downwards as a function of radial distance from the burner center (left) and the radial flux as a function of vertical location above the plane defined by the burner surface for locations (R_o) away from the burner axis (right-hand figures; see values of R_o in the tables in Appendix 1). The lines connect the data points. The expanded measurement uncertainty was 16 %.

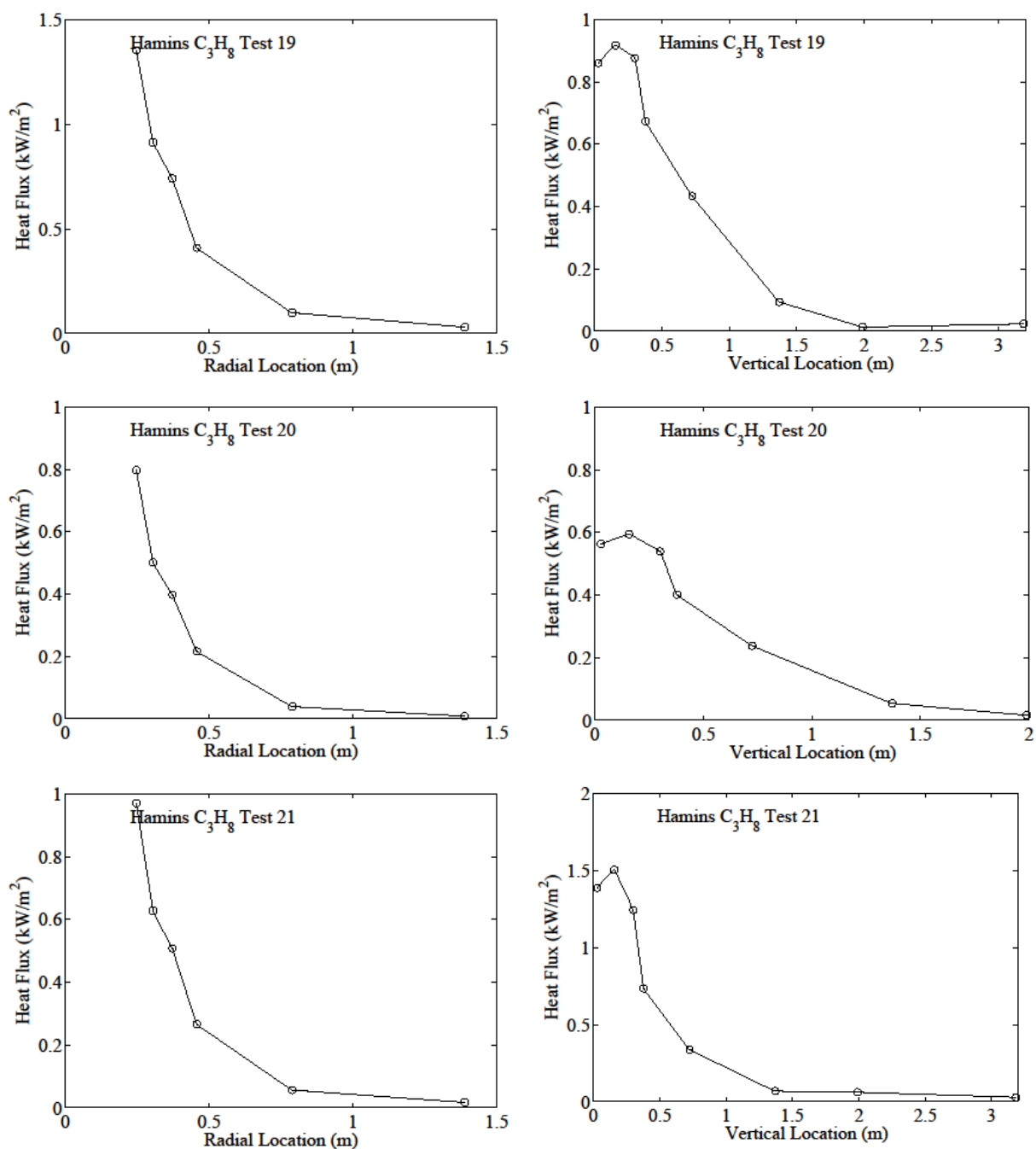


Figure A3.24 The measured local radiative heat flux distributions for 3 propane fire experiments (Tests P19–P21) in the 0.35 m burner, showing the flux downwards as a function of radial distance from the burner center (left) and the radial flux as a function of vertical location above the plane defined by the burner surface for locations (R_o) away from the burner axis (right-hand figures; see values of R_o in the tables in Appendix 1). The lines connect the data points. The expanded measurement uncertainty was 16 %.

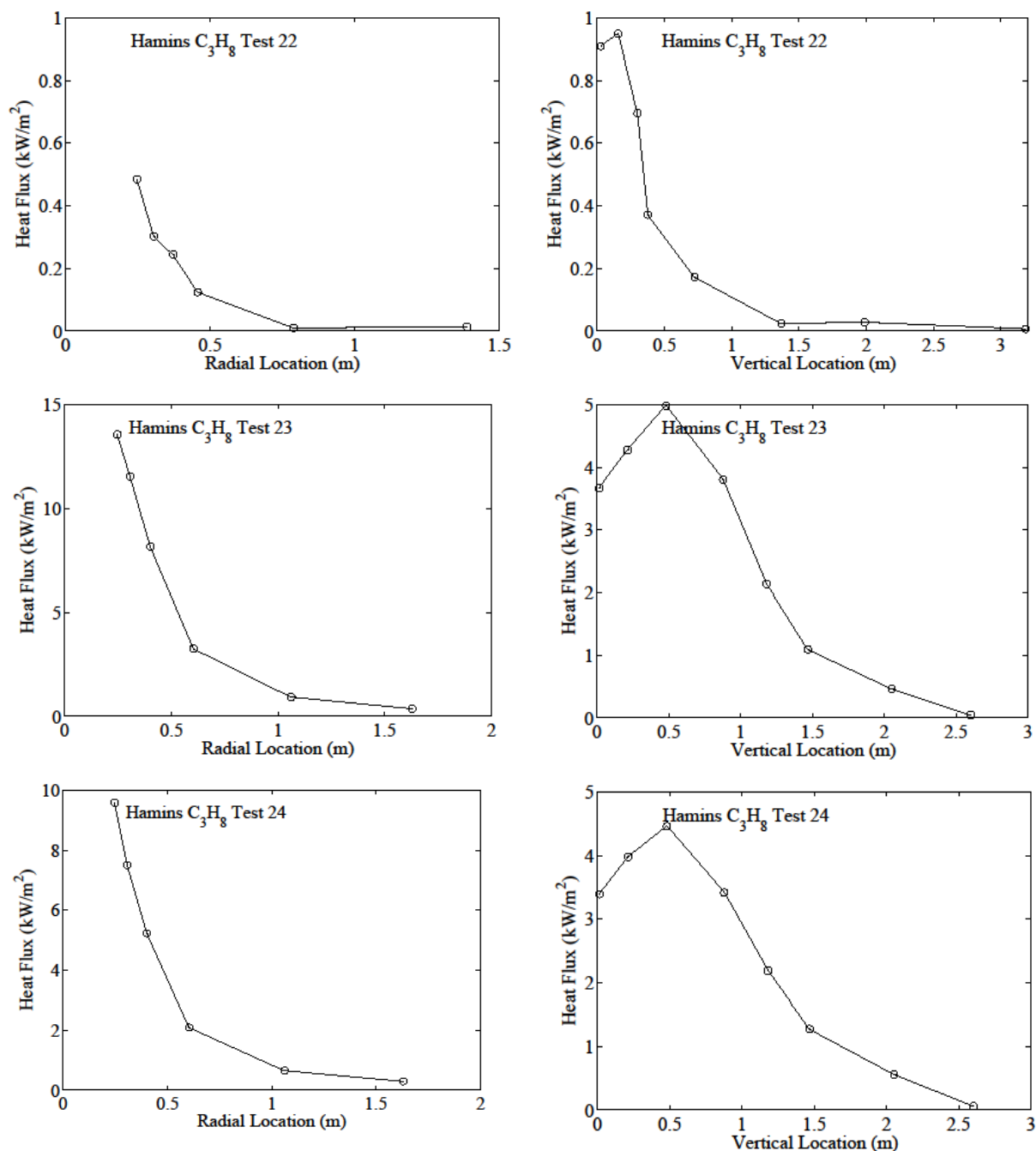


Figure A3.25 The measured local radiative heat flux distributions for 3 propane fire experiments (Tests P22–P24) in the 0.35 m burner, showing the flux downwards as a function of radial distance from the burner center (left) and the radial flux as a function of vertical location above the plane defined by the burner surface for locations (R_o) away from the burner axis (right-hand figures; see values of R_o in the tables in Appendix 1). The lines connect the data points. The expanded measurement uncertainty was 16 %.

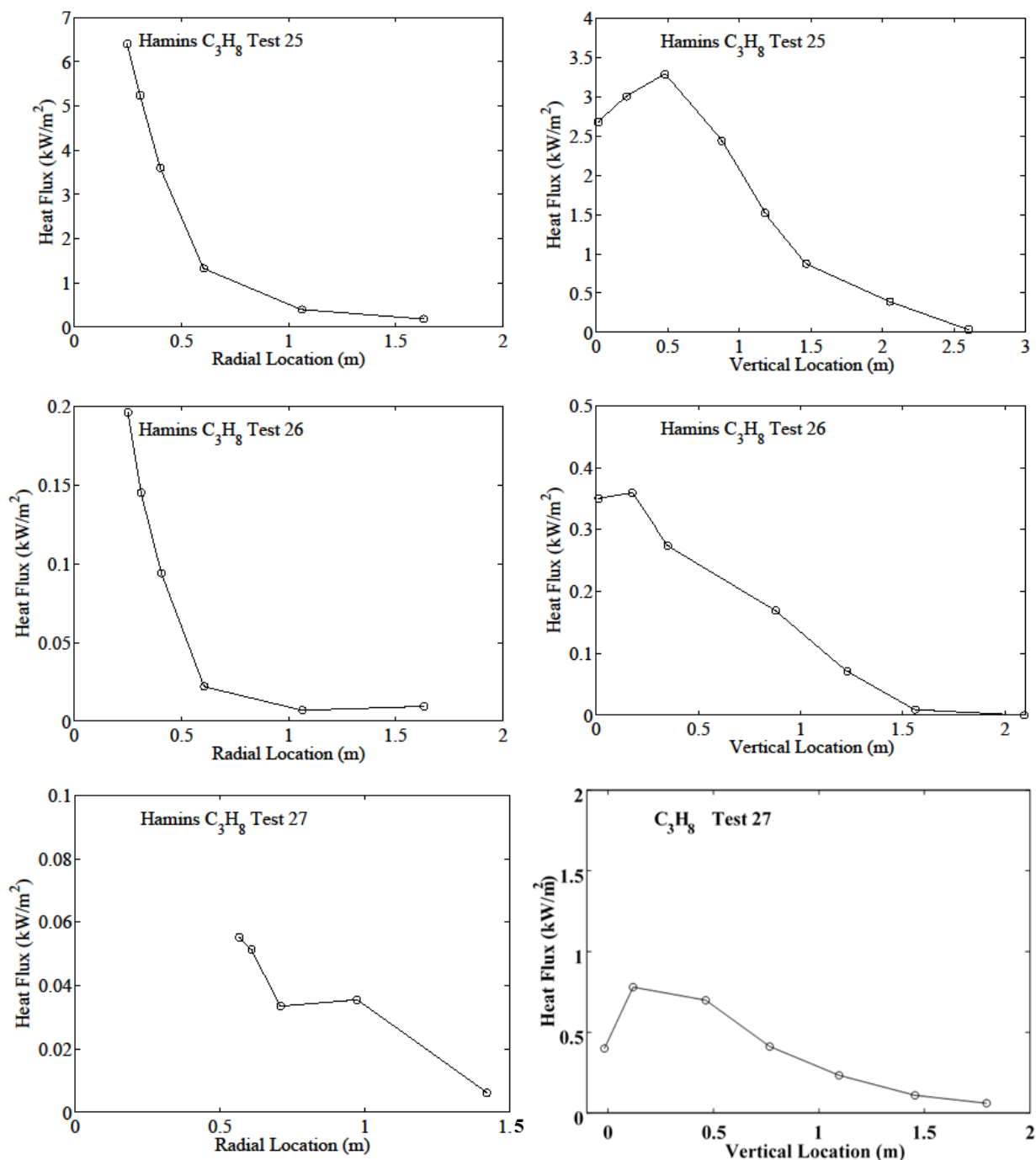


Figure A3.26 The measured local radiative heat flux distributions for 3 propane fire experiments (Tests P25–P27) in the 0.35 m and 1.00 m burners, showing the flux downwards as a function of radial distance from the burner center (left) and the radial flux as a function of vertical location above the plane defined by the burner surface for locations (R_0) away from the burner axis (right-hand figures; see values of R_0 in the tables in Appendix 1). The lines connect the data points. The expanded measurement uncertainty was 16 %.

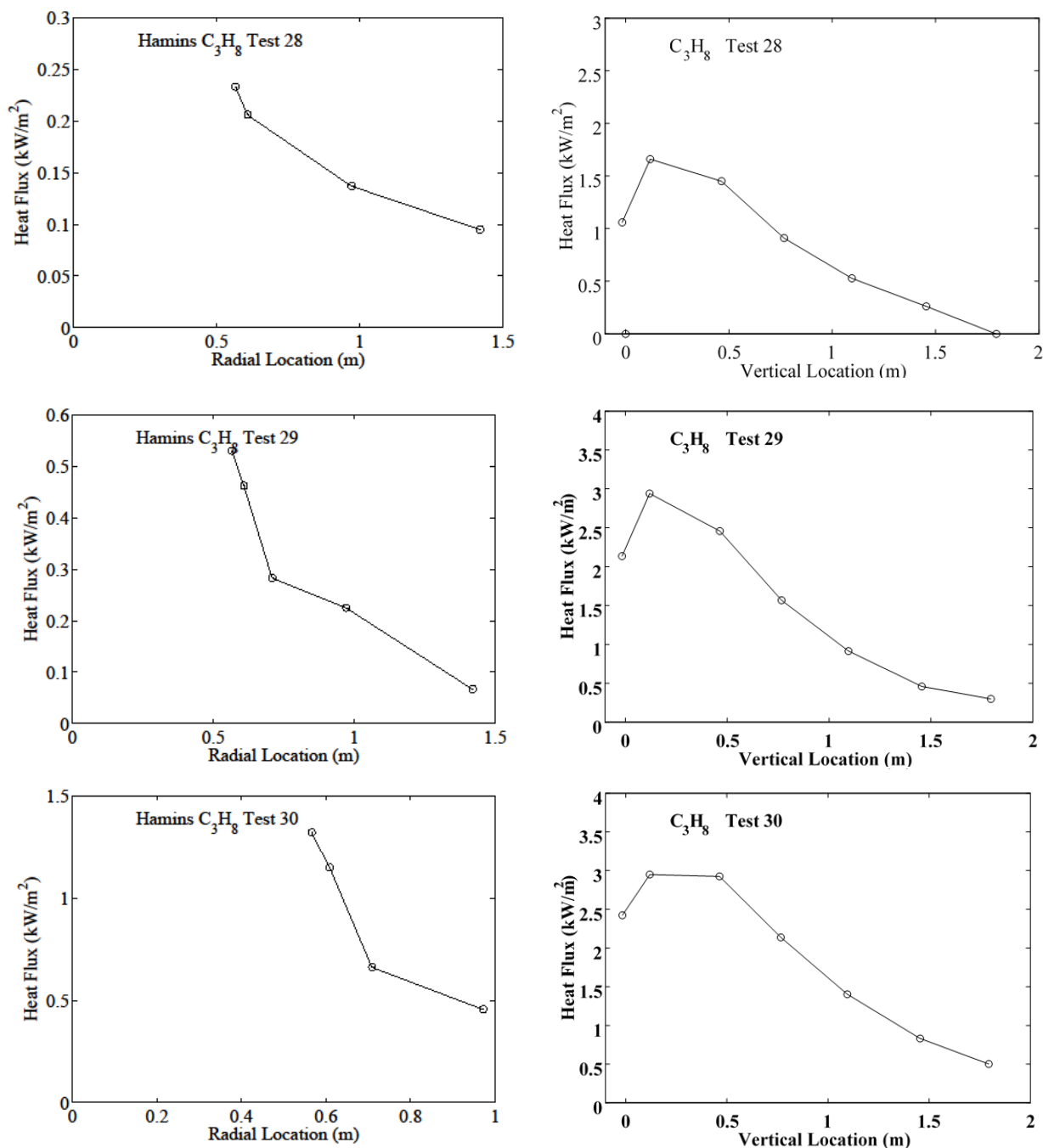


Figure A3.27 The measured local radiative heat flux distributions for 3 propane fire experiments (Tests P28–P30) in the 1.00 m burner, showing the flux downwards as a function of radial distance from the burner center (left) and the radial flux as a function of vertical location above the plane defined by the burner surface for locations (R_o) away from the burner axis (right-hand figures; see values of R_o in the tables in Appendix 1). The lines connect the data points. The expanded measurement uncertainty was 16 %.

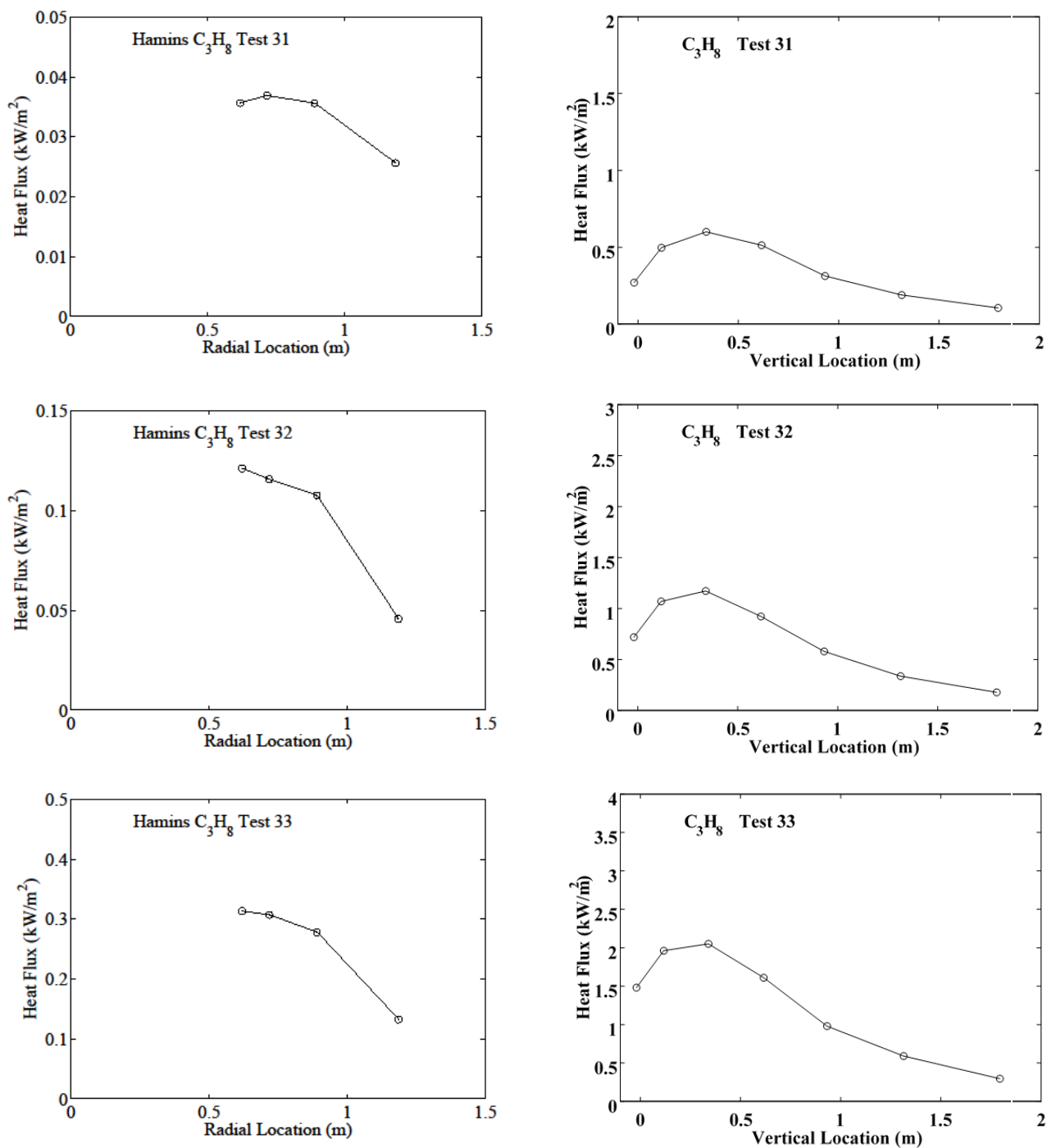


Figure A3.28 The measured local radiative heat flux distributions for 3 propane fire experiments (Tests P31–P33) in the 1.00 m burner, showing the flux downwards as a function of radial distance from the burner center (left) and the radial flux as a function of vertical location above the plane defined by the burner surface for locations (R_o) away from the burner axis (right-hand figures; see values of R_o in the tables in Appendix 1). The lines connect the data points. The expanded measurement uncertainty was 16 %.

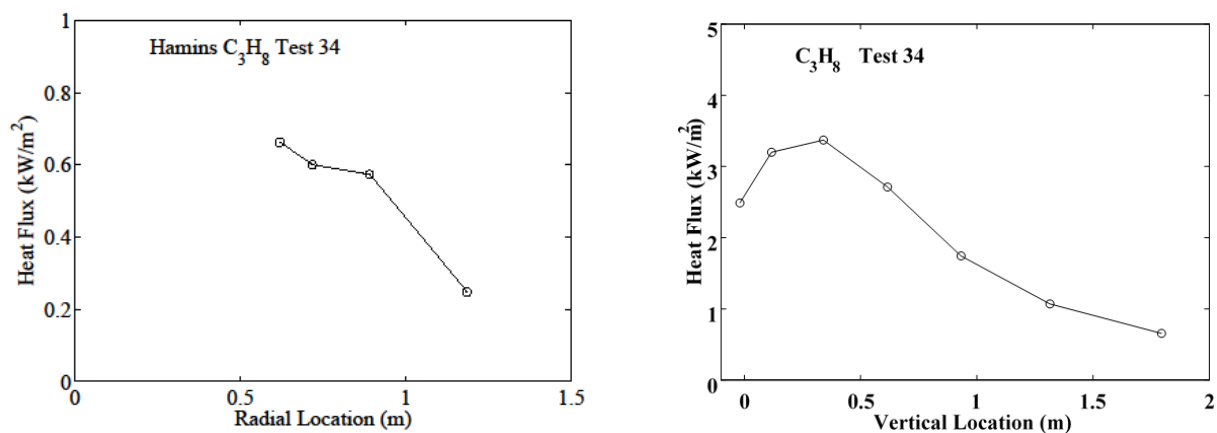


Figure A3.29 The measured local radiative heat flux distributions for a propane fire experiment (Test P34) in the 1.00 m burner, showing the flux downwards as a function of radial distance from the burner center (left) and the radial flux as a function of vertical location above the plane defined by the burner surface for locations (R_0) away from the burner axis (right-hand figures; see values of R_0 in the tables in Appendix 1). The lines connect the data points. The expanded measurement uncertainty was 16 %.